Search for WIMP - ^{129}Xe inelastic scattering in the XMASS large low background liquid Xe detector

Hiroyoshi Uchida
Division of Particle and Astrophysical Science,
Nagoya University

April 10, 2014

Abstract

A search for inelastic scattering of Weakly Interacting Massive Particles (WIMPs) on the isotope ^{129}Xe was done in data taken with the single phase liquid xenon (LXe) detector XMASS at the Kamioka Observatory. The de-excitation of this M1 state in ^{129}Xe proceeds through gamma ray emission or an internal conversion electron with subsequent X-ray emission. As a result of this process, 39.58 keV gamma ray by de-excitation is occurred. Although the signal rate of the inelastic scattering was expected ten times lower than that of the elastic scattering, strong background reduction can be made because of a high energy peak of 39.58 keV. We achieved a lower background $\sim 3 \times 10^{-4}\,\mathrm{keV}^{-1}\,\mathrm{day}^{-1}\,\mathrm{kg}^{-1}$ using reductions, while a signal efficiency of the signal MC of 50 GeV WIMP was 29 %. Using a restricted volume containing 41 kg of LXe at the very center of the detector we observed no significant excess in 165.9 days of data and derived for e.g. a 50 GeV WIMP an upper limit for its inelastic cross section on ^{129}Xe nuclei of 3.2 pb at the 90 % confidence level.

Acknowledgements

I would like to express my deep gratitude to my supervisor, Professor Yoshitaka Itow for introducing me to the XMASS experiment. I would thank him for useful advice to me in my graduate course. I would like to express my deep gratitude to Prof. Y. Suzuki, the spokesperson of the XMASS experiment. He gave me valuable advice related to the experiment and about physics. I would like to express my deep gratitude to Prof. S. Moriyama. He gave many detailed advices. I learned about this analysis and how to face the experiment from him. I would like to thank to XMASS collaboration who worked with me, K. Abe, K. Hieda, K. Hiraide, K. Ichimura, Prof. Y. Kishimoto, K. Kobayashi, K. Nakagawa, Prof. M. Nakahata, H. Ogawa, N. Oka, H. Sekiya, A. Shinozaki, A. Takeda, K. Ueshima, O. Takachio, D. Umemoto, Prof. M. Yamashita, Y. Koshio, B. S. Yang, Prof. S. Tasaka, J. Liu, Prof. K. Martens, H. Nishiie, S. Hirano, Prof. Y. Takeuchi, K. Miuchi, K. Hosokawa, A. Murata, Y. Onishi, Y. Otsuka, Prof. Y. H. Kim, K. B. Lee, M. K. Lee, J. S. Lee, Prof. Y. Fukuda, Prof. K. Masuda, Y. Nishitani, H. Takiya, K. Kobayashi, N. Y. Kim, Prof. Y. D. Kim, D. Motoki, F. Kusaba, Prof. K. Nishijima, K. Fujii, I. Murayama, and Prof. S. Nakamura. I would like to thank to CR laboratory members. I am deeply appreciative of the same class and same laboratory in Nagoya and Kamioka who supported me all the time, D. Suzuki, F. Hayashi, F. Miyake, K. Kawade, Y. Nagai, K. Choi, H. Nishiie, A. Shinozaki, and K. Iyogi,. Special thanks to Prof. K. Fushimi for their useful advices about the inelastic scattering of WIMP - nucleus. I would like to extend my gratitude to all the people who supported and encouraged me during my graduate school. Finally, I would like to express my heartfelt gratitude to my friends and family.

Contents

Chapter 1

Introduction

1.1 Dark Matter

The existence of dark matter in the universe is widely believed because of a variety of observational evidence. Dark matter can not be observed optically. Only the gravitational interaction provides evidences. Existence of dark matter was first described in Ref. [1]. They observed the Coma Clusters, and considered that there is a gravitational source for making such large cluster of galaxies with too large velocity dispersion. As one of the evidences for dark matter, there is a problem in rotation curves of the spiral galaxies. Figure 1.1 shows the rotation curve of the our galaxy [2]. Rotation velocity (v_c) distribution of galaxies is expected from Kepler's laws equation:

$$v(r)^2 = G\frac{M(r)}{r}, \tag{1.1}$$

where G is the gravitational constant, r is the radial distance from the center of the galaxy, and $M(r)$ is the total mass within the radius r. Luminescent matters mostly exist inside the region about a few $k$pc from the center of the galaxy. If luminescent matters become all of matters, the velocity drops at a large r. However, the observed velocity is almost flat outside of luminescent matters, indicating $M(r) \propto r$. This discrepancy refers to the presence of non-luminescent matters in the galaxy.

If we assume our galaxy is a general spiral galaxy such as NGC6503 [3], a rotation velocity of the Sun is $v_c = 220\,\mathrm{km\,s^{-1}}$, and the rotation velocity increases linearly from the galactic center. It reaches almost flat father than $25\,k$pc as shown is Figure 1.1 [2].

The density ρ_0 and velocity v_0 of the dark matter as a function of r can be explained as follows. Assuming the isothermal halo model, a density distribution of the dark halo is

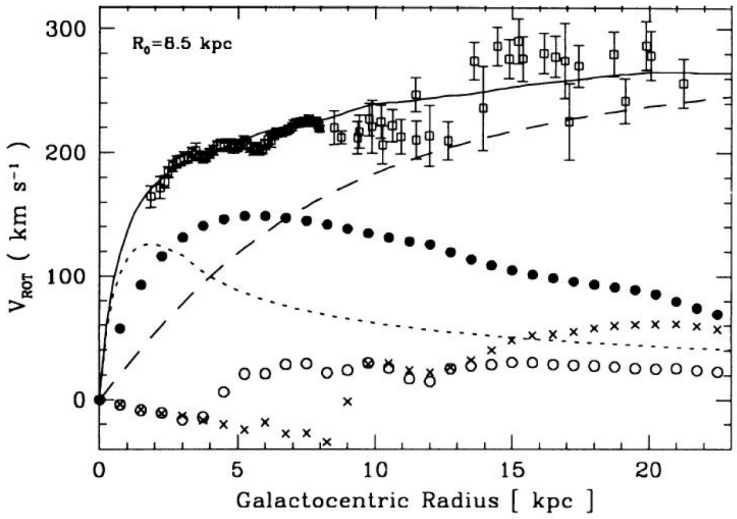

Figure 1.1: Rotation curve of our galaxy [2]. Each lines represent the contribution of the bulge (dotted), the disk (filled circles), the HI layer (crosses), the H_2 layer (circles), and from the dark halo (dashed). The solid line represents the total of the contributions.

$$\rho(r) = \frac{\rho_0}{1 + r^2/r_0^2}\,, \tag{1.2}$$

where ρ_0 and r_0 are fitting parameters. Using the observed rotation velocity, the local halo density of dark matter is evaluated to be

$$\rho(r) \sim 0.3\mathrm{GeVc}^{-2}\mathrm{cm}^{-3} \tag{1.3}$$

with this uncertainty of factor two[4].

1.2 Candidates of Dark Matter

Observation of cosmic microwave background (CMB) and large scale structure of the universe indicate presence of non-baryonic dark matter with the density parameter of $\Omega_{DM}h^2 = 0.12029$, while baryon density $\Omega_b h^2$ is only 0.022068 for the best fit of Plank result [5]. These particles were produced and then decoupled from the thermal equilibrium in the early universe. If dark matter was non-relativistic (relativistic) at that moment, it is classified

as cold (hot) dark matter. One of the candidates for hot dark matter is a neutrino. However, by the results of WMAP and galaxy cluster observation, Ω_ν is found to be at most 0.024 [6]. This is because cold dark matter can reproduce the small scale structure of the universe, while hot dark matter washed out the small scale structure. Many candidates for the cold dark matter have been proposed. Here are the candidates for the cold dark matter of two most common, Axion and WIMP.

1.2.1 Axion

Axion has been proposed to solve the strong CP problem. Allowed mass range of axions are $10^{-6}\,\mathrm{eV} \leq m_a \leq 10^{-3}\,\mathrm{eV}$ and $2\,\mathrm{eV} \leq m_a \leq 5\,\mathrm{eV}$ from laboratory-based experiments and astrophysical observations. Axion could be a candidate of cold dark matter, if mass range is μeV order. On the other hand, a heavy axion is often regarded as a solar axion, because they are likely to be produced in the Sun. A light axion of μeV order has been searched using the Sikivie radio frequency cavity technology. Search for 2.3 - 3.4 μeV mass range was made, but significant signal was not observed [7]. Then the solar axion has been searched in superconducting magnet telescope using the inverse Primakov effect [8] such as CAST [9] and the Tokyo helioscope group [10].

1.2.2 WIMPs of neutralino

Weakly Interactive Massive Particles (WIMPs) are one of the most primitive dark matter candidates. Neutralinos are predicted by the supersymmetric theory (SUSY) is an extension theory beyond the Standard Model of particle physics. They are supposed to be a natural candidate of WIMPs. The minimal supersymmetric extension of the standard model (MSSM) is a theory to explain some of the problem in the standard model. In MSSM all the standard particles with spin j have their supersymmetric partners with spin $|j-1/2|$. All other quantum numbers are the same. Table 1.1 shows particles proposed in supersymmetric theory.

In MSSM, quantum number called R-parity is introduced. This R-parity is assigned to all the standard particles and the supersymmetric particles. R-parity is defined

$$R = (-1)^{3B+L+2S}. \tag{1.4}$$

B is the baryon number, L is the lepton number, and S is the spin. R-parity of supersymmetric particles have an odd number (-1), and its standard particles have even (+1). According to the R-parity conservation, heavy

Table 1.1: The supersymmetric particles and the particles in the Standard Model [12]

SM particle	Name	Spin	Feel these forces	Mediates these forces	Superpartner	Spin
e, μ, τ	Charged leptons (electron,muon, tau)	1/2	EM,W	-	sleptons $\tilde{e}, \tilde{\mu}, \tilde{\tau}$ (selectron, smuon,stau)	0
ν_e, ν_μ, ν_τ	neutrinos	1/2	W	-	sneutrinos $\tilde{\nu_e}, \tilde{\nu_\mu}, \tilde{\nu_\tau}$	0
u, c, t	up, charm, top quarks	1/2	EM,W,S	-	squarks $\tilde{u}, \tilde{c}, \tilde{t}$	0
d, s, b	down, strange, bottom quarks	1/2	EM,W,S	-	squarks $\tilde{d}, \tilde{s}, \tilde{b}$	0
γ	photon	1	-	EM	photino $\tilde{\gamma}$	1/2
$W^{\pm}$	weak boson	1	EM,W	W	Wino $\tilde{W^{\pm}}$	1/2
Z	weak boson	1	W	W	Zino $\tilde{Z}$	1/2
g	gluon	1	S	S	gluino $\tilde{g}$	1/2
G	graviton	2	-	GR	gravitino $\tilde{G}$	3/2
h	Higgs boson	0	W	generates mass	higgsino $\tilde{h}$	1/2

supersymmetric particles decay into lighter supersymmetric particles, which must be stable (LSP) as the lightest. If supersymmetric particles decay to standard particles, its R-parity conservation is broken. Neutralino is a linear combination of photino ($\tilde{\gamma}$), zino ($\tilde{Z}$), and higgsinos ($\tilde{H^0_{u1}}, \tilde{H^0_{d2}}$). The photino ($\tilde{\gamma}$) and zino ($\tilde{Z}$) are shown by

$$\tilde{\gamma} = cos\theta_W \tilde{B} + sin\theta_W \tilde{W_3} \tag{1.5}$$

$$\tilde{Z} = -sin\theta_W \tilde{B} + cos\theta_W \tilde{W_3}. \tag{1.6}$$

$\tilde{B}$、$\tilde{W_3}$ are supersymmetric particles of gauge bosons. So the neutralino($\widetilde{\chi^0_n}$)

is shown by the following function;

$$\widetilde{\chi_n^0} = N_1\tilde{B} + N_2\tilde{W}_3 + N_3\tilde{H}_{u1}^0 + N_4\tilde{H}_{d2}^0, \tag{1.7}$$

magnitude of N_1, N_2, N_3, N_4 decide on nature of neutralinos.
Then mass matrix of the neutralino can be expressed as follows:

$$M = \begin{pmatrix} M_1 & 0 & -m_z cos\beta sin\theta_w & m_z sin\beta sin\theta_w \\ 0 & M_2 & m_z cos\beta cos\theta_w & -m_z sin\beta cos\theta_w \\ -m_z cos\beta sin\theta_w & m_z cos\beta cos\theta_w & 0 & -\mu \\ m_z sin\beta sin\theta_w & -m_z sin\beta cos\theta_w & -\mu & 0 \end{pmatrix} \tag{1.8}$$

M_1, M_2 are the masses of the gaugino, m_z is a mass of the Z boson, μ is a mass parameter of the higgsino, θ_w is the mixing angle of weak interactions (Weinberg angle), $\tan\beta = v_2/v_1$, v_1 and v_2 are the vacuum expectation values of the Higgs. The LSP in the neutralino is a candidate for dark matter. These particles interact with ordinary particles only via gravity and any forces weaker than the electromagnetic force.

1.3 WIMP search

WIMPs can be detected by inelastic scattering and elastic scattering with nuclei. Spin-independent (SI) and spin-dependent (SD) interactions are considered. Each interaction is explained in this section. WIMPs can be detected also by annihilation or decay products in cosmic rays. They are called as indirect searches. Here various dark matter search experiments in the world are described.

1.4 Direct search experiments

If a nucleus of target is recoiled by WIMP, energy is deposited in the detector. The direct search method is to measure various signals produced by recoil of target nucleus. Therefore, a detector of dark matter requires low background for obtaining a very weak signal, high mass targets , and low energy threshold. Here explains direct search experiments of WIMP as follows.

1.4.1 DAMA/LIBLA

DAMA/LIBRA group searched dark matter using 233 kg NaI scintillator. The NaI (Tl) scintillator was high purity without radioactive background,

and had large scintillation yields. They achieved 2 keV_{ee} energy threshold and conducted observations of a cycle of 13 years. Total exposure was 1.17 ton·year. They reported the annual modulation signal with 8.9 σ which would be independent of the galactic halo models. Modulation amplitude in the energy range of 2-6 keVee was of $0.0116 \pm 0.0013\,\mathrm{CPD}^{-1}\mathrm{kg}^{-1}\mathrm{keV}$ particular. Measured phase and period were 146 ± 7 days and 0.999 ± 0.002 year, respectively. However, other experiments such as CDMS and XENON of which sensitivity is higher than the DAMA/LIBRA experiment could not confirm the DAMA/LIBRA result.

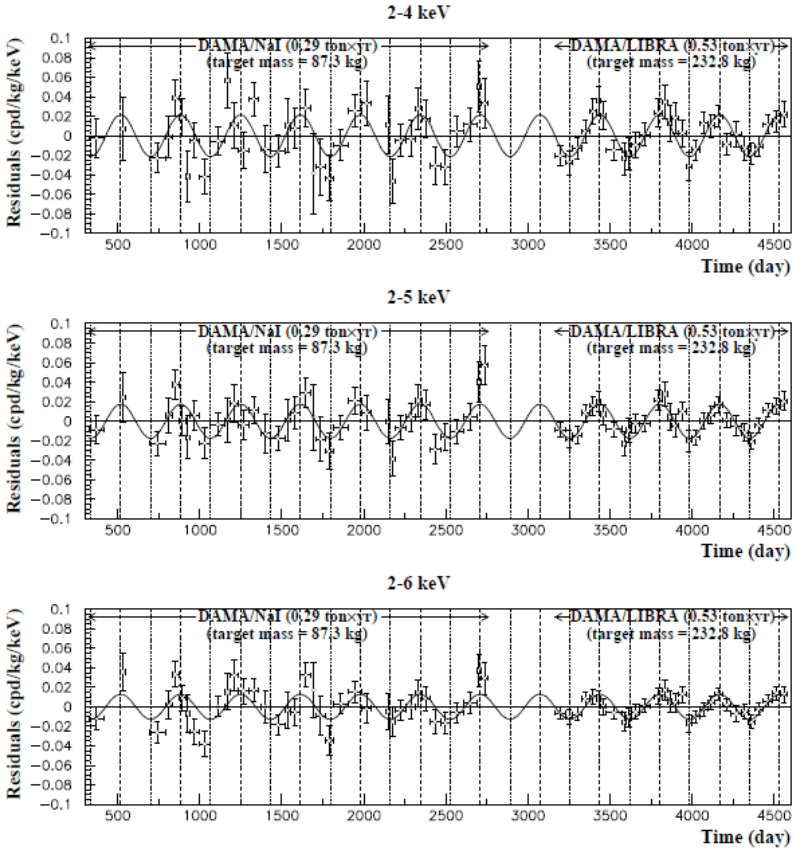

Figure 1.2: Residual rates measured by DAMA/LIBRA experiment [13].

1.4.2 CDMS

In the Cryogenic Dark Matter Search (CDMS II) experiment, a superconducting detector, an array of 30 detectors of 19 Ge and 11 Si, was operated

below 50 mK. The thickness of the disk was 10 mm and the diameter was 76 mm. This detector obtained deposit energy from two information of ionization and phonon due to nuclear recoils. The ratio of the ionization due to recoil energy was used to separate nuclear recoil signals from electron signals. And the timing information due to phonon pulses was used for better reduction of surface background. They observed two events in the signal region with estimated background of 0.9 events. They considered these events was leakage surface electrons. The CDMS collaboration reported a 90 % C.L. upper limit for SI cross section of $3.8 \times 10^{-44}\,\mathrm{cm}^2$ for a WIMP mass of $70\,\mathrm{GeV\,c^{-2}}$ [14].

1.4.3 XENON

XENON10 and XENON100

The XENON10 and XENON100 experiments used a double phase LXe time projection chamber (TPC) with liquid and gas phases of Xe. The main idea is background rejection using a ratio of two types of scintillation lights. The primary signal of energy deposition in the liquid phase is called S1. The other signal of drift electrons in the gas phase is called S2 of proportional light. They reported the result of 58.6 live days using a fiducial mass of 5.4 kg. he result of 90 % C.L. upper limit for nucleon spin-independent cross-section was reported as $8.8 \times 10^{-44}\,\mathrm{cm}^2$ for a WIMP mass of $100\,\mathrm{GeV\,c^{-2}}$ [15]. In the XENON100 phase, they reported the result of 224.6 live days using a fiducial mass of 34 kg. The result of 90 % C.L. upper limit for nucleon spin-independent cross-section was obtained as $2 \times 10^{-45}\,\mathrm{cm}^2$ for a WIMP mass of $55\,\mathrm{GeV\,c^{-2}}$ [16].

1.4.4 LUX

The large underground Xenon (LUX) experiment has started filling of Xe and cooling was carried out from February 2013. This experiment uses a double phase LXe detector similar to XENON100 detector and installed in the Sanford Underground Research Facility. With the analyses of the experimental data for the fiducial volume of 118 kg in 85.3 days from April to August 2013, they reported the results of dark matter search. By the profile-likelihood analysis technique, the 90 % confidence limits was set on the spin-independent WIMP-nucleon elastic scattering cross section of $7.6 \times 10^{-46}\,\mathrm{cm}^2$ for a WIMP mass of $33\,\mathrm{GeV\,c^2}$ [18]. This is the best limit of spin-independent WIMP-nucleon elastic scattering so far.

1.4.5 XMASS

The XMASS (Xenon detector for weakly interacting MASSive particle) is an single phase LXe detector for observing low energy events using a LXe scintillator. The detector is located at Kamioka Observatory of Institute for Cosmic Ray Research (ICRR) university of Tokyo. The observatory locates 1000 m underground (2700 m water equivalent) in the Kamioka mine at Mt. Ikenoyama. XMASS has a plan for three phase of experiments; the 100 kg prototype detector, the 1 ton class detector, and the 20 ton class detector. The 100 kg prototype LXe detector was used for detector technology development of XMASS experiment. Then construction of 800 kg detector (XMASS-I) started on the basis of this R&D in 2007. Data taking of commissioning phase of 800 kg detector for the dark matter search started at October 2010 and finished at May 2012. After this runs, the refurbishment work started in 2012 to reduce radioactive backgrounds inside the detector. Data taking was restarted after the refurbishment of XMASS detector on Dec. 2013. Several experimental results have been published for low mass WIMP search and solar axion search, etc.

1.5 Indirect search experiment

When WIMPs is a Majorana particle, gamma rays or other particles are generated by their annihilation. Annihilations likely occur at the galactic center, the galactic halo, or the center of astronomical object such as the Sun, where WIMPs gravitationally concentrate. These signals can be observed by gamma rays or neutrinos or other cosmic ray particles. This is called as indirect searches.

1.5.1 Super-Kamiokande

Super-Kamiokande is a 10 kt water Cherenkov detector in Kamioka Observatory. They show the results of the indirect search of high-energy neutrinos from WIMP annihilations in the Sun by using upward-going muon (upmu) events from SK I-SK III data of 3109.6 days. They searched for an excess of the neutrinos from the Sun as compared to the background events due to atmospheric neutrinos in three upmu categories: stopping, non-showering, and showering. However they were no significant excess observed. The 90 % C.L. upper limits of upmu flux induced by WIMPs of 100 GeV c^{-2} were 6.4 $\times$ 10^{-15} cm^{-2} s^{-1} and 4.0 $\times$ 10^{-15} cm^{-2} s^{-1} for the soft and the hard annihilation channels, respectively. These limits correspond to upper limits of 4.5

$\times$ $10^{-39}\,\mathrm{cm}^2$ and 2.7 $\times$ $10^{-40}\,\mathrm{cm}^2$ for SD interaction cross section, respectively [19].

1.5.2 IceCube

The IceCube detector of neutrino telescope is located at the South Pole in Antarctica. The IceCube uses a large volume of ice at the South Pole for observing neutrinos. Digital optical modules (DOM) in the ice detect Cherenkov lights from particles produced by high energy neutrino interactions as the signal of them. The IceCube collaboration shows the result of muon neutrinos from WIMP annihilation in the center of the Sun. They analyzed 317 days data from June 2010 to May 2011. As the result, they obtained the upper limits on SD and SI cross sections in the range of 20 - 5000 $\mathrm{GeV\,c^{-2}}$ WIMP mass. These results are the strongest limit on SD WIMP-proton cross section above 35 $\mathrm{GeV\,c^{-2}}$ for most of WIMP models [20].
Figures 1.3, 1.4, and 1.5 show summary of experimental results for spin independent cross section, spin dependent cross section of neutron coupling, and spin dependent cross section of proton coupling, respectively.

1.6 WIMP search by inelastic scattering

Internationally significant experimental efforts have been made to probe for such nuclear recoils through elastic scattering [48, 13, 49, 50, 16, 51, 52, 14, 53]. An inelastic scattering that excites a nucleus to suitable low lying nuclear excited states provides another avenue to probe for WIMP dark matter. Its advantage is that nuclear excited states and their de-excitation mechanisms are typically well measured, and thus the expected energy deposited in the detector is known, resulting in the readily identifiable signature of a line in the energy spectrum. Using ^{127}I there are experimental searches for this inelastic scattering with the excitation level of 57.6 keV [54, 55].
In xenon the isotope ^{129}Xe has a low lying excited state at 39.58 keV; lower than that for ^{127}I, yet significantly above both the XMASS data acquisition and analysis thresholds. Figure 1.6 shows a level of ^{129}Xe. The de-excitation of this M1 state in ^{129}Xe proceeds through gamma ray emission or an internal conversion electron with subsequent X-ray emission. With its high nuclear charge Xe itself is a good absorber for such gamma rays, providing LXe detectors with an intrinsically high detection efficiency for the prospective signal, which is safely above the detector threshold.
The DAMA group had performed a search of elastic scattering of spin dependent using a LXe of large mass [23]. On the other hand, they started

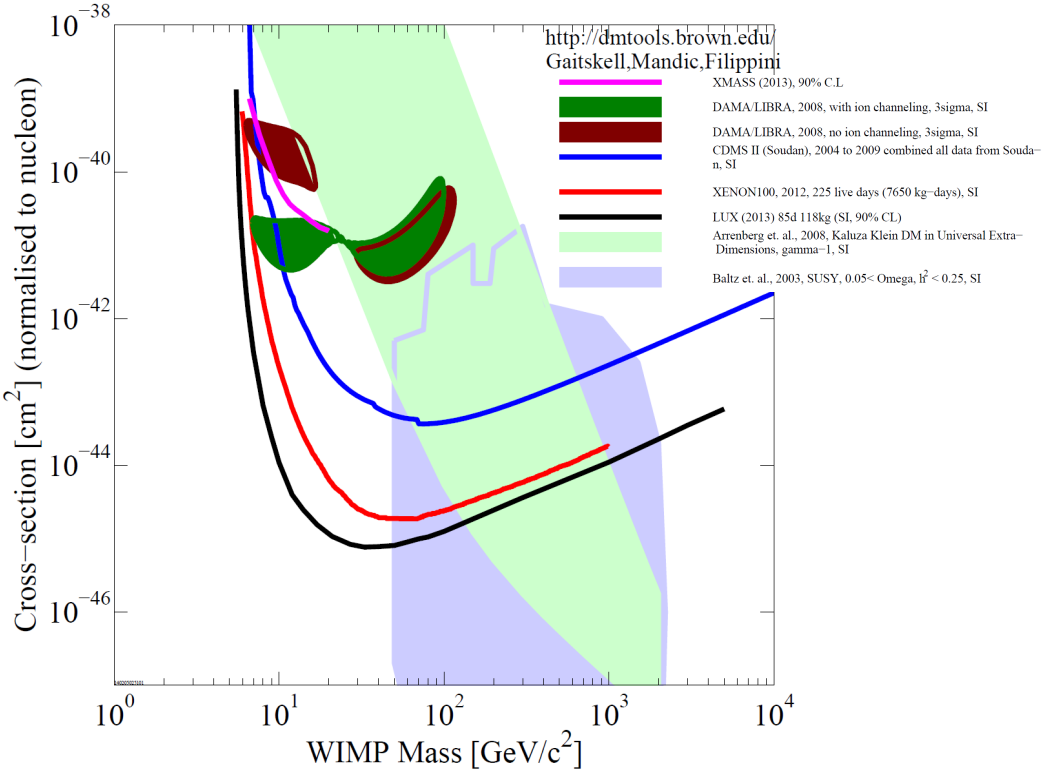

Figure 1.3: Upper limit of the spin independent cross section. Allowed region at 3σ from DAMA and upper limits from CDMSII, XENON100, LUX, and XMASS (low mass WIMP analysis with 835 kg LXe) experiments. This figure is taken from Ref. [21].

the inelastic scattering search with the 99.5 % enriched ^{129}Xe [56]. So far the DAMA group searched for this signal in a 2500 kg·day exposure of 6.5 kg of LXe. They used 99.5 % enriched ^{129}Xe and constrained the inelastic cross section for 50 GeV WIMPs to be less than 3 pb at 90 % C.L. [57].
A motivation of analysis of the inelastic scattering search in the XMASS is to find the dark matter signal. A peak of 39.58 keV from WIMP - ^{129}Xe is an enough high energy for the XMASS which has the high light-yield detector. Therefore the analysis of the inelastic scattering search has a possible to become a good sensitivity comparison of the DAMA group because the background reduction is possible effectively with this energy region. In this thesis, analysis of WIMP - ^{129}Xe inelastic scattering is explained. In Chapter 2, a method of the WIMP detection is described with calculations of a signal spectrum. In Chapter 3, an overview of XMASS experiment is explained. In

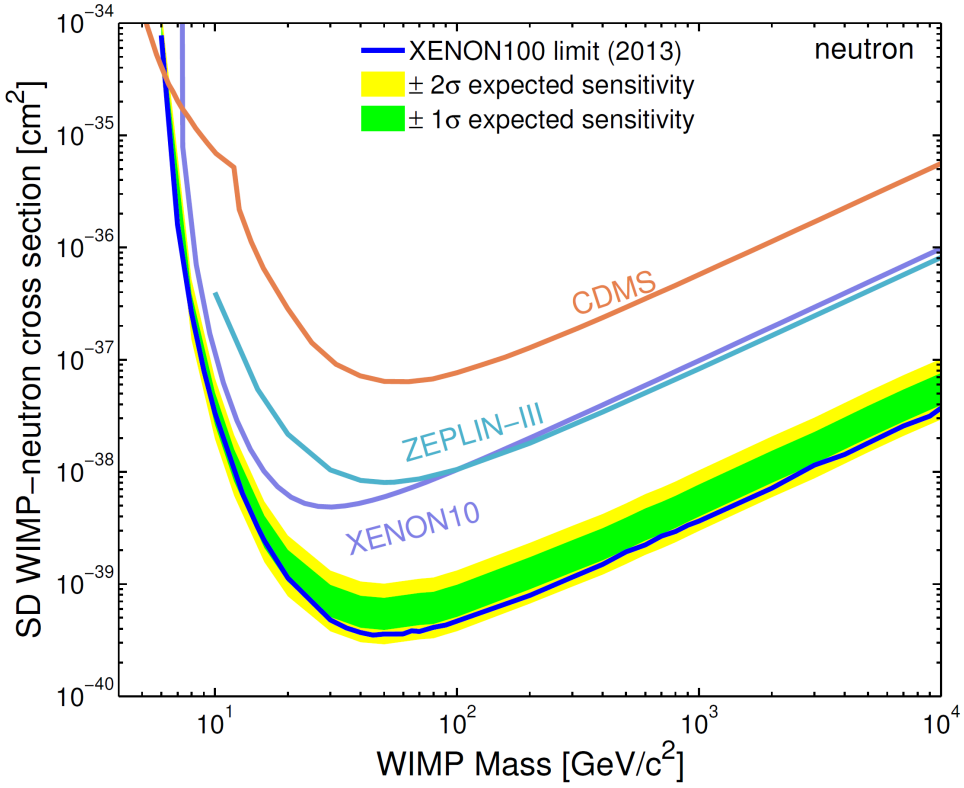

Figure 1.4: Upper limit of the spin dependent cross section for neutron coupling. Upper limits from CDMS, ZEPLIN − III, XENON10, and XENON100 experiments. This figure is taken from Ref. [17].

Chapter 4, an overview of a background for dark matter search is explained. In Chapter 5, an summary of detector calibration is explained. In Chapter 6 and 7, an analysis of WIMP - ^{129}Xe inelastic scattering is explained. This Chapter is a main part of this thesis. Finally, a conclusion of this thesis is shown.

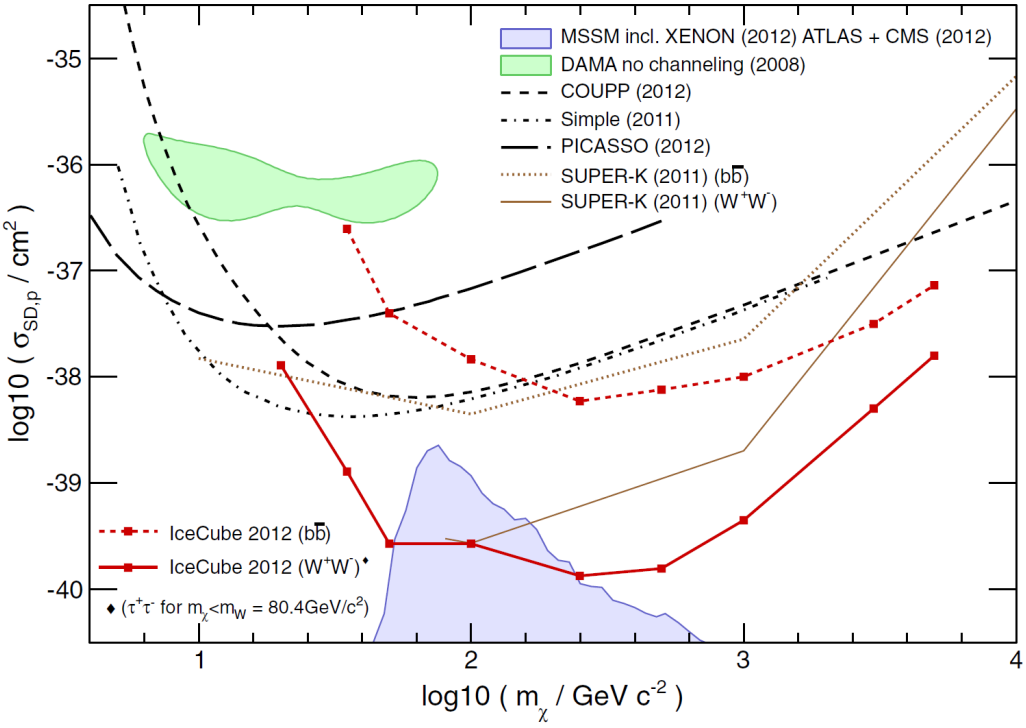

Figure 1.5: Upper limit of the spin dependent cross section for proton coupling. Allowed region at 3σ from DAMA and upper limits from COUPP, Simple, and PICASSO. Also shown the results from indirect searches by Super-Kamiokande, and IceCube experiments for solar WIMP annihilations to neutrinos. This figure is taken from Ref. [20].

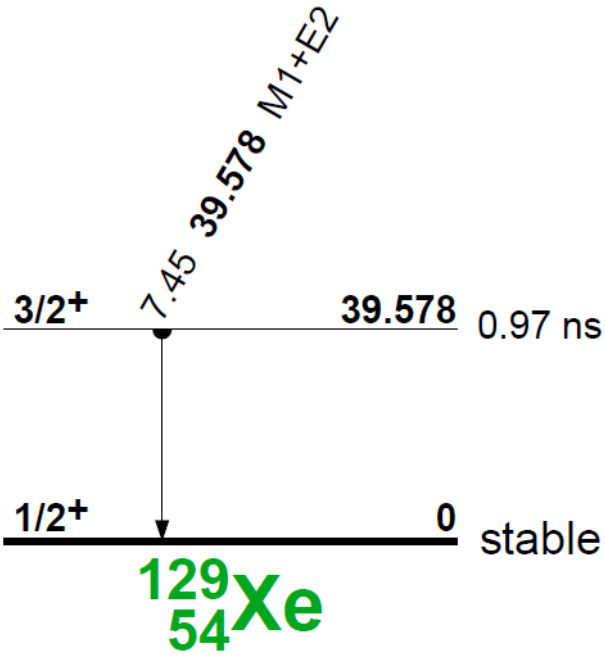

Figure 1.6: The level of ^{129}Xe [22]. ^{129}Xe has a low lying excited state at 39.58 keV with 0.97 ns as a decay constant.

Chapter 2

Direct detection of WIMPs

In this chapter the theory of direct detection is described based on Ref. [12, 24, 29]. It is considered that direct detection of dark matter can be realized by observing the interaction with the target nucleus. It is necessary to know an event rate of dark matter in order of detection. The event rate depends on density and velocity of dark matter.

2.1 WIMP - nucleus scattering

The density of dark matter particle is given by

$$dn = \frac{n_0}{k}\ f(v, v_e)\ d^3v, \tag{2.1}$$

$$n_0 \equiv \int_0^{v_{esc}} dn = \rho_D / M_\chi\,, \tag{2.2}$$

$$\text{and } k = \int_0^{2\pi}\ d\phi\ \int_{-1}^{1}\ d(cos\theta) \int_0^{v_{esc}}\ f(v, v_e)\ v^2\ dv. \tag{2.3}$$

k is a normalization constant. n_0 is the mean number density of the dark matter particle. $\rho_D = 0.3\,\mathrm{GeV\,c^{-2}\,cm^{-3}}$ is dark matter density. M_χ is the neutralino mass. The Maxwell-Boltzmann distribution is

$$f(v, v_e) = e^{-(v+v_e)^2/v_0^2}. \tag{2.4}$$

v is the dark matter velocity on the target. v_e is the earth velocity relative to the dark matter distribution. $v_{esc} = |v + v_e|$ is the local galactic escape velocity. As $v_{esc} = \infty$, k is shown following from Eq. 2.3

$$k = k_0 = (\pi\ v_0^2)^{3/2}, \tag{2.5}$$

The differential event rate is shown as

$$dR = \frac{N_A}{A}\sigma_{\chi-N}\ v\ dn\,. \tag{2.6}$$

N_A is the Avogadro number per unit mass ($6.02 \times 10^{26}\,\mathrm{kg}^{-1}$). A is the mass number of target nucleus. $\sigma_{\chi-N}$ is neutralino-nucleus cross section for zero momentum transfer.

R_0 of total event rate for the $v_e = 0$ and the $v_{esc} = \infty$ is shown as

$$R_0 = \frac{N_A}{A}\sigma_{\chi-N}\frac{\rho_D}{M_\chi}\frac{2}{\sqrt{\pi}}\ v_0. \tag{2.7}$$

R_0 is shown as following in a unit of $\mathrm{kg}^{-1}\,\mathrm{day}^{-1}$ and $v_0 = 230\,\mathrm{km\,s}^{-1}$

$$R_0 = \frac{361}{M_\chi\ M_N}\left(\frac{\sigma_{\chi-N}}{1\ pb}\right)\left(\frac{\rho_D}{0.3\ GeV\ c^{-2}\ cm^{-3}}\right)\left(\frac{v_0}{230\ km\ s^{-1}}\right). \tag{2.8}$$

M_N is the mass of the target nucleus. The unit of M_χ and M_N is $\mathrm{GeV\,c}^{-2}$.

R of total event rate for the $v_e \neq 0$ and $v_{esc} \neq \infty$ is shown as

$$R = R_0\frac{\sqrt{\pi}}{2}\frac{\langle v\rangle}{v_0} = R_0\frac{k_0}{k}\frac{1}{2\pi v_0^4}\int v\ f(v, v_e)\ d^3v. \tag{2.9}$$

And the total event rate R(v_e,v_{esc}) is shown as

$$\frac{R(v_e, v_{esc})}{R_0} = \frac{k_0}{k_1}\Big[\frac{R(v_e,\infty)}{R_0}\ -\ \Big(\frac{v_{esc}^2}{v_0^2}\ +\ \frac{1}{3}\frac{v_e^2}{v_0^2}\ +\ 1\Big)e^{-v_{esc}^2/v_0^2}\Big], \tag{2.10}$$

$$\frac{R(v_e,\infty)}{R_0} = \frac{1}{2}\Big[\sqrt{\pi}\Big(\frac{v_e}{v_0} + \frac{1}{2}\frac{v_0}{v_e}\Big)erf\Big(\frac{v_e}{v_0}\Big)\ +\ e^{-v_e^2/v_0^2}\Big], \tag{2.11}$$

$$\text{and}\ \frac{R(0, v_{esc})}{R_0} = \frac{k_0}{k_1}\Big[1 - \Big(1 + \frac{v_{esc}^2}{v_0^2}\Big)e^{-v_{esc}^2/v_0^2}\Big]. \tag{2.12}$$

The error function: erf and k_1 are shown as

$$erf\Big(\frac{v_e}{v_0}\Big) = 2/\sqrt{\pi}\int_0^{\frac{v_e}{v_0}}\ exp(-t^2)\ dt\,, \tag{2.13}$$

$$\text{and}\ k_1 = k_0\Big[erf\Big(\frac{v_{esc}}{v_0}\Big)\ -\ \frac{2}{\sqrt{\pi}}\frac{v_{esc}}{v_0}e^{-v_{esc}^2/v_0^2}\Big]. \tag{2.14}$$

The differential rate depending on the recoil energy (E_R) is shown as

$$\frac{dR}{dE_R} = \int_{E_{min}}^{E_{max}} \frac{1}{Er}\, dR(E) \;=\; \frac{1}{E_0 r} \int_{v_{min}}^{v_{max}} \frac{v_0^2}{v^2}\, dR(v). \tag{2.15}$$

$E_{min} = E_R/r$ is the minimum energy. E_0 is $1/2M_\chi v_0^2$.

Using Eq. 2.9, the differential event rate is shown as

$$\frac{dR}{dE_R} = \frac{R_0}{E_0 r}\frac{k_0}{k}\frac{1}{2\pi v_0^2} \int_{v_{min}}^{v_{max}} \frac{1}{v}\, f(v, v_e)\, d^3v. \tag{2.16}$$

Expected spectrum was calculated by this function.

2.2 Cross section of elastic scattering

In order to calculate an expected spectrum, cross section have to be assumed. The elastic scattering cross section is shown as

$$\sigma_{\chi-N} = 4G_F^2 \mu_{\chi-N}^2 C_N\,, \tag{2.17}$$

$$\mu_{\chi-N} = \frac{M_\chi M_N}{M_\chi + M_N}\,, \tag{2.18}$$

$$\text{and } C_N = C_N^{SI} + C_N^{SD}. \tag{2.19}$$

$\mu_{\chi-N}$ is the reduced mass. G_F is the Fermi coupling constant ($1.166 \times 10^{-5}\, GeV^{-2}(\hbar c)^3$), C_N is enhancement factor, and C_N is sum of SI and SD. $\sigma_{\chi-N}$ can be replaced by $\sigma_{\chi-p}$ (neutralino-proton cross section) and $\sigma_{\chi-n}$ (neutralino-neutron cross sections) with C_N, C_p (enhancement factor of proton), and C_n (enhancement factor of neutron) as following function:

$$\sigma_{\chi-N} = \sigma_{\chi-n}\frac{\mu_{\chi-N}^2}{\mu_{\chi-n}^2}\frac{C_N}{C_n},\,. \tag{2.20}$$

C_n and $\sigma_{\chi-n}$ terms are changed to C_p and $\sigma_{\chi-p}$ for proton.
The enhancement factor of the SI cross section is shown as

$$C_N^{SI} = \frac{1}{\pi G_F^2}\Big[Zf^{(p)} + (A-Z)f^{(n)}\Big]^2. \tag{2.21}$$

Z is the atomic number, $f^{(p)}$ and $f^{(n)}$ are neutralino-proton (neutron) couplings. If $f^{(p)} \simeq f^{(n)}$, $C_N^{SI} \propto A^2$. Therefore

$$\frac{C_N^{SI}}{C_p^{SI}} \simeq \frac{C_N^{SI}}{C_n^{SI}} \simeq A^2\,, \tag{2.22}$$

$$\text{and } \sigma_{\chi-N}^{SI} = \sigma_{\chi-p}^{SI}\frac{\mu_{\chi-N}^2}{\mu_{\chi-p}^2}\, A^2\,, \tag{2.23}$$

using Eq. 2.20 and Eq. 2.22. A target nucleus of large A has the advantage for SI interaction.
The enhancement factor of the SD cross section is shown as

$$C_N^{SD} = \frac{8}{\pi}\Big(a_p\langle S_p\rangle + a_n\langle S_n\rangle\Big)^2 \frac{J+1}{J}\,, \tag{2.24}$$

$$\text{and } a_p = \sum_{q=u,d,s} \frac{\alpha_{2q}}{\sqrt{2}G_F}\Delta_q^{(p)}\,. \tag{2.25}$$

The part of $(a_p\langle S_p\rangle + a_n\langle S_n\rangle)$ is called Lambda factor: Λ. a_p are the neutralino-proton (neutron) SD couplings. J is the total spin of the nucleus. $\Delta_q^{(p)}$ and $\Delta_q^{(n)}$ are the quark spin contents of nucleon (proton or neutron).

$$C_N^{SD} = \frac{8}{\pi}\Lambda^2 J(J+1). \tag{2.26}$$

Using Eq. 2.20 and Eq. 2.26

$$\sigma_{\chi-N}^{SD} = \sigma_{\chi-p}^{SD}\frac{\mu_{\chi-N}^2}{\mu_{\chi-p}^2}\frac{\Lambda^2 J(J+1)}{0.75}\,. \tag{2.27}$$

$\Lambda^2 J(J+1)$ of proton is 0.75 from Table 2.1.

2.3 Form factor

The cross section of WIMP-nucleus has a effect of this nucleus form. A calculation of the cross section needs to include the this effect as form factor.

The cross section is shown using the cross section of zero momentum transfer σ_0,

$$\sigma(qr_n) = \sigma_0\ F^2(qr_n)\,. \tag{2.28}$$

q is the momentum transfer ($\sqrt{2M_N E_R}$) and r_n is the effective nuclear radius.

The form factor of SI is shown as

$$F^2(qr_n) = \Big[\frac{3j_1(qr_n)}{qr_n}\Big]^2 e^{-q^2s^2}, \tag{2.29}$$

$j_1(x) = [sin(x) - xcos(x)]/x^2$ is a spherical Bessel function. $r_1 = (R^2 - 5s^2)$, $R \simeq 1.2fm \times A^{1/3}$ and $s \simeq 1fm$ in Ref. [24].

A Form factor of SD interaction is calculated from the nuclear spin structure function. The isoscalar (a_0) and isovector (a_1) are shown as

$$a_0 = a_p + a_n\,, \tag{2.30}$$

$$\text{and } a_1 = a_p - a_n. \tag{2.31}$$

unpaired proton			
Isotope	J	Abundance (%)	$\Lambda^2 J(J+1)$
^{1}H	1/2	100	0.750
^{7}Li	3/2	92.5	0.244
^{19}F	1/2	100	0.647
^{23}Na	3/2	100	0.041
^{127}I	5/2	100	0.007
^{133}Cs	7/2	100	0.052

unpaired neutron			
Isotope	J	Abundance (%)	$\Lambda^2 J(J+1)$
^{3}He	1/2	1.3×10^{-4}	0.928
^{29}Si	1/2	4.7	0.063
^{73}Ge	9/2	7.8	0.065
^{129}Xe	1/2	26.4	0.124
^{131}Xe	3/2	21.2	0.055
^{183}W	1/2	14.3	0.003

Table 2.1: Values of $\Lambda^2 J(J+1)$ calculated on the basis of the odd group model for various nuclei [29].

The form factor is shown as using the spin structure function $S(q)$

$$F^2(q) = \frac{S(q)}{S(0)}\,, \tag{2.32}$$

$$\text{and } S(q) = a_0^2 S_{00}(q) + a_1^2 S_{11}(q) + a_0 a_1 S_{01}(q). \tag{2.33}$$

The form factor of SD has a effect for the cross section when the nucleus has a unpair nucleon. The spin structure function $S(q)$ [30] was used in Figure 2.2, the ratio a_n/a_p is -0.853. The Figure 2.1 and 2.2 show the nuclear form factor as a function of recoil energy for spin independent case and spin dependent case.

2.4 Expected spectrum by WIMP-Xe elastic scattering

The expected signal spectrum of dark matter is described. The event rate of dark matter depends on the target nucleus and WIMP mass. The Figures 2.3 and 2.4 show the event rate of dark matter by the SI interactions with Xe and

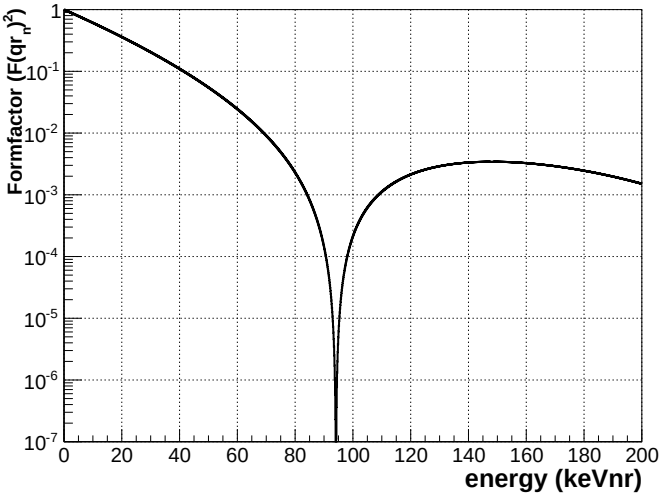

Figure 2.1: The form factor of Xe as a function of recoil energy for spin independent case.

those by SD interactions with ^{129}Xe and ^{131}Xe. The neutralino masses were assumed as $M_x = 50\,GeV$ and $M_x = 100\,GeV$. SI and SD cross sections were assumed as $\sigma^{SI}_{\chi-p} = 1\,\mathrm{pb}$ and $\sigma^{SD}_{\chi-n} = 1\,\mathrm{pb}$. Also, the recoil energy spectrum depends on target nuclei, which would be useful to determine the mass of WIMPs.

2.5 Scintillation efficiency

A visible energy of the nuclear recoil and the electron recoil have a different. This is an effect by a different of sum of a deposit energy per unit length (dE/dx), detector response, and etc. The effect is called to scintillation efficiency. Many detector are calibrated by gamma ray source (electron recoil). Therefore exchanging factor of the visible energy is needed from the nuclear recoil to the electron recoil. The ratio of the visible energy to the nuclear recoil energy is shown as

$$E_R = \frac{E_v}{L_{eff}(E_R)}, \tag{2.34}$$

A $L_{eff}(E_R)$ is the relative scintillation efficiency. The $L_{eff}(E_R)$ have been measured using neutron source. The $L_{eff}(E_R)$ value measurement in XMASS have not still done because of the difficult of the single scattering neutron

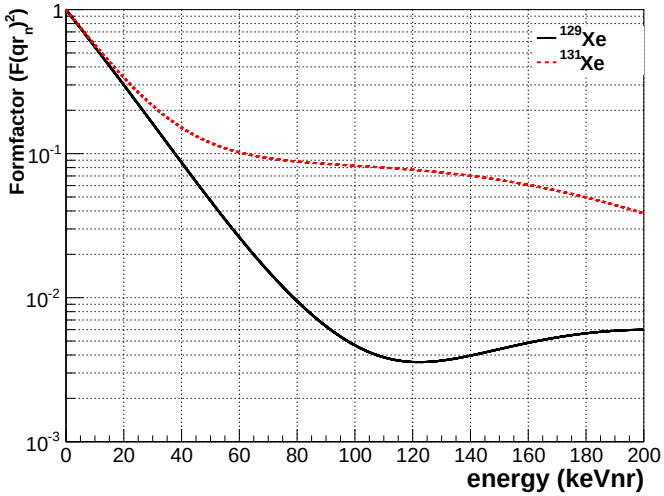

Figure 2.2: The form factor of ^{129}Xe and ^{131}Xe as a function of recoil energy for spin dependent case [30]. The ^{129}Xe and ^{131}Xe are shown by the black solid and the red solid line, respectively.

measurement for multi scattering of neutron. This measurement will be planed in future. In an analysis of this thesis, $L_{eff}(E_R)$ by XENON100 detector was used for using the same target nucleus. In Chapter 6.5.6, a curve of $L_{eff}(E_R)$ is shown.

2.6 Expected spectrum for ^{129}Xe inelastic scattering

WIMP on ^{129}Xe inelastic scattering produces a 39.58 keV γ-ray from de-excitation and a few keV energy deposition due to nuclear recoil. Energy spectra for the nuclear recoil part are obtained as described in Ref. [56, 57]. The differential rate for inelastic scattering of WIMPs is calculated from

$$\frac{dR}{dE_{det}} = \frac{dE_R}{d(\mathcal{L}_{\rm eff}E_R)}\frac{dR}{dE_R} = \frac{dE_R}{d(\mathcal{L}_{\rm eff}E_R)}\frac{\rho_\chi N_T \sigma_I^{as} M_N c^2}{2M_\chi \mu^2}F^2(E_R)\int_{v_{min}(E_R)}^{v_{max}}\frac{1}{v}\frac{dn}{dv}dv, \tag{2.35}$$

where R is event rate in a unit mass of the target, E_{det} is the detected energy in electron equivalent, E_R is the recoil energy, $\mathcal{L}_{\rm eff} = \mathcal{L}_{\rm eff}(E_R)$ is a factor that converts nuclear recoil energy E_R to electron equivalent energy E_{det} relative to that of 122 keV gamma at zero electric field [63, 64], ρ_χ is

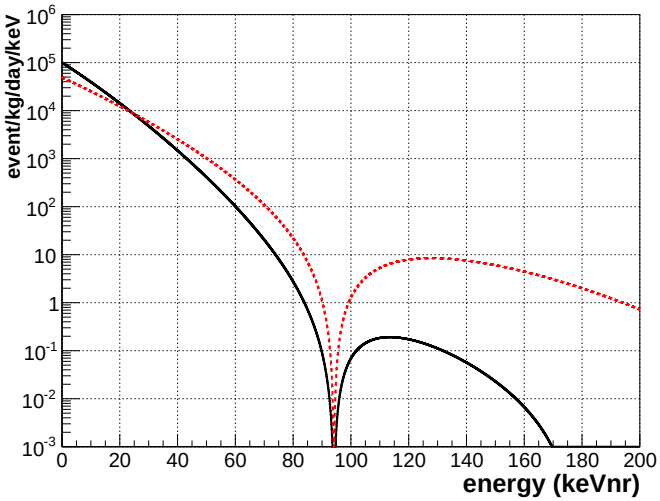

Figure 2.3: The expected event rate of Xe for spin independent case. The neutralino masses M_χ are assumed 50 GeV and 100 GeV. The spin independent cross section $\sigma^{SI}_{\chi-p}$ is assumed to be 1 pb. The neutralino masses of 50 GeV and 100 GeV are shown by the black solid and the red dash line, respectively.

the local mass density of dark matter ($0.3\,\mathrm{GeV\,c^{-2}\,cm^{-3}}$) [65], N_T is the number of target nuclei, σ^{as}_I is the asymptotic cross section for inelastic scattering, M_N is the mass of the target nucleus, M_χ is the WIMP mass, μ is the reduced mass of the WIMP mass and the target nucleus mass, $F^2(E_R)$ is the nuclear form factor of ^{129}Xe, v_{max} is the maximum velocity of the WIMPs in the Earth's vicinity (approximated by the local escape velocity for the galaxy, $650\,\mathrm{km\,s^{-1}}$), $v_{min}(E_R)$ is the minimum velocity to cause the excitation of the nuclei, v is the velocity of the WIMP, and dn/dv is the velocity distribution of WIMPs. The velocity distribution, dn/dv, is assumed to be quasi-Maxwellian. The galactic rotation velocity is v_0=220 $\mathrm{km\,s^{-1}}$[24]. The average of the earth velocity is v_e=232 $\mathrm{km\,s^{-1}}$[66]. Following Ref. [56, 57], the minimum velocity needed to excite ^{129}Xe is evaluated as;

$$v_{min} = v^0_{min} + \frac{v^2_{thr}}{4v^0_{min}}, \tag{2.36}$$

with:

$$v_{min}^0 = \sqrt{\frac{M_N E_R}{2\mu^2}}, \tag{2.37}$$

$$E_{det} = E^* + \mathcal{L}_{\text{eff}} E_R, \tag{2.38}$$

$$v_{thr}^2 = 2\Delta E c^2/\mu, \tag{2.39}$$

where ΔE is the energy of the first excited state of ^{129}Xe (39.58 keV) and $E^* \sim \Delta E$ is the sum of all the energy deposited in the de-excitation process.

The total event rate in the case of a point-like target thus becomes;

$$R_{I,\text{point-like}} = \int_{v_{thr}}^{v_{max}} \frac{\rho_\chi v}{M_\chi} N_T \sigma_I(v) \frac{dn}{dv} dv = \frac{\rho_\chi \langle v \rangle}{M_\chi} f N_T \sigma_I^{as}, \tag{2.40}$$

$$f = \frac{1}{\langle v \rangle} \int_{v_{thr}}^{v_{max}} (v^2 - v_{thr}^2)^{1/2} \frac{dn}{dv} dv, \tag{2.41}$$

where $\sigma_I(v)$ is the excitation cross section for a point-like target, which is shown as the following function of the WIMP velocity v;

$$\sigma_I(v) = \frac{\mu^2}{\pi M_N} |\langle N^*|M|N\rangle|^2 \Big(1 - \frac{v_{thr}^2}{v^2}\Big)^{1/2} = \sigma_I^{as} \Big(1 - \frac{v_{thr}^2}{v^2}\Big)^{1/2} \tag{2.42}$$

with $\langle N^*|M|N\rangle$ being the matrix element for inelastic scattering. Details can be found in Ref. [67]. To incorporate effects of the finite size of the ^{129}Xe nucleus, the form factor $F^2(E_{nr})$ should be taken into account such as Figure 2.5. In fact, there are several models on the form factor for ^{129}Xe including recent studies on the effect of uncertainties due to WIMP-nucleon currents [68, 69, 70, 71, 73]. In this thesis, we chose the same model [23, 68] as DAMA group [56, 57] for comparison.

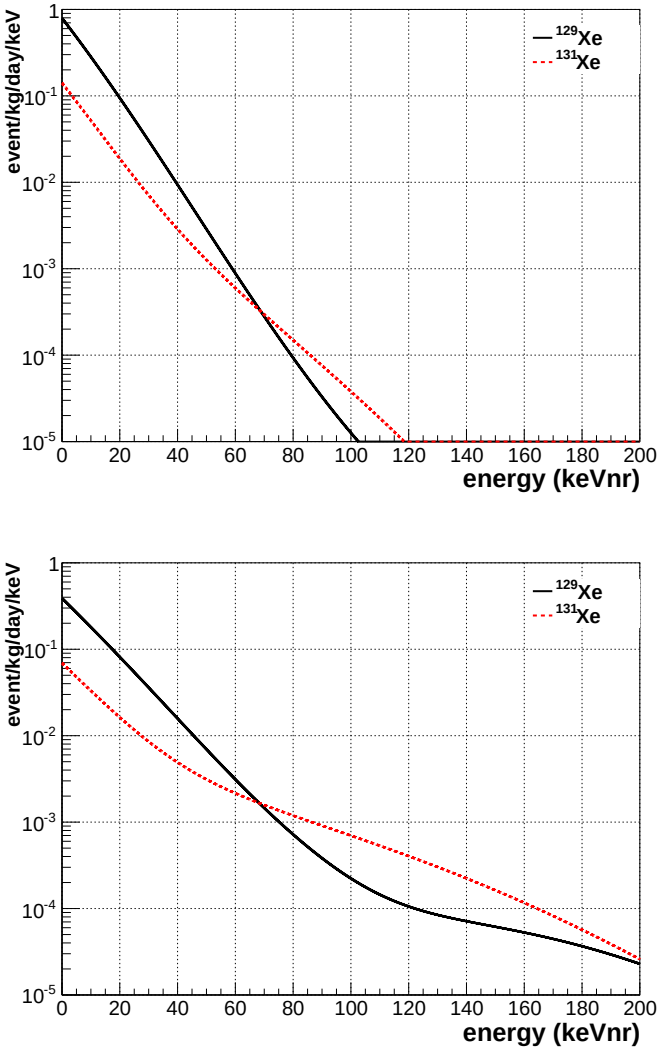

Figure 2.4: The expected event rate of ^{129}Xe and ^{131}Xe for spin dependent case. The neutralino masses M_χ are assumed 50 GeV (the top figure) and 100 GeV (the bottom figure). The spin dependent cross section $\sigma^{SD}_{\chi-n}$ is assumed to be 1 *pb*. The ^{129}Xe and ^{131}Xe are shown by the black solid and the red solid line, respectively

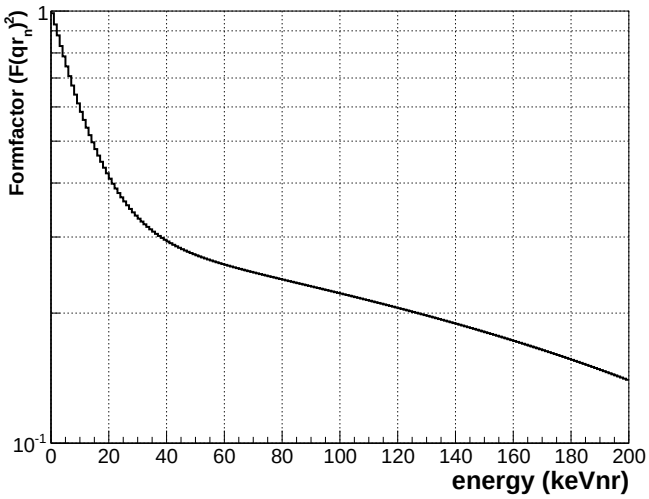

Figure 2.5: The form factor of ^{129}Xe for inelastic scattering. This form factor was used by the DAMA LXe experiment [23].

Chapter 3

XMASS experiment with liquid xenon

3.1 XMASS

Figure 3.1 shows the overall of XMASS. A detail about XMASS is explained as follows.

3.1.1 800 kg detector

The 800 kg detector is the main part of the XMASS experiment. The detector consists of Inner Vacuum Chamber (IVC) and Outer Vacuum Chamber (OVC) made of oxygen-free copper. There are a PMT holder made of oxygen-free high conductivity copper (OFHC), 642 low background PMTs, and liquid Xe inside IVC. The space between IVC and OVC was vacuumed for insulation to prevent heat intrusion from the outside. The PMT holder were assembled into sixty tetrahedral structure combining twelve sites pentagons combined five triangles (pentakis-dodecahedron). Photocathodes of all PMTs were directed toward the center of detector. Filler made of OFHC covered the PMT holder to reduce amount of LXe into the IVC. The side of photocathodes of all PMTs are immersed in liquid Xe of 1ton in IVC. The PMT holder had an inner sensitive volume filled with LXe of 835 kg. Because of a hexagonal shape of photocathode surface of PMT, the gap of PMTs were reduced as much as possible. As a result, the photocathode coverage of the detector was achieved to be 62.4 %. Figure 3.2 shows the arrangement IVC, OVC, and the PMT holder. Figure 3.3 shows an PMT holder with PMTs mounted with and without Filler. PMT installation work is shown in Figure 3.4.

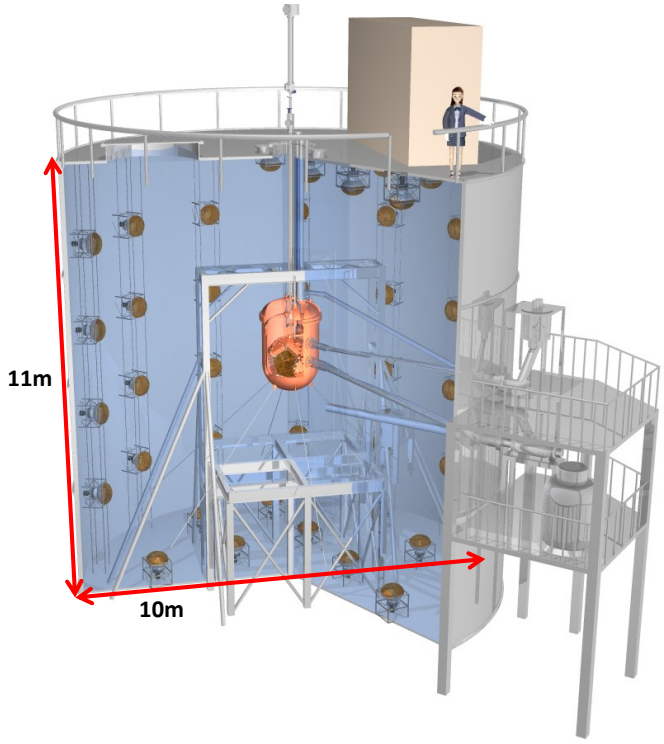

Figure 3.1: XMASS detector
The 800 kg detector is located the center of the water tank. Electronics hut for data acquisition system is installed at top of the water tank.

3.1.2 Water tank

The water tank is a cylinder of 10 m diameter and hight of 11 m. They are made of stainless steel. The tank was designed to shield the 800 kg detector. Inside the tank, 72 20-inch PMTs, which is same type as used in the Super-Kamiokande, were installed on the inner surface of the tank. The ultra-pure water was used as a shield at the 800 kg detector against γ rays, fast neutrons, and to tag cosmic ray muons. Cherenkov lights caused by cosmic ray muons were detected by 20-inch PMTs in the tank. Therefore the tank works as passive shield and an active veto for external backgrounds.

3.1.3 Low background PMT

The main background source in XMASS experiment is PMT. It is necessary to reduce the radioactive isotopes in PMT materials for the success of low background experiment. We developed low background PMTs consisting

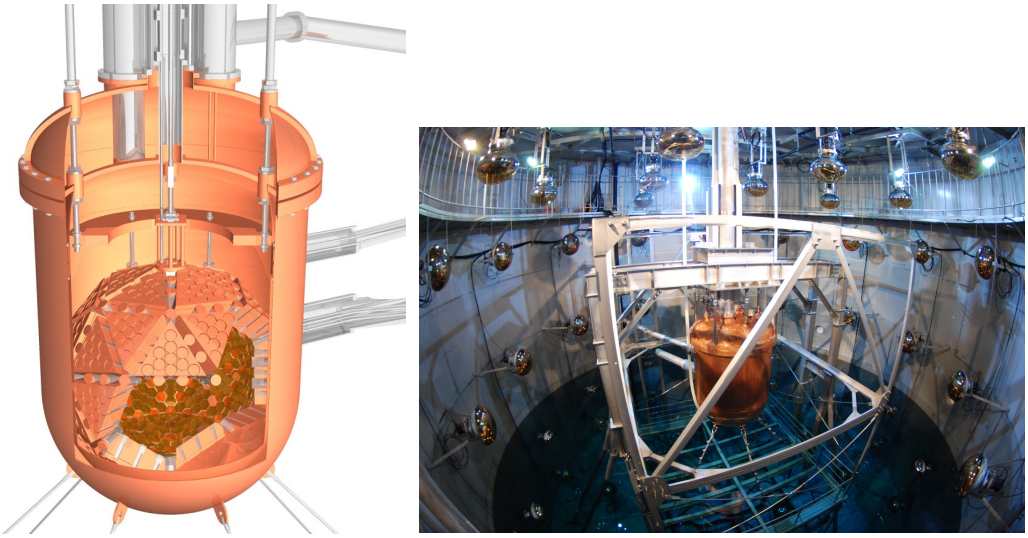

Figure 3.2: 800 kg detector

of selected parts with low radioactivity in collaboration with Hamamatsu Photonics. In order to immerse the PMT in the LXe, it was required to operate at a liquid Xe temperature. Quantum efficiency of the PMT was approximately 30 % at the LXe temperature. Table 3.1 shows the radioactive

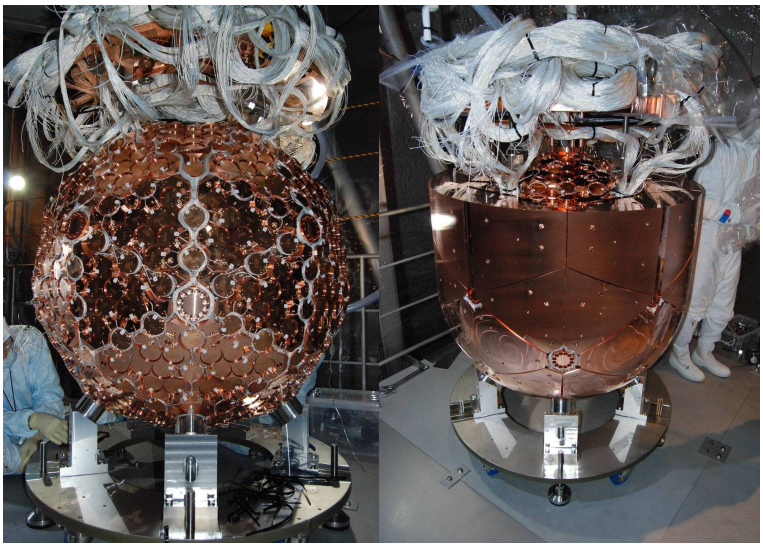

Figure 3.3: PMT holder after PMT installation (left) and after Filler installation (right)

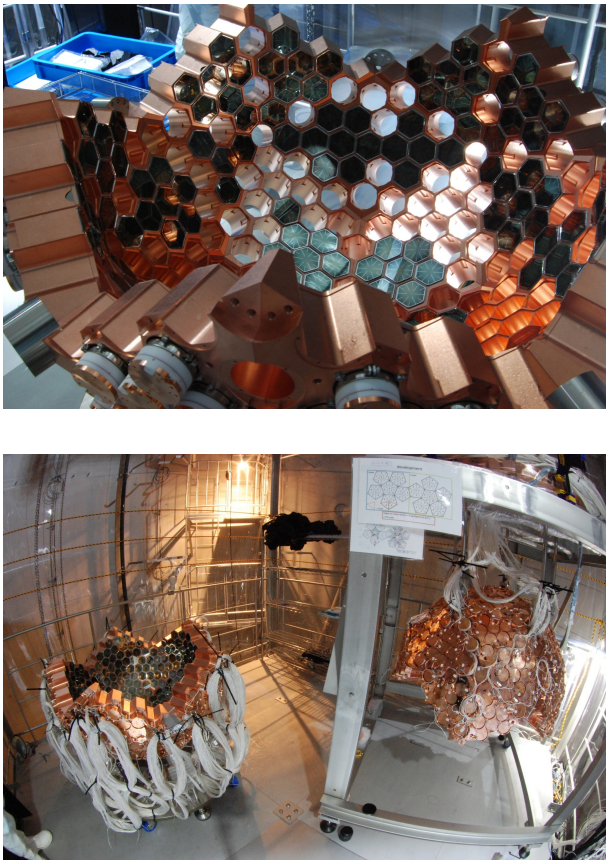

Figure 3.4: PMT holder during the PMT installation work

impurities contained in the PMT. Figure 3.5 shows the PMT photo and the circuit of the bleeder.

3.2 Xe

LXe is target material for WIMP scattering in the XMASS experiment. LXe have many advantages for dark matter search as follows.

- High scintillation light yield ($\sim$42 [photons keV^{-1}])

A kinetic energy of the WIMP is very small from several keV to several tens of keV. So energy deposit by nuclear recoil of Xe is small. Therefore, a low energy threshold can be obtained by this large scintillation light, which is very advantageous to the WIMP search.

Table 3.1: The contamination of radioactive sources in PMT[29]

Radioactive material	U	Th	K	^{60}Co
Measurement value(mBq/PMT)	0.704 ± 0.282	1.51 ± 0.31	5.10	2.92 ± 1.61

- Relatively longer wavelength of scintillation light (∼175 nm)

Peak wavelength of Xe scintillation light "175 nm" is a long wavelength compared to other noble gas scintillators (i.e.Ar∼128 nm). It can be directly detected by the PMT without a wavelength length shifter.

- Relatively high temperature in liquid phase

LXe can be kept at a relatively high temperature as compared to the noble gas (- 95 ℃ at 0.1 MPa at - 108 ℃ at 0 MPa).

- High density

Since density is about 2.9 g cm^{-3}, 800 kg of LXe can be stored in a sphere with a diameter of 80 cm. LXe can be used as a compact laboratory equipment. Figure 3.6 shows as the LXe temperature and density [32].

- Large atomic number

Because the atomic number of Xe is large: Z = 54, so the radiation length is short: 2.77 cm, high energy γ rays atenuates rapidly upon entering the LXe. The self-shielding ability of LXe is a main idea of the XMASS experiment. If large volume of LXe can be provided, external γ rays stopped in the surface of the liquid Xe, then the center can be realized as environment of low background for WIMP search. Figure 3.7 shows the attenuation coefficient of γ rays in LXe.

- Easy phase change

Figure 3.8 shows the phase diagram of Xe. The Xe can be handled in phase of both liquid and gas. Therefore, we can attempt many existing techniques to reduce radioactive impurities contained in the Xe.

- Many isotope

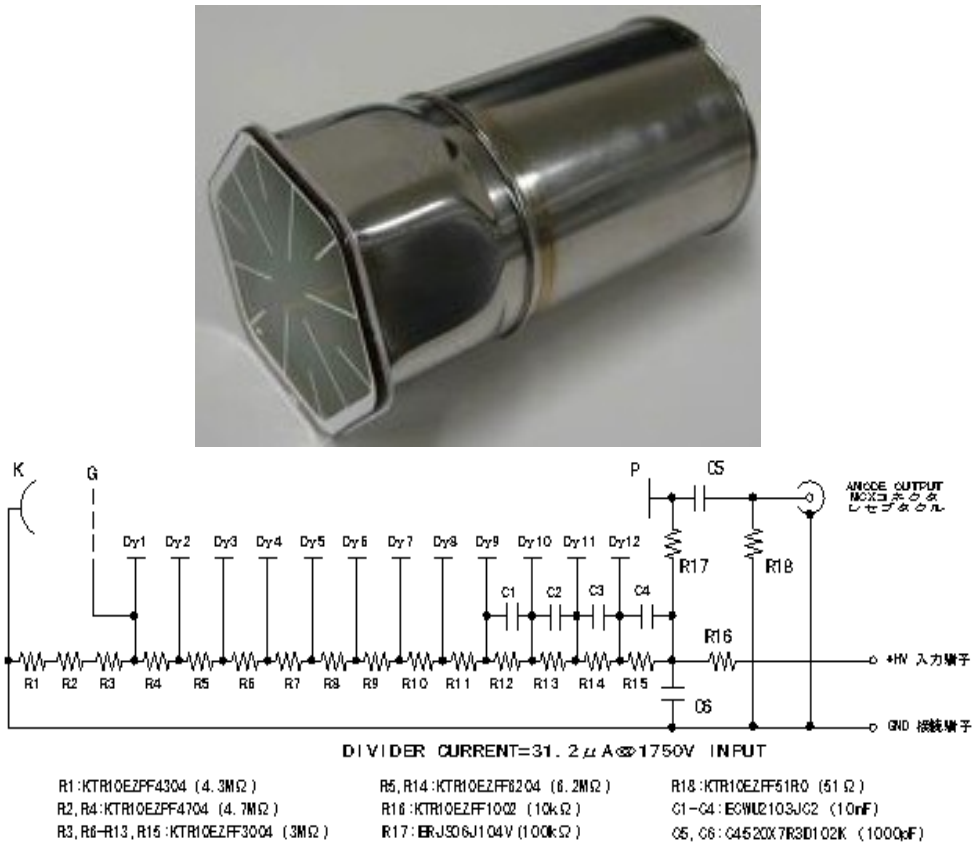

Figure 3.5: Hexagonal PMT (R10789-11) and the circuit in the bleeder

Table 3.2 shows the natural abundance of the isotope Xe. Xe has many isotopes. The differences in the interaction by spin has a advantage for WIMP search. The difference can be useful for the identification of WIMP by comparing the interactions in even and odd mass number. ^{129}Xe has the excited state of 39.58 keV. Therefore it has a possible to expect the inelastic scattering with WIMP.

Table 3.2: the natural abundance of the Xe

Isotope	^{124}Xe	^{126}Xe	^{128}Xe	^{129}Xe	^{130}Xe	^{131}Xe	^{132}Xe	^{134}Xe	^{136}Xe
abundance[%]	0.096	0.090	1.92	26.44	4.08	21.18	26.89	10.44	8.87

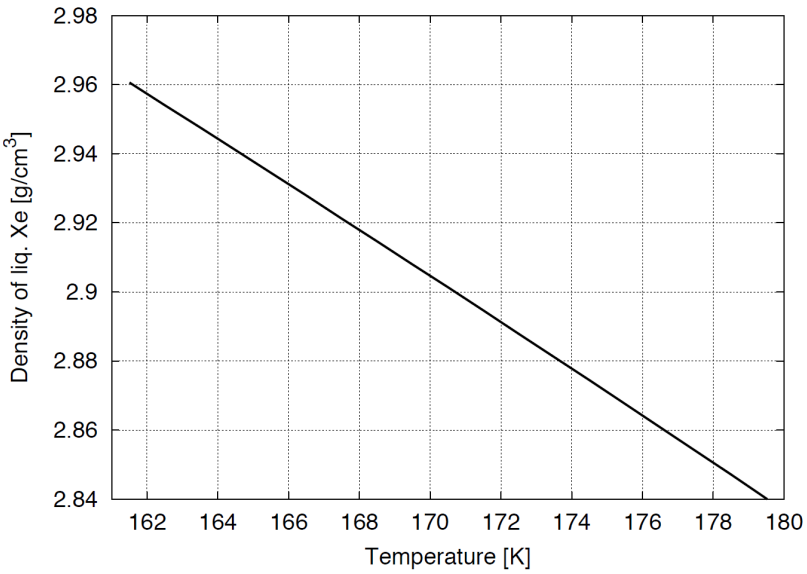

Figure 3.6: The density of Xe as a function of temperature.

3.3 Emission mechanism of Xe

Scintillation light in LXe is produced during the following two case (excitation: Eq. 3.1 and recombination: Eq. 3.2) [34].

Excitation light

$$\begin{aligned} Xe^* + Xe &\rightarrow Xe_2^* \\ Xe_2^* &\rightarrow 2Xe + h\nu \end{aligned} \tag{3.1}$$

Recombination light

$$\begin{aligned} Xe^+ + Xe &\rightarrow Xe_2^+ \\ Xe_2^+ &\rightarrow Xe^{**} + Xe \\ Xe^{**} &\rightarrow Xe^* + heat \\ Xe^* + Xe &\rightarrow Xe_2^* \\ Xe_2^* &\rightarrow 2Xe + h\nu \end{aligned} \tag{3.2}$$

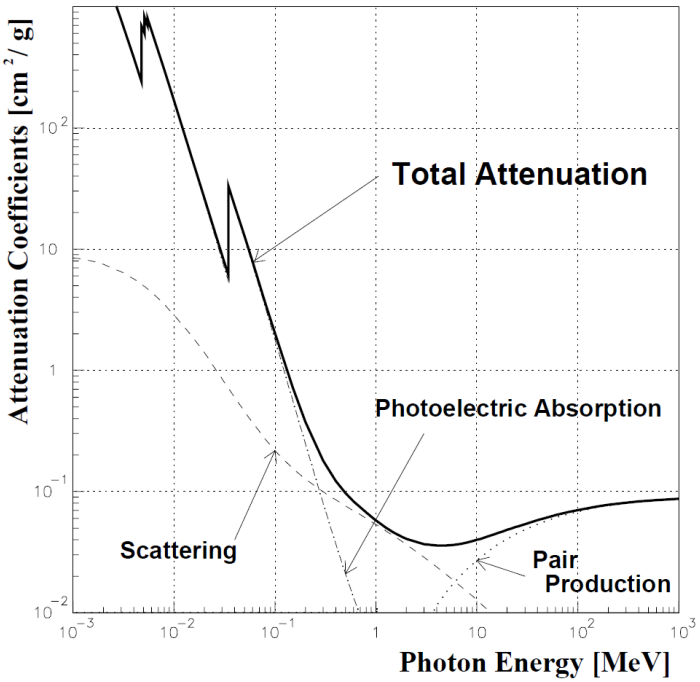

Figure 3.7: Attenuation coefficient of γ ray on Xe [33]

In these processes is scintillation lights of vacuum ultraviolet with a wavelength of 175 nm are emitted from dimer Xe_2^*. Table 3.3 shows various properties of LXe. From Table 3.3, when electrons travel in LXe, a decay constant of slow component by the recombination light has a different significantly from those for heavy ions and α particles. The reason can be explained from the light-emitting process of recombination light in Eq. 3.2. For heavy ions and α particles have a high dE/dx, ion pairs density of Xe^+ and e^- is higher than that of electrons. Therefore. decay constant of heavy ions and α particles is smaller than that of electrons for the high probability of pair production of Xe^+ and e^-. For excitation light, the influence of the difference in dE/dx is small for Xe^+ which react with near by Xe. A fast component of the excitation light by a electron can not be measured to be hidden by a slow component. Then this fast component can be measured by attenuating the slow component of recombination light using a electric field. This decay constant is the same of those by heavy ions and α particles. The decay constant of scintillation light in LXe are different by various charged particles. There is a possibility for particle identification by using the pulse shape discrimination to discriminate the difference of decay constants for the electron and neutralino or neutron.

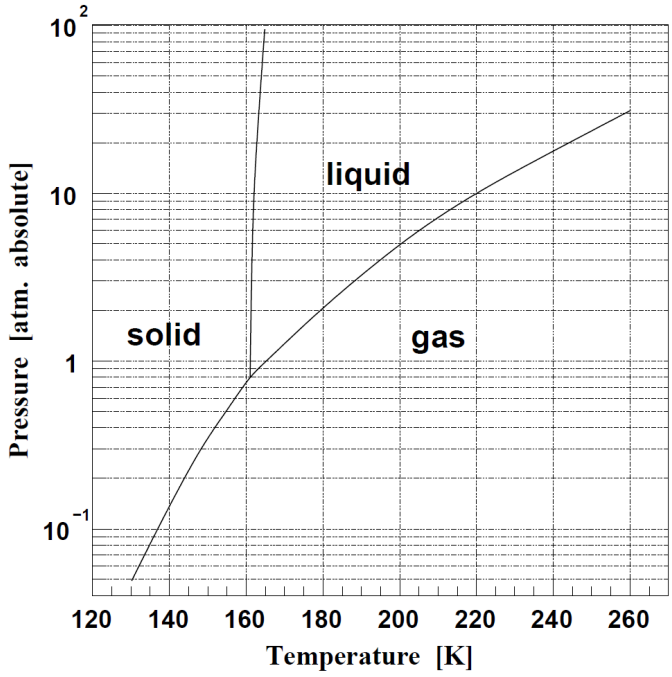

Figure 3.8: Phase diagram of Xe

3.4 Xenon circulation system

It is possible to perform circulation of Xe to remove impurities in Xe in the XMASS experiments. Radioactive sources in Xe is removed using Charcoal filter or Getter during circulation. Summary of Xe circulation system is shown in the Figure 3.9. The "Ugai" work for removing contaminations was done before the data taking. Xe after distillation process for removing Kr was stored in 700 ℓ tank, and transfer into the 800 kg detector through the Getter to impurity such oxygen and water in Xe. And Xe was back to 700 ℓ tank through the filter housing. The purpose of this work is to remove impurities in Xe. After finishing this work, LXe was filled again in the 800 kg detector. Currently, Xe circulation for removing radioactive source (Rn) has not yet been done. This is a next step of the XMASS.

Table 3.3: Properties of LXe

Property	value	condition	reference
atomic number	54		[35]
Mass number	131.29		[35]
Boiling point	165.1K		[35]
Melting point	161.4K		[35]
Density	$2.96 g/cm^3$	161.5K	[36]
Radiation length	2.77 cm		[36, 37]
Wavelength	175nm		
Refractive index	1.61	177±5nm	[38]
Energy per scintillation photon	21.6±2.8eVee		[39]
Slow component of electron	45ns	electron, γ ray	[40]
Fast component of α particle	4.2ns		[40]
Slow component of α particle	22ns		[40]
Absorption length	≥100cm		[41]
Rayleigh scattering length	∼60cm	$^nXe = 1.61$	[41]

3.5 Data acquisition

3.5.1 ATM

We used Analog Timing Module which (ATM) was previously used in the Super-Kamiokande experiment. Specifications are summarized in Table 3.4. Data acquisition by 66 Analog Timing Module (ATM) boards was performed for signals from 72 20-inch PMTs coming from water tank and from 642 2-inch PMTs coming from the 800 kg detector in the XMASS experiment. Then the signal is amplifier by a factor 10 and was divided into two signals. One of them sent to the ATM, other one was sent to the FADC, which is not used for the analysis in this thesis. One board of ATM can handle a signal form 12 PMTs. The signal of PMT is divided into four signals as shown in Figure 3.10. A one of the signal is fed into a discriminator which is set 0.2 photoelectrons (PE) corresponds to the threshold of 400 mV after 100 times amplification. Figure 3.11 shows the data acquisition flowchart. When pulse height of the signal exceeded the threshold, A HIT signal, which is a square wave signal of 11 mV height and of 200 ns width was generated. 12 HIT signals were summed and output as a HITSUM signal. After a HIT signal was generated, the PMT signal vetoed for 900 ns. Charge of time-

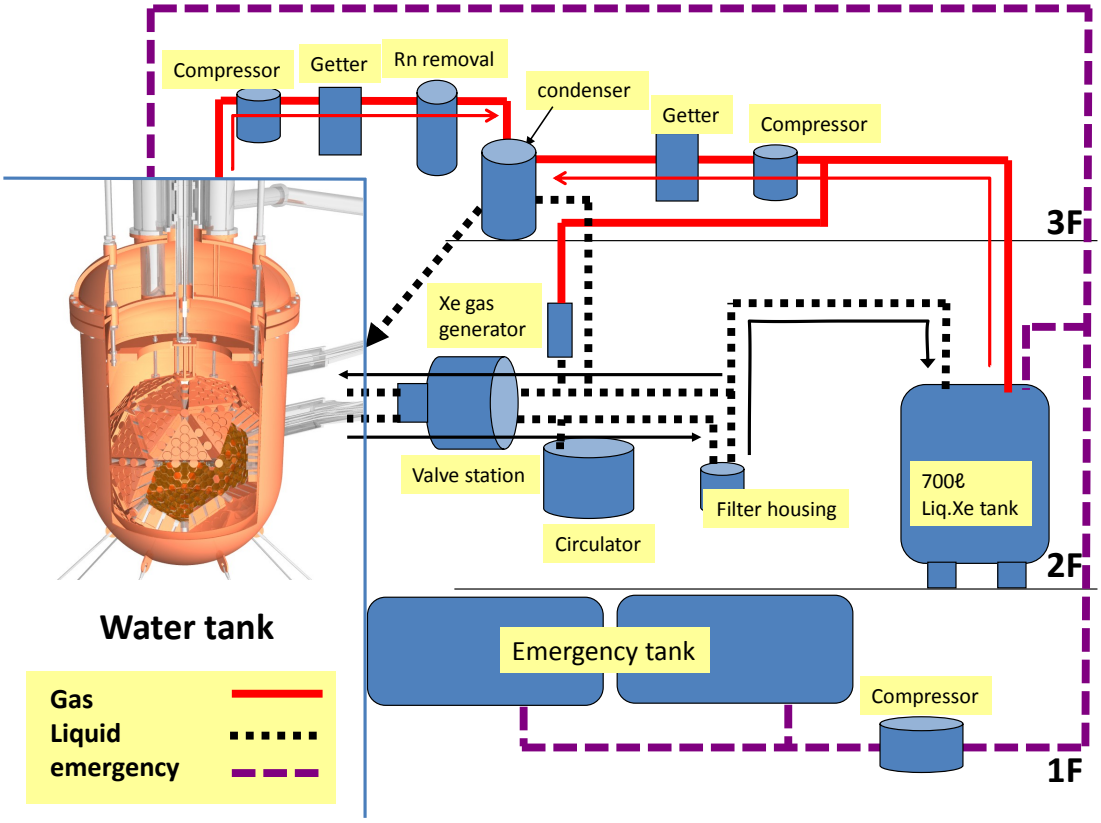

Figure 3.9: Xe circulation

to-analog converter (TAC) was initiated by a HIT signal and finished by a global trigger. Another signal from the PMT was sent to charge-to-analog converter (QAC). Charges were integrated over 400 ns. If the global trigger did not arrived within 1300 ns after the HIT signal, charge of QAC and TAC were discarded. AD conversion of the charge stored in the capacitor of the TAC/QAC was initiated, if the global trigger was arrived. The dead time of measurement can be reduced by two QAC/TAC for each channel.

Table 3.4: Specifications of the ATM

ADC/TDC resolution	12 bit
ADC dynamic range	0∼400 pC
TDC dynamic range	0∼1μs

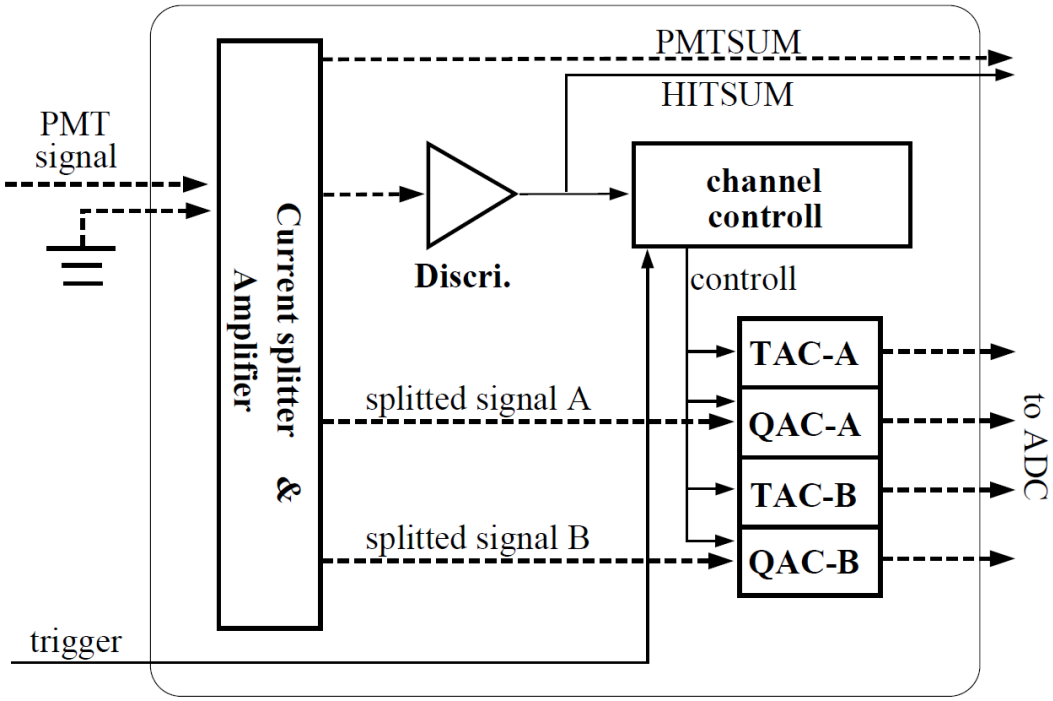

Figure 3.10: ATM board[60]

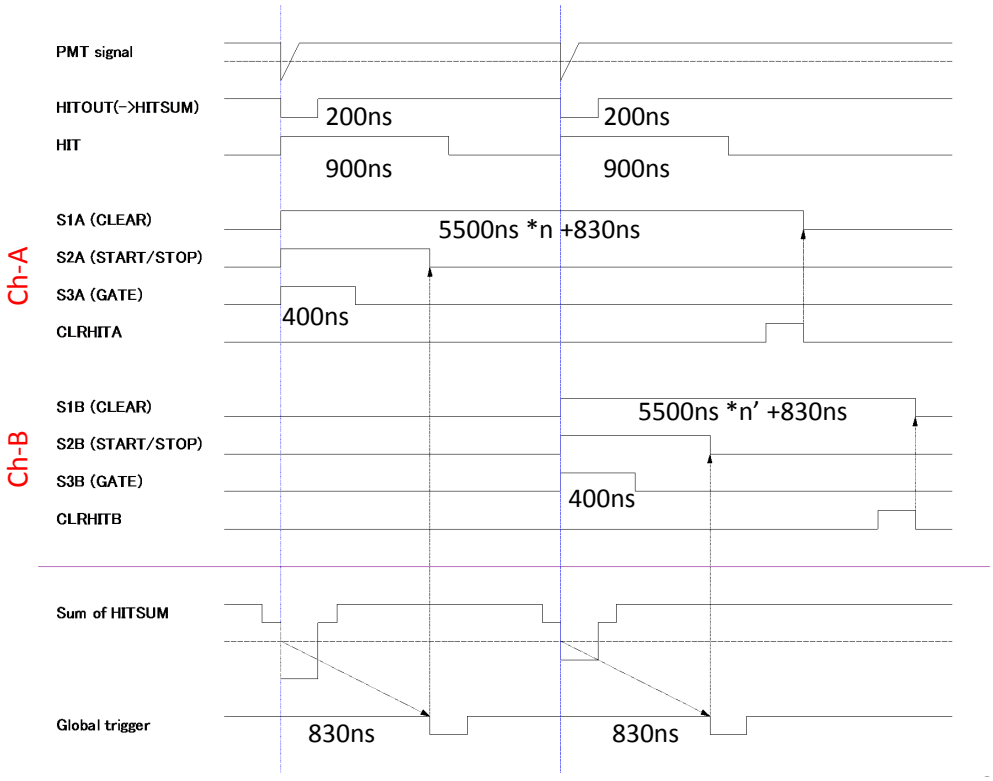

Figure 3.11: Data acquisition flowchart of ATM

3.5.2 Trigger logic

Figure 3.12 shows the DAQ logic of XMASS. The XMASS detector consisted of two parts, Inner Detector (ID) as a LXe detector and the Outer Detector (OD) as a water Cherenkov detector. In ID, signals from 642 PMTs were input to the preamplifier of the back of the ATM in TKO crate to produce a trigger from an analog sum signal of HITSUM signals. This trigger threshold was set to - 100 mV equivalent of 10 PMT hits. In OD, signals from 72 PMTs were input to the 6 ATMs. Trigger of OD hits was generated from HITSUM signal as same as ID. Threshold of this trigger was -80 mV equivalent of 8 PMT hits. A global trigger was generated by OR of trigger of ID and OD. Then this global trigger was sent to all the ATM modules.

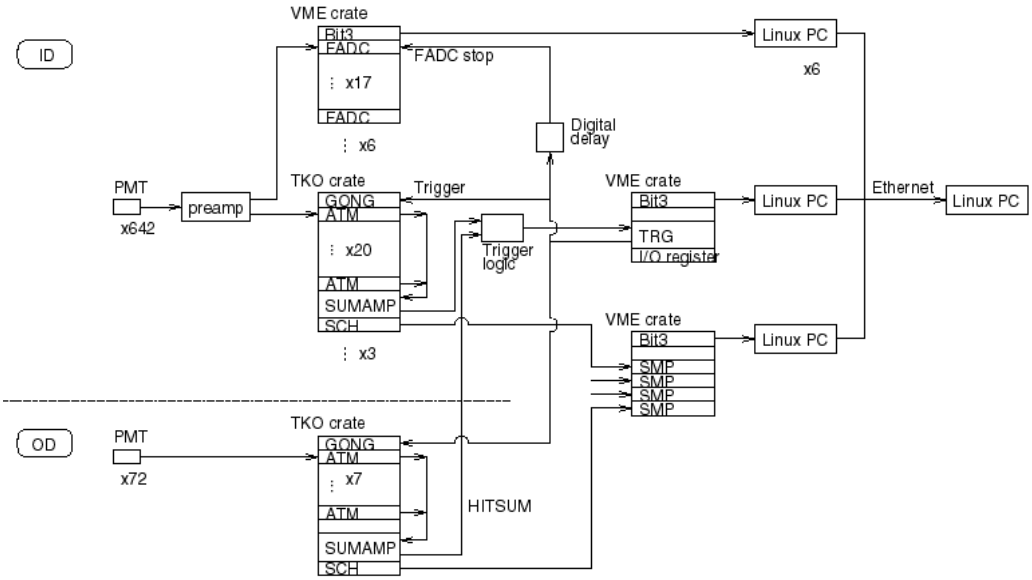

Figure 3.12: DAQ logic for XMASS.

A global trigger was made when sum of HITSUM signals of ATM exceeded 100 mV (10 hits) in the 200 ns window.

3.6 Detector simulation

A complete XMASS detector Monte Carlo (MC) simulation package based on Geant4 [61, 62] including the readout electronics has been developed [59]. Figure 3.13 shows the structure of the 800 kg detector, 2-inch PMT, and PMT holder. The MC reproduced the photon propagation and radiation interaction. It is important to understand vertex reconstruction and background evaluation for the XMASS experiment. Understanding and an evaluation of the detector were performed using a simulation and detector calibration. The MC has been tuned using calibration data and the optical properties of the LXe. The energy dependence of the light yield as well as the energy resolution were tuned on calibration data, as were the decay constant of gamma induced scintillation light and the transit timing spread (TTS) of the PMTs. We choose these constants so that we can reproduce the observed distribution of PMT hit timing in our simulation. The effective decay constant τ_γ thus determined is 27.3 ns for a 39.58 keV gamma ray and the TTS is 2.33 ns (rms).

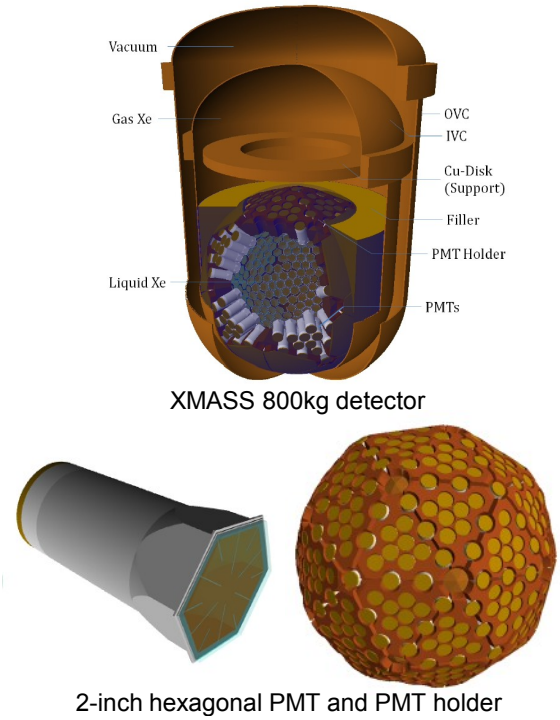

Figure 3.13: Structure of XMASS detector.

3.6.1 Energy estimation

Total photoelectron was converted to the scaled energy by multipling a factor of 13.9 p.e./keV. This value was determined using calibration data of ^{57}Co at the center of ID. The value does not take into account position dependence of energy.

3.6.2 Vertex reconstruction

Vertex reconstruction was carried out with the information of nPE pattern from the detector [59]. For various grid positions inside the ID, expected nPE in each PMT was calculated with the MC. We use positions on a Cartesian grid, on radial lines from the center of the detector, and on the inner surface of the detector including gaps between PMTs. These expected $nPEs$ are normalized so that can be calculated probability density functions (PDFs) for each grid position. The probability, $p_i(n)$ that the i-th PMT detects nPE is calculated using the PDF. The likelihood that the vertex is at the position $\mathbf{x}$ is the product of all $p_i(n_i)$;

$$L(\mathbf{x}) = \prod_{i=1}^{642} p_i(n_i), \tag{3.3}$$

where n_i represents nPE for the i-th PMT. The most likely position is obtained by maximizing L.

Chapter 4

Background

In the XMASS experiment, it is important point is to suppress a background in order to search for a dark matter signal. The background is classified into two categories, internal and external backgrounds, regarding as their origins are located inside or outside of the detector. In this Chapter, internal and external backgrounds are described for the XMASS experiment.

4.1 External background

Cosmic rays interact with the atmosphere of the Earth and many muons are produced by a decay of secondary cosmic rays. They reach at the ground and become a big background source for dark matter searches. Therefore the detector is located at 1000 m underground in the Kamioka-mine to reduce the effect of muons. Table 4.1 shows the radiation circumstance at the underground. A rate of muon become a 10^{-5} times of that for the ground. The 800 kg detector was shielded against external background, such as neutrons or gamma rays, by the water tank filled with the ultra pure water. In addition, the gap space inside of the water tank was filled with Super Rn Free Air. Super Rn Free Air is external air after reduction of Rn by a charcoal filter. Thanks to this Rn concentration in the water tank was kept much lower than the typical Rn concentration in the mine. The experimental cavern was filled also by external air supplied from out side of the mine.

The background neutrons can be categorized into 3 types according to their production mechanism.

- The nuclear spallation reaction by cosmic ray muon.
- The fission reaction by U and Th chain in the rock.

Table 4.1: The background of the laboratory in the Kamioka-mine

	Ground	Laboratory
$\mu[/cm^2/s]$[44]	1.1×10^{-2}	$\sim 10^{-7}$
Thermal neutron $[/cm^2/s]$ [45]	1.4×10^{-3}	8.26×10^{-6}
Neutron except for thermal$[/cm^2/s]$[45]	1.2×10^{-2}	1.15×10^{-5}
Rn[Bq/s] (Summer) [46]	40	1200
Rn[Bq/s] (Winter) [46]	40	40
γ rays $[/cm^2/s](>500keV)$	-	0.71

・ The (α, n) interaction between material in the rock and α particle produced by decay of U and Th

Neutrons are classified as thermal neutron (E<0.5 eV) and fast neutron (E>500 keV) according to their energy. In order to achieve the same background level as the γ rays background in the 800 kg detector, thermal neutron and fast neutron must be reduced by 4th order and 2nd order, respectively. This background level can be achieved by using the water tank as a neutron moderator.

4.2 Internal background

The internal background in LXe can not be reduced by the water tank and the self shielding effect. Therefore, the internal background need to be removed using the Xe circulation and the distillation. The internal background in LXe is shown as follows.

4.2.1 Uranium chain

A ^{238}U has a long half-life (4.468×10^9 y). Figure 4.1 shows a decay chain of ^{238}U until a stable nuclide. β rays and low energy γ rays in this chain become background events in the low energy region where dark matter signal would appear. A Rn in this chain would contaminate to the LXe. It is necessary to examine amount of Rn during removal of the background. The amount of ^{222}Rn was deduced from the analysis by using the delayed coincidence of two successive decays as $^{214}\mathrm{Bi} \rightarrow {}^{214}\mathrm{Po} \rightarrow {}^{210}\mathrm{Pb}$ (Figure 4.2) assuming the radiative equilibrium. The amount of ^{222}Rn was a 0.28 mBq/835 kg.

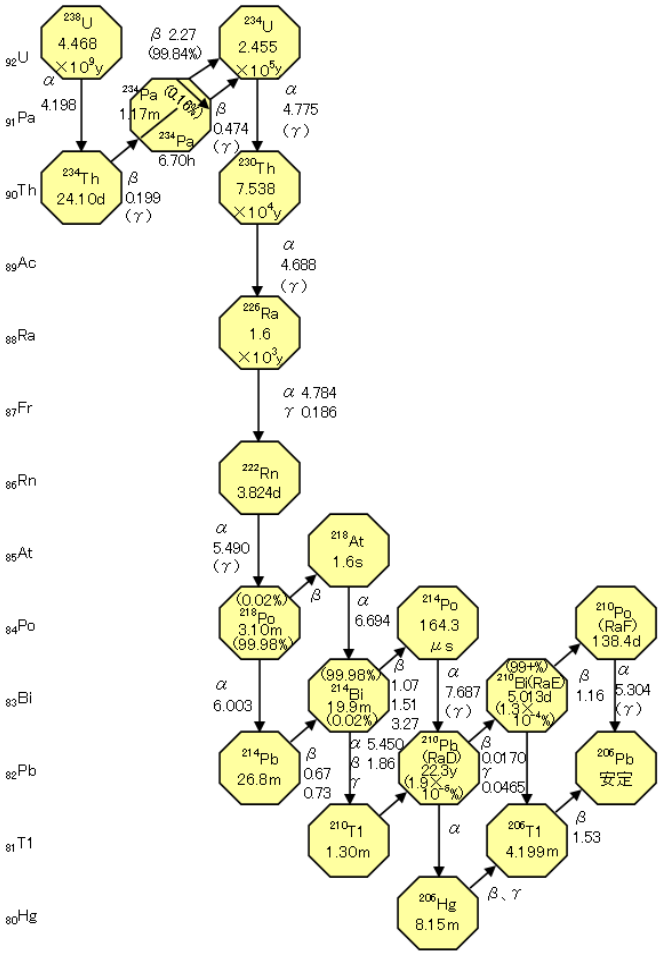

Figure 4.1: A decay chain of ^{238}U

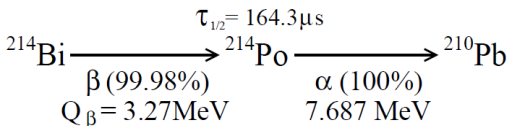

Figure 4.2: The ^{214}Bi sequential decay

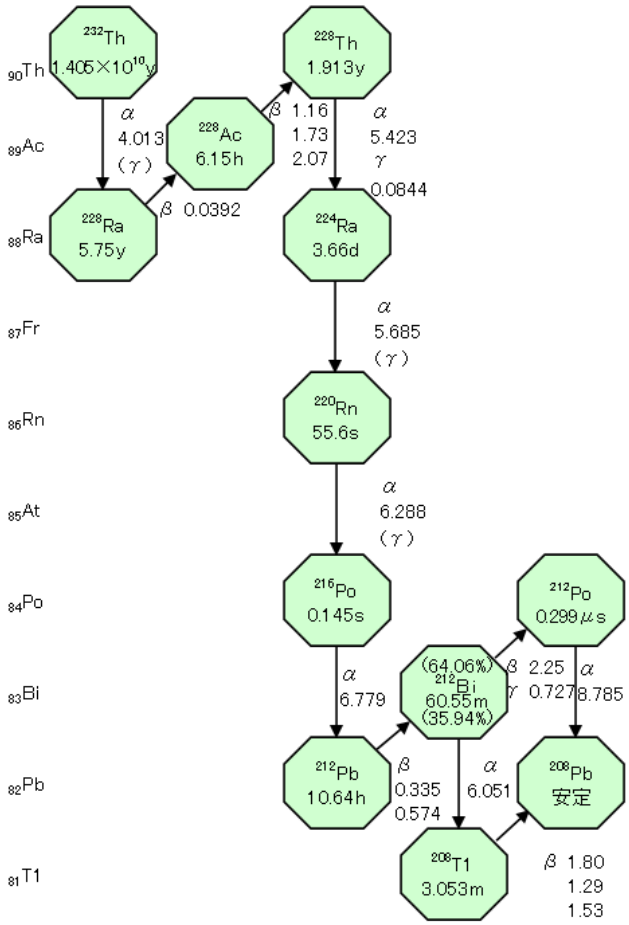

Figure 4.3: A decay chain of ^{232}Th

4.2.2 Thorium chain

A ^{232}Th has also a long half-life (1.405×10^{10} y). Figure 4.3 shows a decay chain of ^{232}Th until a stable nuclide. β rays and low energy γ rays in this chain also become the background. The amount of ^{220}Rn was evaluated from the analysis by using the delayed coincidence of two successive decays as $^{220}\mathrm{Rn} \rightarrow {}^{216}\mathrm{Po} \rightarrow {}^{212}\mathrm{Pb}$ (Figure 4.4) assuming the radiative equilibrium. The amount of ^{220}Rn was a 8.2 ± 0.5 mBq/835 kg.

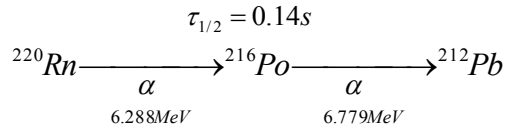

Figure 4.4: The ^{220}Rn sequential decay

4.2.3 ^{85}Kr

A ^{85}Kr has a half-life of 10.756 y. Figure 4.5 shows a decay of ^{85}Kr until a stable nuclide. This ^{85}Kr was produced by reactors and was included in the atmosphere. Therefore the ^{85}Kr was mixed in Xe when Xe was extracted from the atmosphere. The ^{85}Kr was removed by a Xe distillation system. The distillation work actually was done at 2010 before filling LXe. An abundance ratio of Kr(mol)/Xe(mol) was obtained to be less than 2.7 ppt by the measurement of gas sample of our detector [47]. This value gave

$$^{85}Kr/Kr = (0.61 \pm 0.19) \times 10^{-11}. \tag{4.1}$$

99.563% of ^{85}Kr decay to the ground state by β decay. The Q_β value of this β decay is 687 keV. Therefore, a component of β ray overlaps in the WIMP signal region. 0.434% of ^{85}Kr decay to ^{85}Rb*, the excitation state of ^{85}Rb, and ^{85}Rb* emits a γ ray of 514 keV with $\tau_{1/2}$=1.015μs. ^{222}Rn in U chain can be removed by a charcoal filter for LXe. Circulation of Xe in a gas phase with a charcoal filter was done in the commissioning runs. But LXe circulation with a charcoal filter has not been done. The ^{85}Kr background was actually removed by the distillation by using difference in the boiling points of Kr and Xe. Table 4.2 shows the remaining backgrounds in LXe by the gas measurement [59]. The background level of Th chain and ^{85}Kr almost satisfied the target value. The background level of ^{222}Rn in U chains was higher by 1 order than the target value. The background level of only internal events only was 10^{-4} keV^{-1} day^{-1} kg^{-1}. Also a expected background level of 2-inch PMTs in the detector materials was 10^{-2} keV^{-1} day^{-1} kg^{-1} for the full volume of the detector and 10^{-4} keV^{-1} day^{-1} kg^{-1} for the central part of LXe in the detector. These numbers were used to estimate a number of the expected background events with MC as discussed later. The amount of ^{85}Kr can be measured for the read data by using the delayed coincidence method without the measurement of gas sample in future.

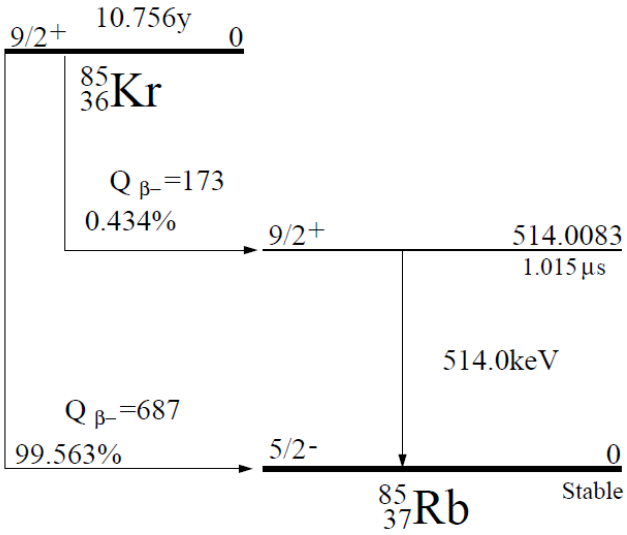

Figure 4.5: The ^{85}Kr decay

Table 4.2: Result of internal background

Contamination	measurement
U chain	8.2±0.5 mBq/835 kg
Th chain	0.28 mBq/835 kg
Kr(mol)/Xe(mol)	<2.7 ppt

4.2.4 Background from PMT Al seal

The background level of the commissioning run data was higher than the expectation. This was found to be due to more surface background than expected. Because aluminum components (sealing material between the PMT body and its window), i.e. Al seal, contact to LXe of the sensitive region, β rays from a radioactive isotope possibly contribute to the background. Events on the surface of a quartz window of the PMT can be easily identified using a information of PMT hit pattern. On the other hand, events in the gap region between the PMT and the PMT holder may be more difficult to identify using only hit pattern information, resulting vertex mis-reconstruction. In order to identify the cause of the background, Al seal was examined for their contribution of low energy γ rays and to the related β rays by a High-purity Germanium (HPGe) Detector. Significant amounts of ^{238}U, ^{214}Pb and

^{234}Th were found in aluminum samples [59]. Figure 4.6 shows the Al seal together with the estimated energy spectrum deduced from the background MC with the results of HPGe detector measurement, and the observed data in the XMASS detector. The expected background level and the observed data had a good agreement with the level of $\sim 1\,\mathrm{keV}^{-1}\,\mathrm{day}^{-1}\,\mathrm{kg}^{-1}$ for the full volume of the detector. Background MCs for producing the expected background spectrum have been modified to match in the error of HPGe Detector measurement.

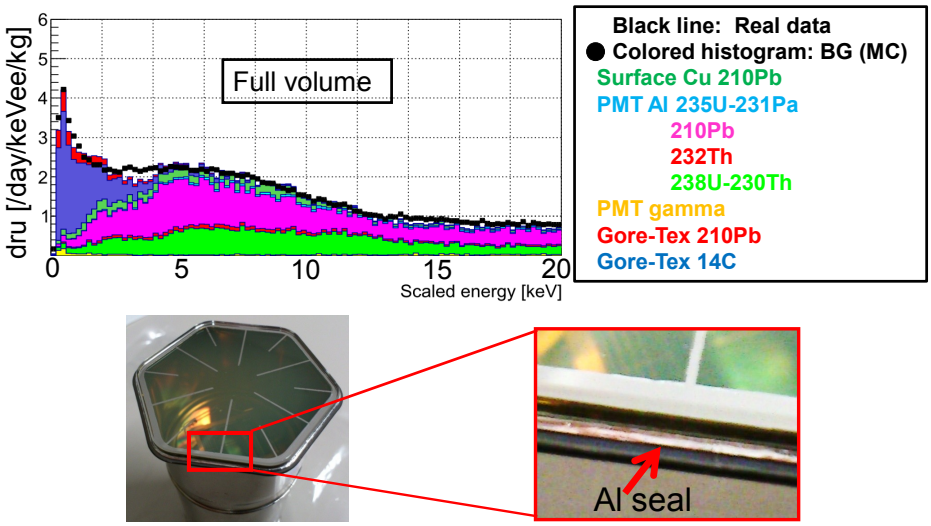

Figure 4.6: PMT Al seal and the results from the background MC and data.

Chapter 5

Detector calibration

For investigating response of the XMASS detector, we performed detector calibrations as follows. A LED calibration corrected the 1 p.e. gain of PMTs and electronics. An inner radioactive source calibration corrected the energy scale with ^{57}Co calibration data at the center position, the response with ^{57}Co or ^{241}Am calibration data at various vertical positions, and the hit timing. The γ ray injection from outside of the OVC was used to investigate the effect of external backgrounds.

5.1 LED calibration

An investigation of PMT gain stability was performed by a LED calibration. Eight LEDs of blue light with Teflon diffuser were installed at the surface of PMT holder in ID. Low occupancy LED data were taken with every week for obtaining the PMT 1 p.e. data. The PMT gain was found to be stable within $\pm$5% [59].

5.2 Hose calibration

Hose calibration performed investigations of the response from external backgrounds and a effect of inner surface events [59]. The hose calibration system was attached to the outside of the OVC using an U-shaped soft hose such as Figure 5.1. Radioactive sources were set inside of the hose and moved around the ID through the hose.

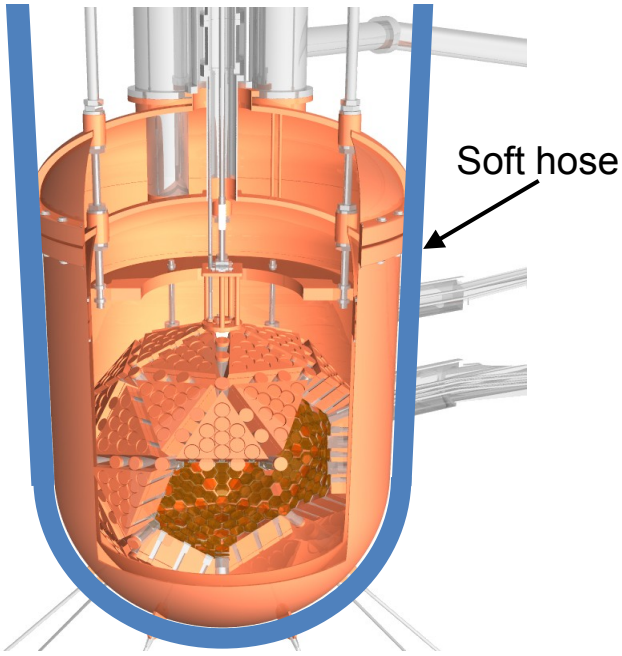

Figure 5.1: The hose calibration system. Radioactive sources moved inside of the hose.

5.3 Source calibration

An inner source calibration system can insert a radioactive source inside ID [59]. Figure 5.2 shows the calibration system which consists of an OFHC copper rod and a radioactive source. The radioactive source can be installed at the tip of the copper rod. Then this system moved a rod in the vertical direction remotely by a stepping motor with precision of better than 1 mm. The source used in the XMASS experiment are listed in Table 5.1. The ^{241}Am and ^{57}Co had a diameter of 0.21 mm, which is much smaller than the absorption lengths for 59.5 and 122 keV gamma rays in LXe ($\sim$0.44 mm and $\sim$2.5 mm, respectively). The ^{241}Am and ^{57}Co were used in the inelastic scattering analysis for the correction of energy scale and evaluation of systematic errors. Figure 5.3 shows the reconstructed vertex of MC and real data for the ^{57}Co calibration data. The position resolution was 1.4cm (RMS) for 122 keV gamma rays. Energy scale in Figure 5.4 was determined by the 122 keV peak of ^{57}Co calibration data. The energy resolution was 4 % (RMS) for 122 keV gamma rays. The ^{241}Am data was used to check the energy scale uncertainty

for the inelastic scattering analysis. Uncertainty of energy resolution was estimated from the difference between the energy scale determined by the 59.5 keV peak and that by ^{241}Am for inelastic scattering analysis.

Table 5.1: Calibration sources and energies. The 8 keV (*1) in the ^{109}Cd and 59.3 keV (*2) in the ^{57}Co source are K_α X-rays from the copper and tungsten, respectively, used for source housing.

Isotopes	Energy [keV]	Shape
^{55}Fe	5.9	cylinder
^{109}Cd	8(*1), 22, 58, 88	cylinder
^{241}Am	17.8, 59.5	thin cylinder
^{57}Co	59.3(*2), 122	thin cylinder
^{137}Cs	662	cylinder

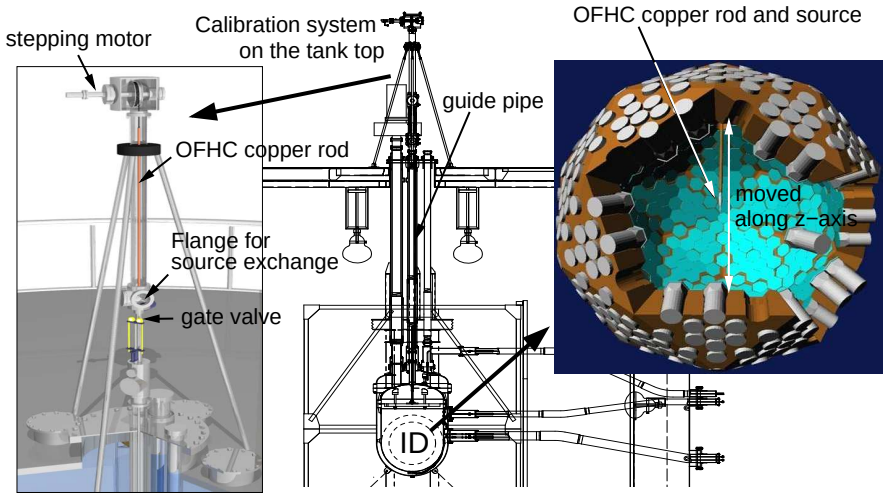

Figure 5.2: Calibration system. Radioactive source set on the tip of the copper rod is installed in the ID and can be moved the vertical axis.

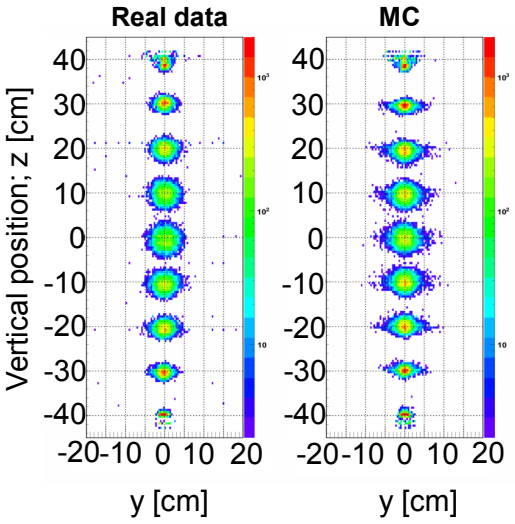

Figure 5.3: The reconstructed vertex distribution of ^{57}Co calibration data (122 keV).

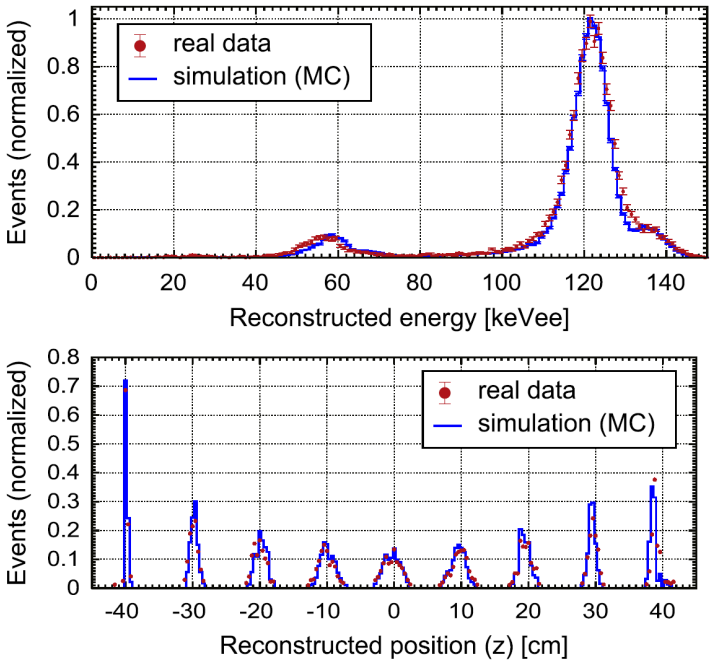

Figure 5.4: The energy spectrum and reconstructed vertex distribution of ^{57}Co calibration data and its MC at 122 keV.

Chapter 6

Analysis of WIMP - ^{129}Xe inelastic scattering

6.1 Detector simulation for inelastic scattering

As discussed in the Chapter 2.6 both nuclear recoil and a 39.58 keV de-excitation gamma ray are observed in a WIMP - ^{129}Xe inelastic scattering. The expected combinations of excitation and nuclear recoil were used to simulate events. In the simulation, a nuclear recoil (decay constant $\tau_{nr} =$ 25 ns [29]) and a γ ray with 39.58 keV were simulated at their common vertex in the detector. Here we ignored a few percent difference of K shell and L shell electron ejection probability after de-excitation and gamma ray absorption. These vertices were distributed uniformly in the inner detector. The half life of the excited state can be ignored since it is much faster ($\sim$1 ns) than the decay constant of scintillation light. Figure 6.1 shows the simulated energy deposits for WIMPs with various masses.

6.2 Data reduction

The data used for this search was taken between December 24, 2010 and May 10, 2012, and amounts to a total live time of 165.9 days. Since we took extensive calibration data and various special runs to understand the background and the general detector response, we selected runs taken under what we designated "normal running conditions" with stable temperature and pressure (0.160-0.164 MPa absolute). Additional data quality checks rejected runs with excessive PMT noise, unstable pedestal levels, or abnormal

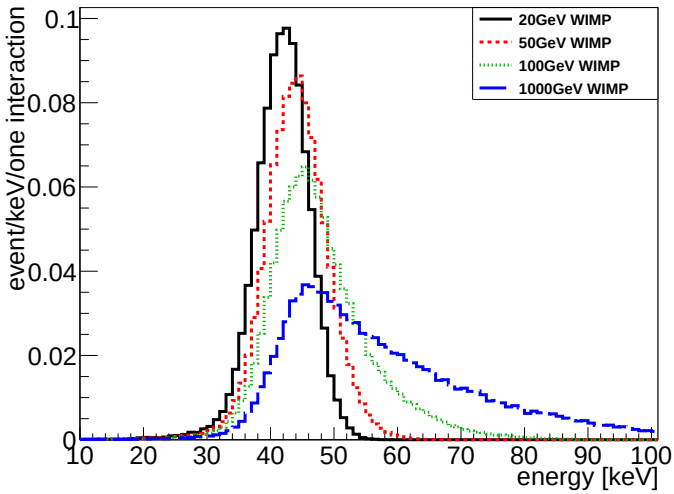

Figure 6.1: Simulated energy spectra for the WIMP mass with 20 (solid line), 50 (dashed line), 100 (dotted line), and 1000 GeV (long dashed line). The energy is defined by dividing the number of photoelectrons observed by 13.9 (p.e./keV).

trigger rates.

As discussed in Ref. [64, 11], most of the observed events are background events due to radioactive contamination in the aluminum seals of our PMTs and radon progeny on the inner surface of the detector. To reduce these backgrounds, a dedicated event reduction procedure was developed for this analysis. In this Chapter we give a detailed description of this reduction procedure in four step and our evaluation of its acceptance.

6.2.1 Cut (1); Pre-selection

This is similar cut used in Ref. [64]. The Pre-selection is based on the ID trigger, the time difference between a event and next to it, and RMS of hit timing distribution. Figure 6.2 shows the energy spectrum of ID trigger events. Only ID events were selected in this analysis. Figure 6.3 shows the time difference between a event and the previous event (dTpre) and that between the event and the following event (dTpost). In order to remove the event caused by the tail of the scintillation light emission the event of which time difference to the previous event was less than 10 ms were rejected. In order to remove the event caused by ^{214}Bi, a daughter of ^{222}Rn, in the

detector, the event that the following event was loss than 10 ms were rejected. Figure 6.4 shows the TDCRMS distribution of the observed data and 50 GeV signal MC. The event of which hit timing distribution has RMS of more than 100 ns were also removed. These cuts did not have significant impact on the signal efficiency.

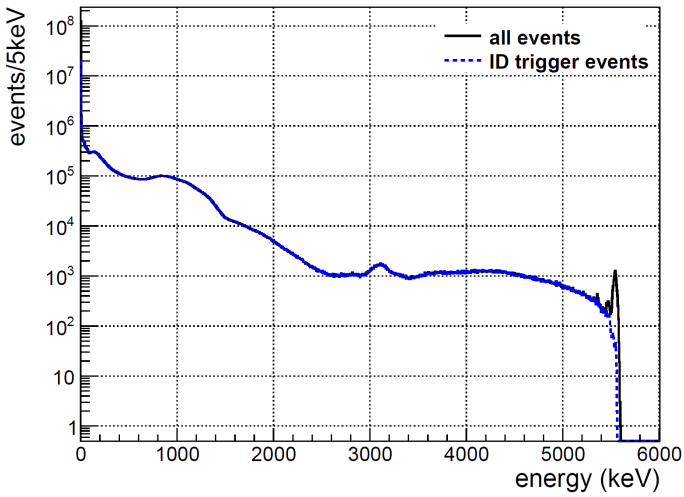

Figure 6.2: The energy spectrum of all the triggered events and ID trigger events.

6.2.2 Cut (2); Fiducial volume cut

As is described in Chapter 3.6.2, Figures 6.5 and 6.6 show the radius cut parameter distribution after the pre-selection of signal MC and that of observed data,respectively. The observed pattern of photoelectrons was used to reconstruct the event vertex. The radial position R of an event was obtained from this reconstruction.

6.2.3 Cut (3); Timing cut

Figures 6.7 and 6.8 show the timing cut parameter distribution after the radius cut of signal MC and that of observed data, respectively. Even after the radius cut, some surface events remain in the sample. Timing information was used to further reduce these remaining surface background events. Here we used the timing difference δT_m between the first hit and the average of

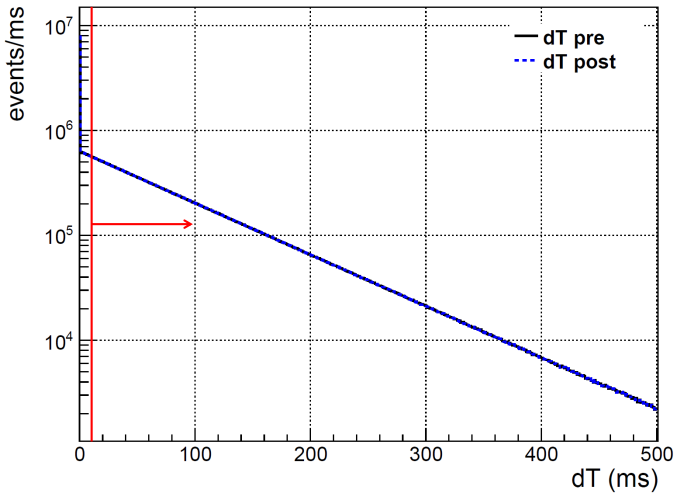

Figure 6.3: dTpre and dTpost distributions after event selection of ID trigger.

hit timings of first 50% PMT signals except the first 10 hits. A larger timing difference indicates of a surface event.

6.2.4 Cut (4); Band cut

Figures 6.10 and 6.11 show the band cut parameter distribution after the timing cut of signal MC and that of observed data, respectively. Grooves and gaps exist between PMTs. Scintillation light caused by events inside those grooves have a characteristic pattern like a Figure 6.9. This pattern emerges because the propagation of scintillation light from within a groove is constrained by the rims of the groove, and its characteristic band shape can be identified. Events with such a pattern are eliminated by this cut. An axis is defined by the geometric center of the detector and the reconstructed event vertex. This axis intersects the approximately spherical inner detector surface in two opposing points. We select PMTs within bands extending ± 7.5 cm around great circles through these two points. In a first step we determine the great circle for which the p.e. count of the PMTs within in its band becomes maximal. We next check planes parallel to that in which the selected great circle lies in an effort to further maximize the integral p.e. count on PMTs within a 15 cm wide band around these parallel planes. Again we select the plane with the maximal p.e. count in its 15 cm wide band. This determines the maximal p.e. count in a 15 cm wide band, which

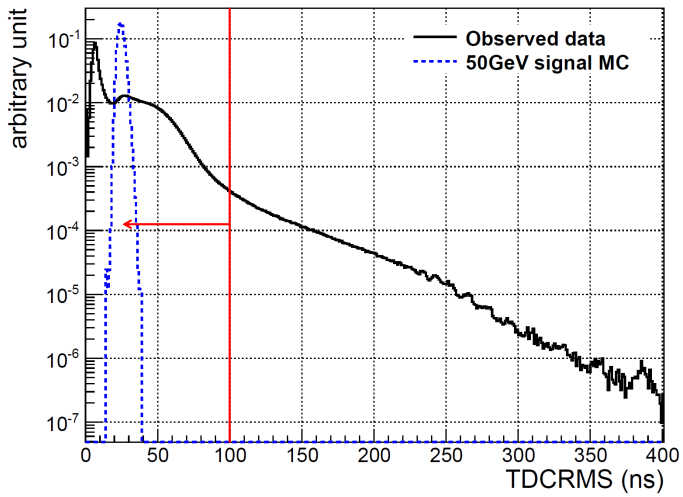

Figure 6.4: The TDCRMS distribution of observed data after dTpre and dTpost cut. Also shown the TDCRMS distribution of 50 GeV signal MC as the dotted histogram.

defines our cut parameter as follows;

$$\text{Band cut parameter } F_B = \frac{\text{Maximum p.e. in a band of width 15 cm}}{\text{Total p.e. in the event}}. \quad (6.1)$$

6.3 Cut optimization

The cut values for the three cuts above were optimized for a WIMP mass of 50 GeV. Other than the radius cut our cut values were determined by optimizing the ratio of remaining signal events in a signal range from 30 to 80 keV from our simulation over the sum of background events in two side bands ranging from 10 to 30 and from 80 to 100 keV. For the radius cut this procedure results in an extremely low fiducial volume, leading us to relax the cut to 15 cm. For the remaining cuts the values resulting from our optimization were 12.91 ns for the timing cut and a ratio of 0.248 for the band cut. Events with parameter values smaller than these cut values were chosen for the final sample. Figure 6.12 shows the example of the 2-dimensional plots of cut parameters when the band cut parameter is 0.248. When optimized cut parameters were chosen, the best signal and noise ratio

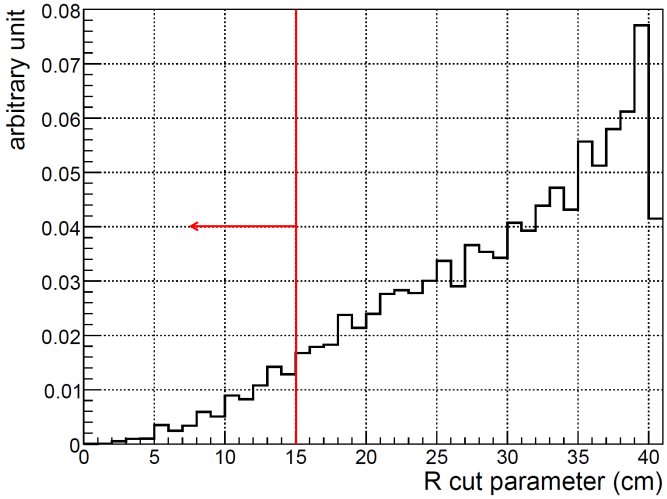

Figure 6.5: The radius cut parameter distribution of 50 GeV signal MC after pre-selection in the signal region from 36 to 48 keV.

was 63.4. Remaining events with 50GeV signal MC were 1,340 in signal range from 30 to 80 keV. Remaining background events were 16 (21.12 at 90 % C.L.) in two side bands ranging from 10 to 30 and from 80 to 100 keV. Figures 6.13, 6.14, and 6.15 show the impact of our cuts on the expected signal for WIMP simulation for each mass. As we did not apply the proper radial correction for energy, a shift in our energy scale seems to occur after our fiducial volume cut (2). As we are only using events in the very limited fiducial volume and the energy scale is based on calibration at the center of the detector, the energy scale of the surviving events was correct within 4 % Figure 6.16 shows the impact of our cuts on the expected signal from the observed data spectrum. The signal window was defined as 36-48 keV, so that it contained 90 % of the 50 GeV WIMP signal. These cut values and signal window optimized for the 50 GeV WIMPs were also used to obtain the limits for the other WIMP masses. A signal efficiency was defined as the ratio between the number of simulated events remaining after all cuts in the 36-48 keV signal region and the number of simulated events generated within the fiducial volume (radius less than 15 cm). It ranges from 29 % for 50 GeV WIMPs to 15% for 5 TeV WIMPs as shown in Table 6.1. Event rates after each cut are shown in Figure 6.17.

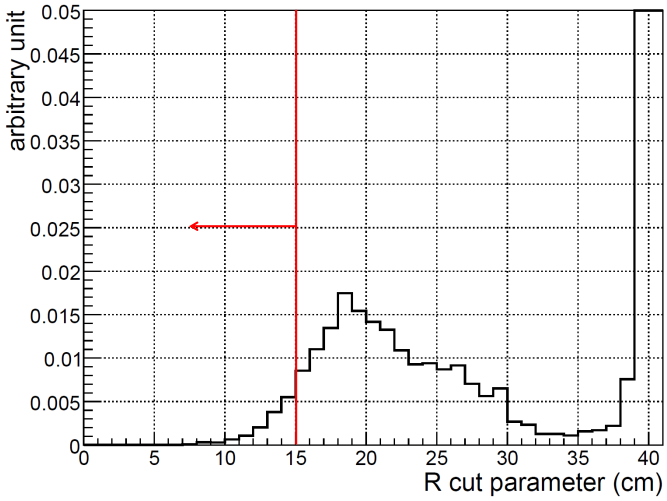

Figure 6.6: The radius cut parameter distribution of the observed data after the pre-selection in the signal region from 36 to 48 keV. The peak around the 20 cm region is due to vertex mis-reconstruction events.

6.4 Reduction of observed data

After each cut, event rates after the pre-selection, the radius cut, the timing cut, and the band cut were 6×10^{-1} Hz, 2×10^{-3} Hz, 4×10^{-4} Hz, and 10^{-6} Hz level from 10 to 100 keV region. They are stable and consist to statistical fluctuation. As clearly visible in Figure 6.16, the cuts discussed in previous Chapters almost eliminated all the background around the signal region. We could not find any significant signal around the signal region after all cuts. After all cuts, 5 events remained in the 36 to 48 keV signal region. The main contribution to the remaining background in this energy region was from ^{222}Rn daughter ^{214}Pb as shown in Figure 6.18. The radon concentration in the LXe was evaluated from data recorded in the XMASS detector itself. The obtained values was 8.2 ± 0.5 mBq for ^{222}Rn [59]. From our simulation we estimated this background alone contributes 2.0 ± 0.6 events. A probability to obtain more than 5 events was 5.3 % assuming the Poisson distribution when main radon concentration gave 2.0 ± 0.6 events. As other background contribution was considered to be smaller but less certain, we did not subtract background when calculating our limits.

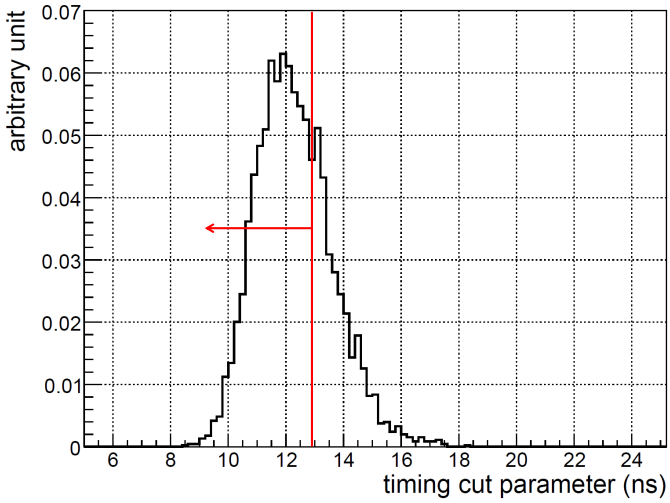

Figure 6.7: The timing cut parameter distribution of 50 GeV signal MC after the radius cut in the signal region from 36 to 48 keV.

6.5 Systematic error evaluation

The systematic uncertainty on our signal efficiency was estimated from data - MC comparisons for ^{241}Am calibration data (60 keV) at various positions within the fiducial volume. The relevant comparisons are shown in Figures 6.21, 6.22, 6.23, and 6.24. From these comparisons we derived systematic differences in the energy scale, the energy resolution, the radius reconstruction, the timing cut and the band cut parameter. There was uncertainty in the effective light yield $\mathcal{L}_{\text{eff}}$ and in the decay constants of nuclear recoils. The cumulative effect of these individual contributions was obtained by adding these errors in quadrature. As an example for our systematic error evaluation we explain it for the signal efficiency for 50 GeV WIMPs; see Table 6.2 for other masses.

6.5.1 Energy scale

The uncertainty in the energy scale was evaluated to $^{+4.6}_{-3.1}$ % by comparing more than 10 sets of calibration data (^{57}Co) taken at different times throughout the data taking period with our simulation as shown in Figure 6.21. Changing the number of photons generated per unit energy deposited in the simulation by this amount, the signal efficiency changes by $^{+11}_{-13}$ %.

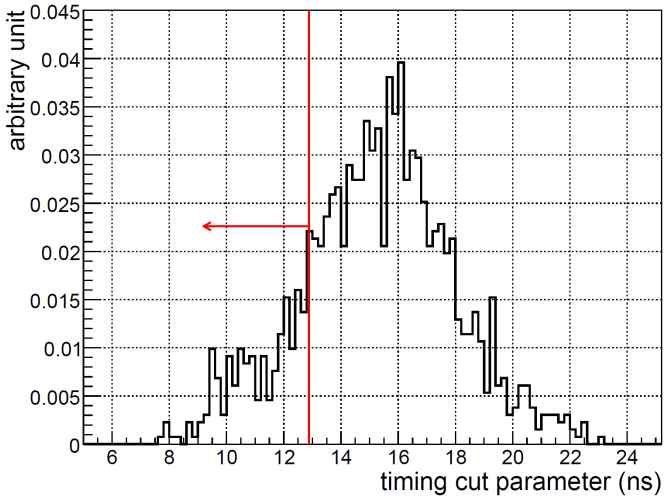

Figure 6.8: The timing cut parameter distribution of the observed data after the radius cut in the signal region from 36 to 48 keV.

6.5.2 Energy resolution

The uncertainty of the energy resolution was evaluated to be $\pm 12\,\%$ by comparing the resolution of the 60 keV peak in the ^{241}Am calibration data and the simulated events as shown in Figure 6.21. This led to 5.6 % reduction of the signal efficiency.

6.5.3 Radius cut

Figure 6.22 shows comparison of radius distributions between the ^{241}Am calibration data and the simulations. The radial position of the reconstructed vertex for the calibration data differs by 5 mm from the true source position, which caused 3.2 % reduction in the efficiency. This was taken in account $^{+0}_{-3.2}$ % systematic error.

6.5.4 Timing cut

Figure 6.23 shows comparison of timing cut distributions between the ^{241}Am calibration data and the simulations around the 60 keV region. These distribution have a slightly different impact on calibration data and simulated events. By taking the difference of its acceptance we evaluated the systematic

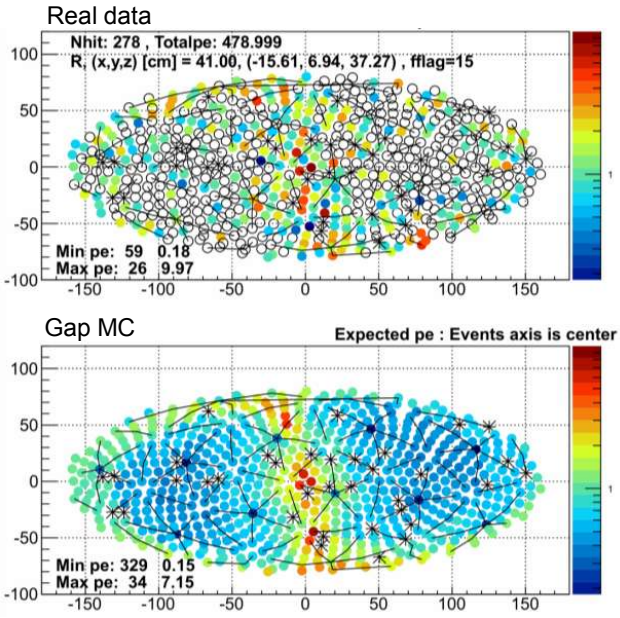

Figure 6.9: The upper figure shows an event pattern of band structure in real data. The lower figure shows an event pattern for gap simulation. This structure appears in cause by grooves and gaps.

impact on the signal efficiency as $^{+4.2}_{-5.1}$ %.

6.5.5 Band cut

Figure 6.24 shows comparison of band cut distributions between the ^{241}Am calibration data and our simulations with same energy region of the timing cut distribution. These distribution have a slightly different impact on calibration data and simulated events. By taking the difference of its acceptance we evaluated the systematic impact on the signal efficiency as $\pm 4.2\,\%$.

6.5.6 Scintillation yield

Figure 6.20 shows the effective light yield $\mathcal{L}_{\text{eff}}$ based on the nuclear recoil equivalent energy [63]. The $1\,\sigma$ uncertainty in the $\mathcal{L}_{\text{eff}}$ changes the signal efficiency in the range from $+1.4\,\%$ to $-0.2\,\%$.

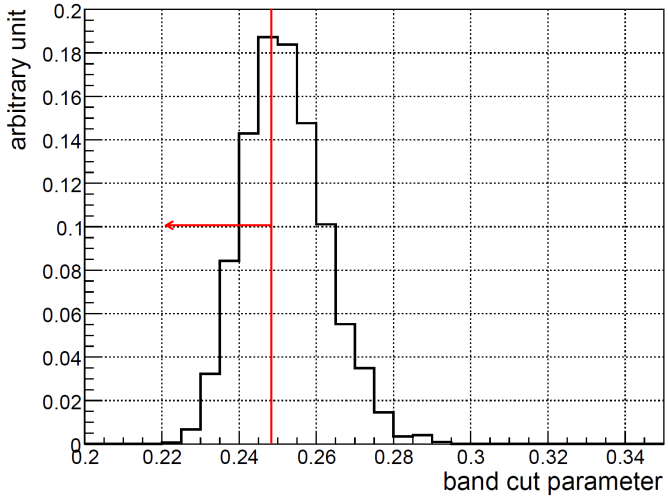

Figure 6.10: The band cut parameter distribution of 50 GeV signal MC after the timing cut in the signal region from 36 to 48 keV.

WIMP mass (GeV)	20	50	100	300	1000	3000	5000
signal efficiency (%)	23^{+7}_{-6}	29^{+4}_{-5}	26^{+2}_{-4}	19^{+1}_{-3}	16^{+1}_{-3}	15^{+1}_{-3}	15^{+1}_{-3}

Table 6.1: Signal efficiencies with their systematic errors for deriving the limit shown in Figure 7.6.

6.5.7 Decay constant for nuclear recoil

For the decay constants of scintillation light emission caused by nuclear recoils we took the uncertainty in the determination of the constants and the difference between our values and the NEST model [72], ± 1 ns, as our systematic uncertainty.

6.5.8 Total systematic error

The total systematic error on the signal efficiency for a 50 GeV WIMP was evaluated to $^{+13}_{-16}$ %, summing up the systematic errors as evaluated above in quadrature . This evaluation was repeated for WIMP masses of 20, 100 and 300 GeV and 1, 3 and 5 TeV and assumed to be applicable for masses close to the evaluated ones.

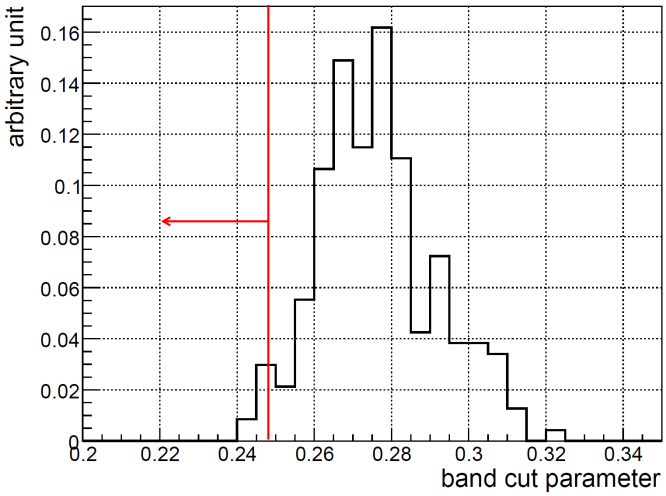

Figure 6.11: The band cut parameter distribution of the observed data after the timing cut in the signal region from 36 to 48 keV.

WIMP mass (GeV)	20	50	100	300	1000	3000	5000
Energy scale	$^{+30}_{-22}$	$^{+11}_{-13}$	$^{+0}_{-5.1}$	$^{+0.4}_{-7.1}$	$^{+1.1}_{-9.5}$	$^{+2.2}_{-11}$	$^{+2.7}_{-11}$
Energy resolution	$^{+0}_{-8.2}$	$^{+0}_{-5.6}$	$^{+0}_{-6.8}$	$^{+0}_{-8.1}$	$^{+0}_{-9.7}$	$^{+0}_{-8.8}$	$^{+0}_{-9.0}$
Radius cut	$^{+0}_{-3.3}$	$^{+0}_{-3.2}$	$^{+0}_{-4.0}$	$^{+0}_{-5.2}$	$^{+0}_{-6.8}$	$^{+0}_{-6.3}$	$^{+0}_{-6.4}$
Timing cut	$^{+4.2}_{-5.1}$	$^{+4.2}_{-5.1}$	$^{+4.2}_{-5.1}$	$^{+4.2}_{-5.1}$	$^{+4.2}_{-5.1}$	$^{+4.2}_{-5.1}$	$^{+4.2}_{-5.1}$
Band cut	± 4.2	± 4.2	± 4.2	± 4.2	± 4.2	± 4.2	± 4.2
$\mathcal{L}_{\text{eff}}$	$^{+6.4}_{-0}$	$^{+1.4}_{-0.2}$	$^{+0}_{-1.4}$	$^{+3.9}_{-0}$	$^{+1.0}_{-1.3}$	$^{+0}_{-1.7}$	$^{+0}_{-4.0}$
τ_{nr}	$^{+0}_{-0.8}$	$^{+1.3}_{-2.2}$	$^{+0}_{-8.8}$	$^{+0}_{-4.6}$	$^{+0}_{-4.7}$	$^{+0}_{-5.7}$	$^{+0}_{-5.7}$
total systematic error	$^{+31}_{-25}$	$^{+13}_{-16}$	$^{+5.9}_{-15}$	$^{+7.1}_{-14}$	$^{+6.0}_{-17}$	$^{+6.3}_{-18}$	$^{+6.5}_{-18}$

Table 6.2: Systematic errors on the signal efficiency for different WIMP masses. All the numbers tabulated are in % relative to the nominal efficiencies. They were evaluated by comparing ^{241}Am data and simulated events (see text).

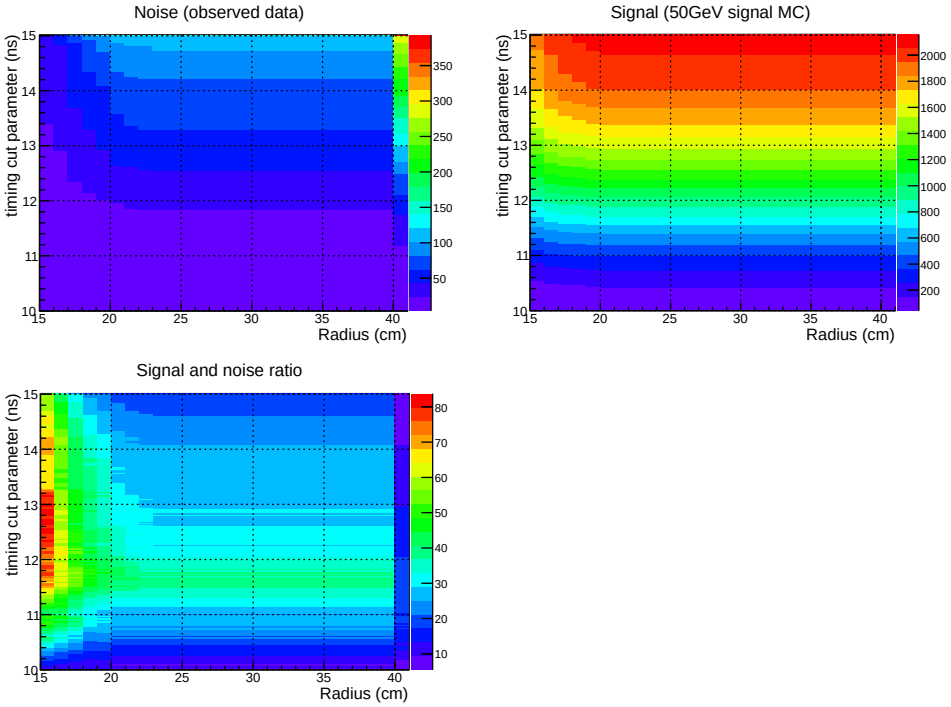

Figure 6.12: The 2-dimensional plots of radius and timing cut parameter when band cut parameter is 0.248. Left upper side figure shows remaining events of the observed data in two side bands ranging from 10 to 30 and from 80 to 100 keV. Right side figure shows remaining events of the 50 GeV signal MC in signal range from 30 to 80 keV. Left lower side figure shows the S/N ratio using 50 GeV signal MC and observed data.

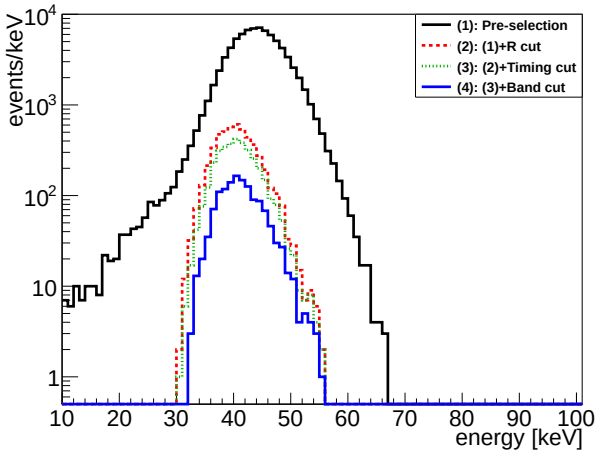

Figure 6.13: The 50 GeV WIMPs energy spectra of the simulated events after each step of the cuts. From top to bottom, simulated energy spectrum after the pre-selection (solid line), cut (2) (dashed line), cut (3) (dotted line), and cut (4) (solid line).

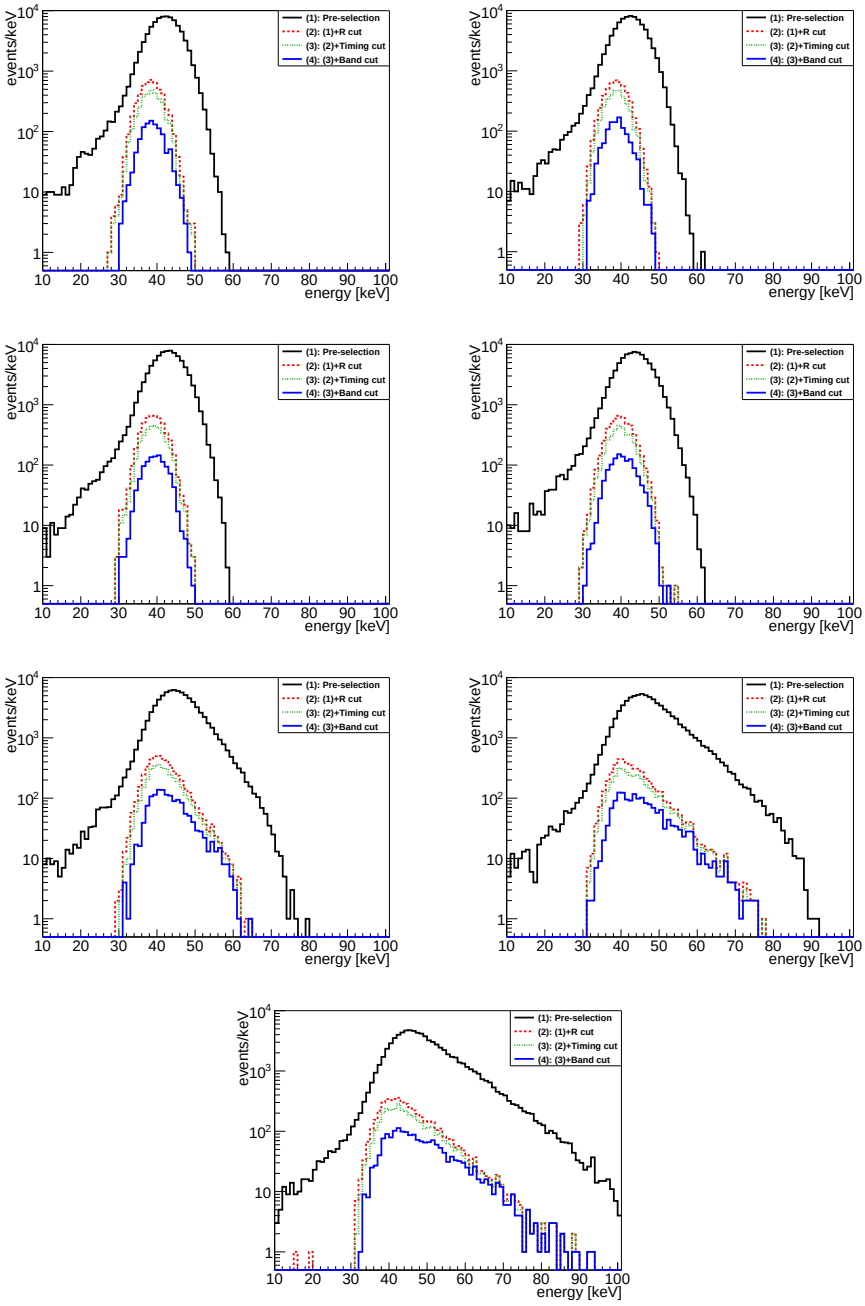

Figure 6.14: The WIMPs energy spectrum of 20, 23, 30, 40, 70, 100, and 130 GeV for the simulated events after each step of the cuts. From top to bottom, simulated energy spectrum after the pre-selection (solid line), cut (2) (dashed line), cut (3) (dotted line), and cut (4) (solid line).

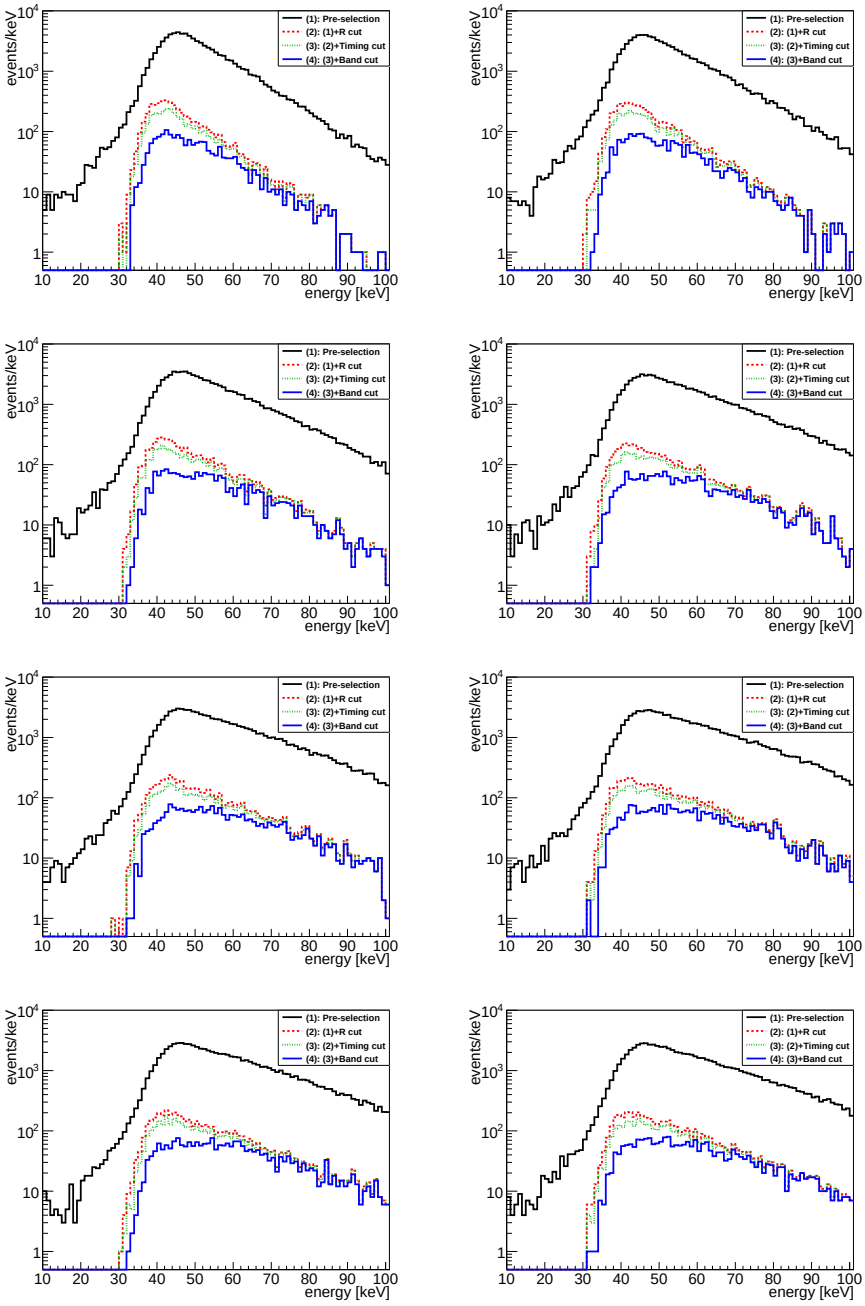

Figure 6.15: The WIMPs energy spectrum of 160, 200, 300, 600, 1000, 2000, 3000, and 5000 GeV for the simulated events after each step of the cuts. From top to bottom, simulated energy spectrum after the pre-selection (solid line), cut (2) (dashed line), cut (3) (dotted line), and cut (4) (solid line).

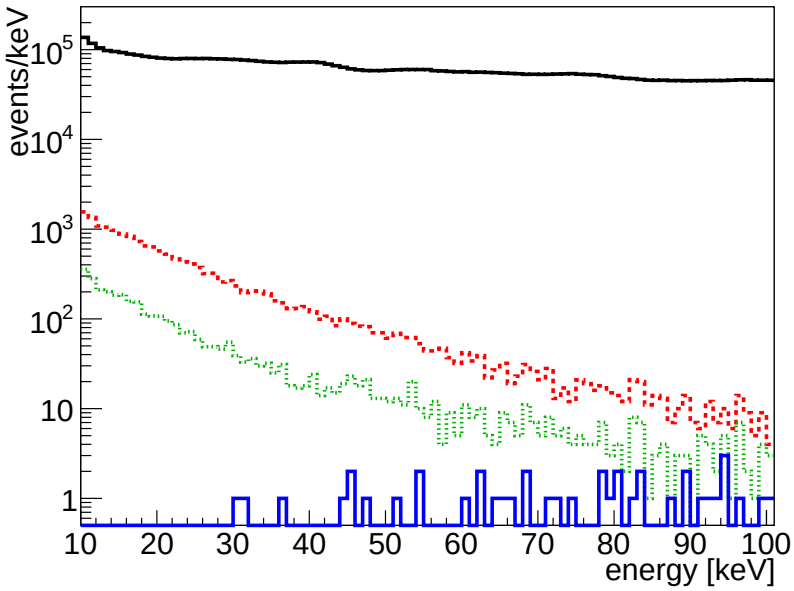

Figure 6.16: Energy spectra of the observed events after each step of the cuts for our 165.9 days data. From top to bottom, the observed energy spectrum after the pre-selection (solid line), cut (2) (dashed line), cut (3) (dotted line), and cut (4) (solid line).

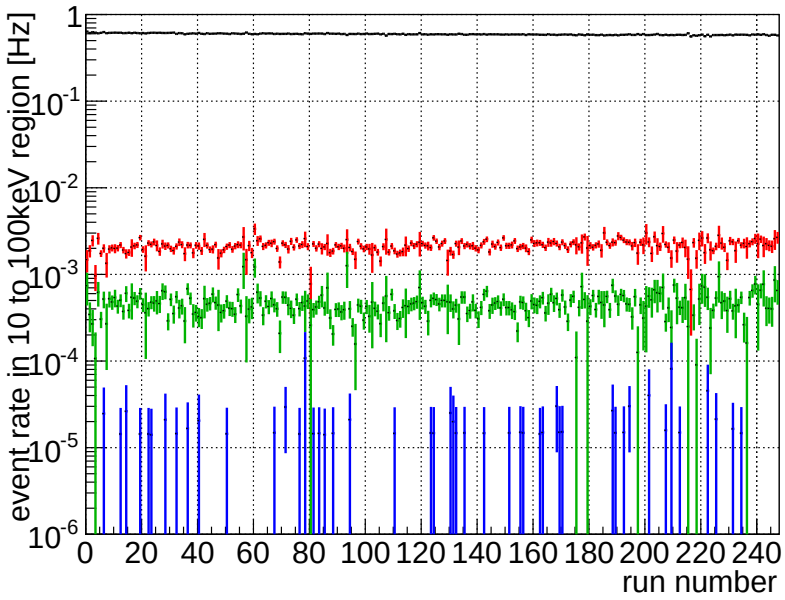

Figure 6.17: Event rates from 10 to 100 keV region after each step of the cuts. From top to bottom, event rates after the pre-selection (black line), radius cut (red line), timing cut (green line), and band cut (blue line).

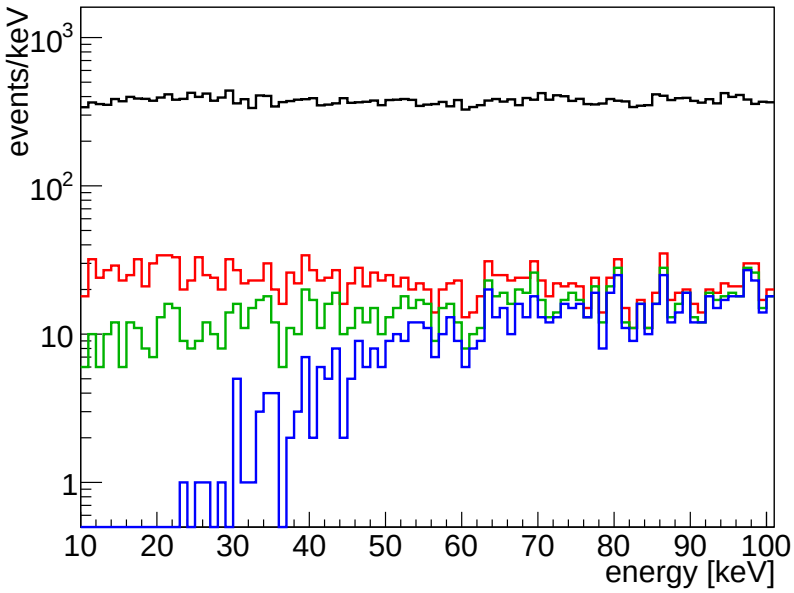

Figure 6.18: The background simulation from the ^{222}Rn daughter ^{214}Pb in 10 to 100 keV region. From top to bottom, these spectrum after the pre-selection (black line), radius cut (red line), timing cut (green line), band cut (blue line).

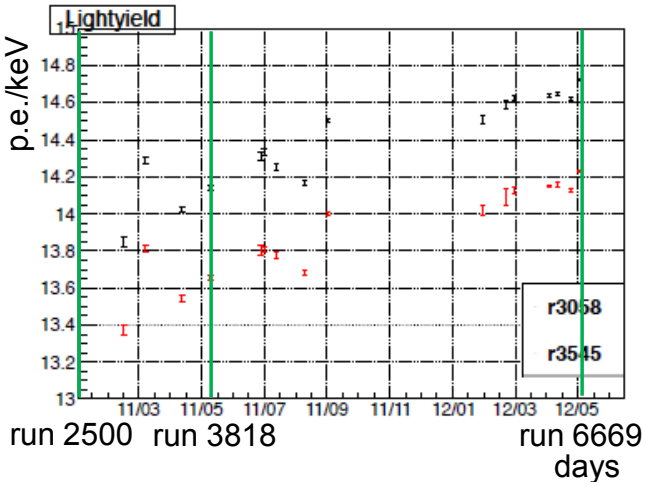

Figure 6.19: A stability of light yield. Difference of $^{+3.0}_{-3.1}$ % exists based on run3818 (^{57}Co energy scale correction data).

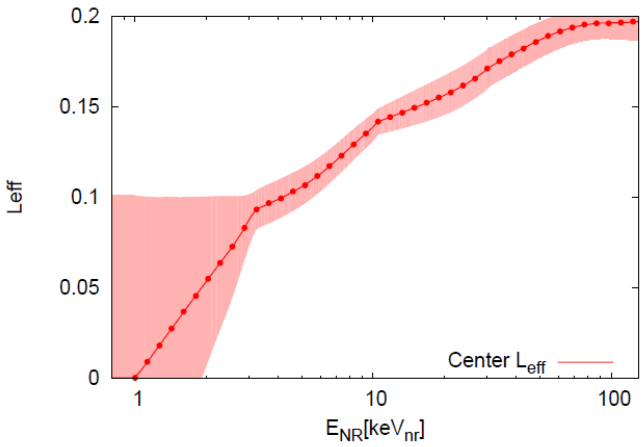

Figure 6.20: $\mathcal{L}_{\text{eff}}$ uncertainty: The pink band is $1\,\sigma$ uncertainty.

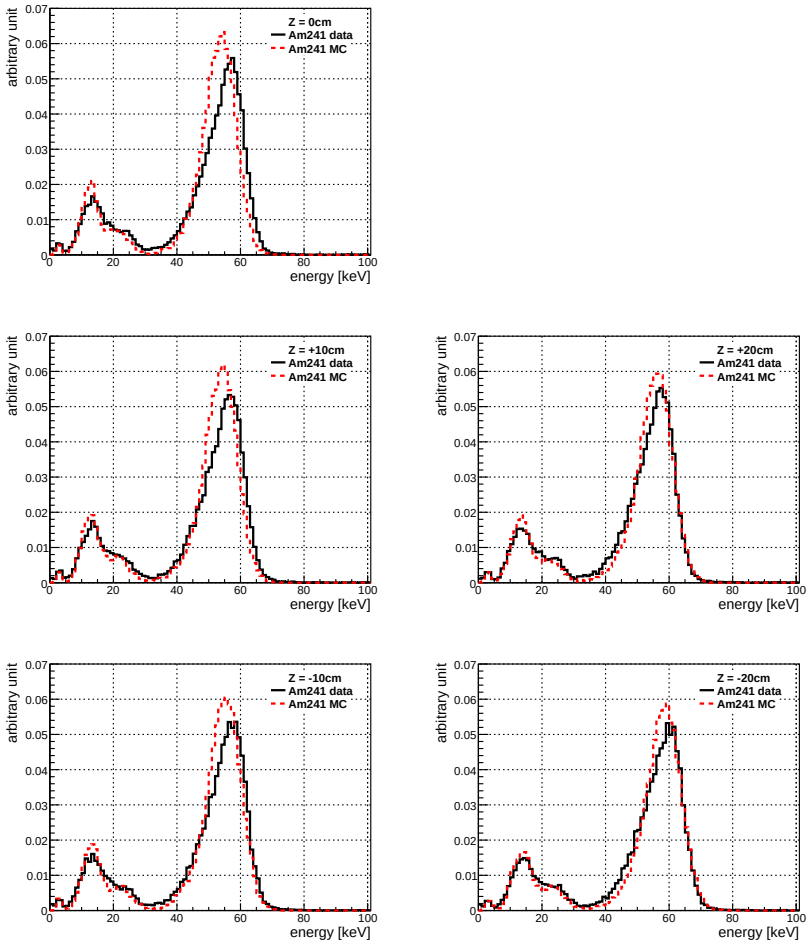

Figure 6.21: The comparison of energy distributions between data (solid histograms) and simulation (dashed histograms) of ^{241}Am at five vertical positions Z.

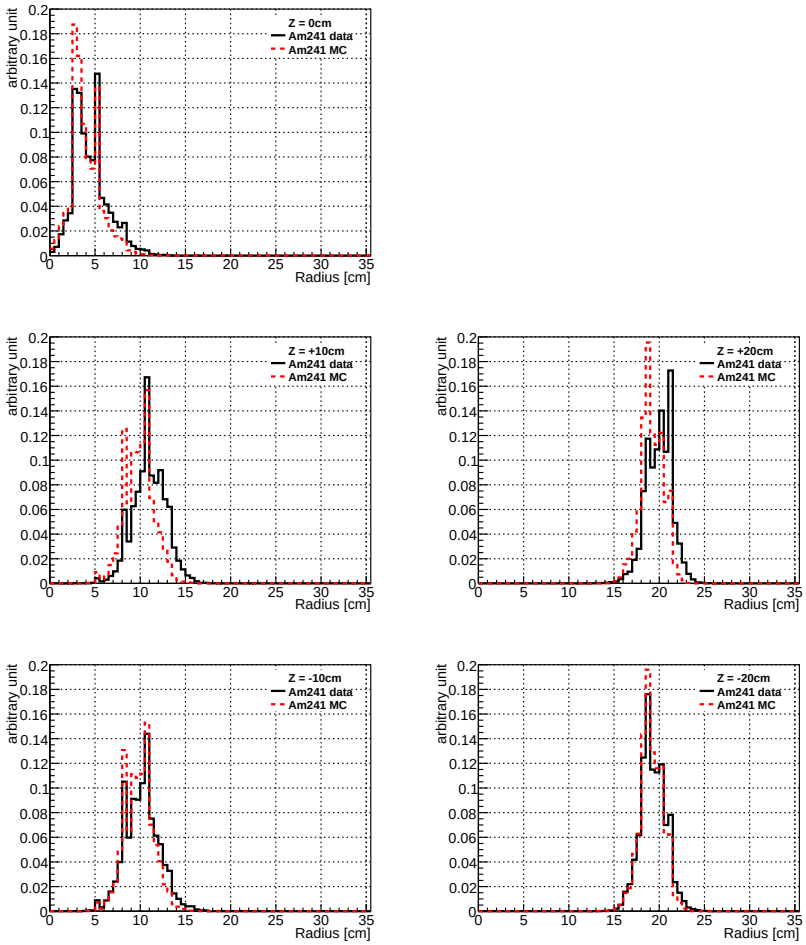

Figure 6.22: The comparison of reconstructed radius cut parameter distributions between ^{241}Am data (solid histograms) and simulation (dashed histograms) at five vertical positions in the detector, $Z = 0$ cm, +10 cm, +20 cm, -10 cm, and -20 cm from the top to the bottom, respectively.

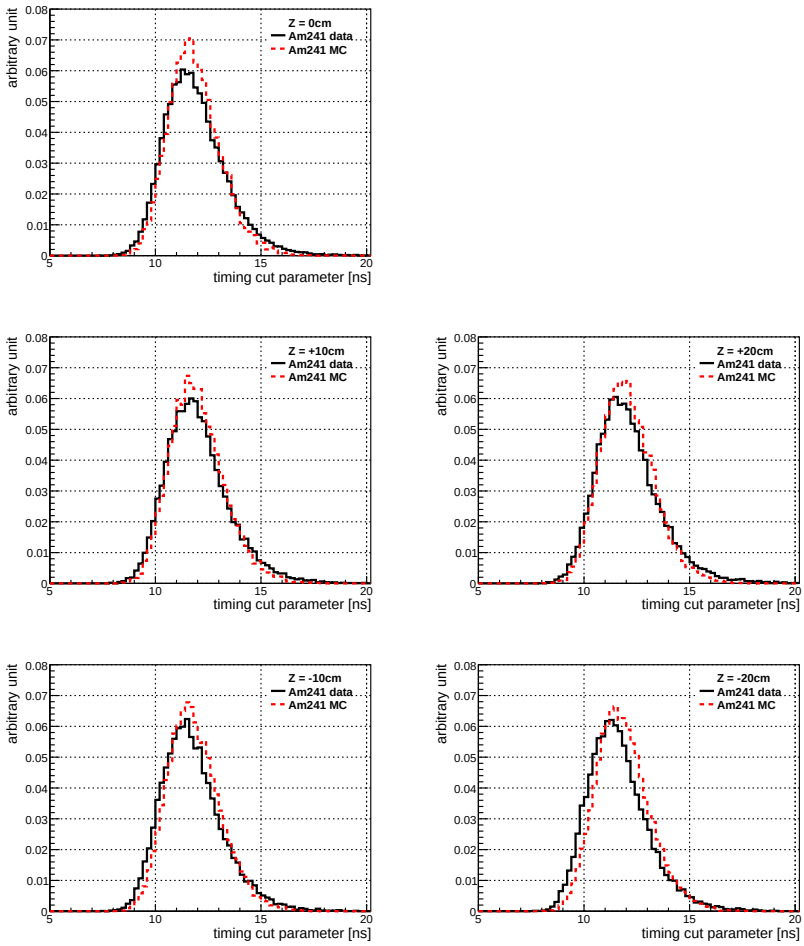

Figure 6.23: The comparison of timing cut parameter distributions between ^{241}Am data (solid histograms) and simulation (dashed histograms) at five vertical positions in the detector, Z = 0 cm, +10 cm, +20 cm, -10 cm, and -20 cm from the top to the bottom, respectively.

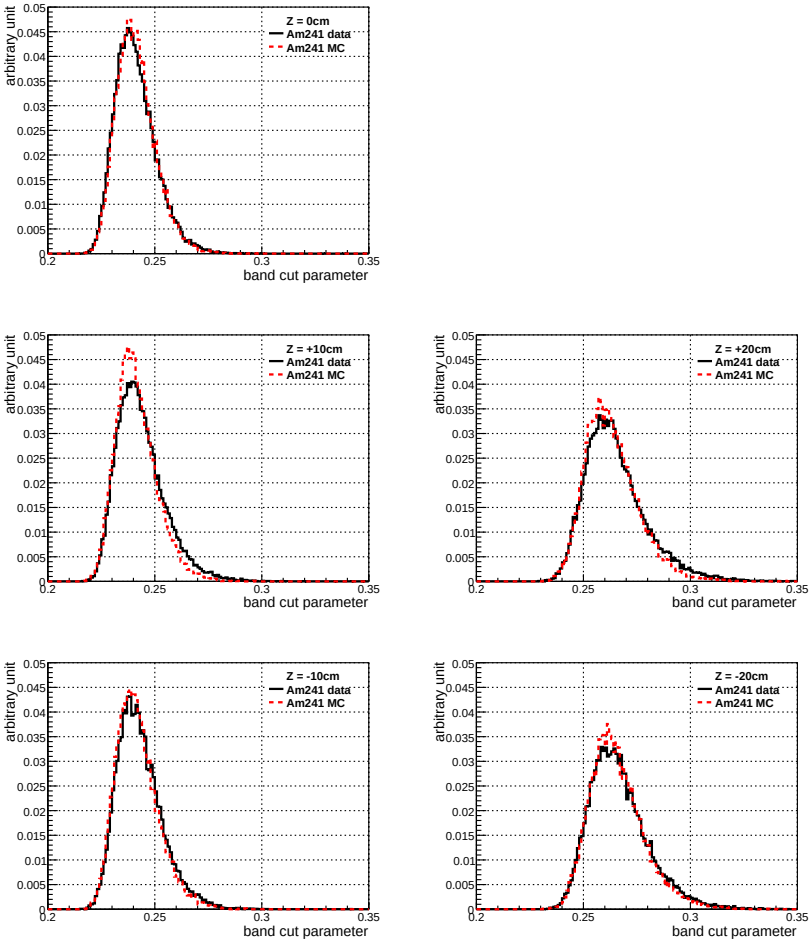

Figure 6.24: The comparison ob band cut parameter distributions between ^{241}Am data (solid histograms) and simulation (dashed histograms) for the band cut parameter at five vertical positions in the detector, $Z = 0\,\mathrm{cm}$, $+10\,\mathrm{cm}$, $+20\,\mathrm{cm}$, $-10\,\mathrm{cm}$, and $-20\,\mathrm{cm}$ from the top to the bottom, respectively.

Chapter 7

Result and Discussion

Since we could not find any significant signals, the upper limit for σ_I^{as} can be derived. In this Chapter also discuss the variation of our limit within our systematic uncertainties. Assuming a true number of events μ in the energy window before the event reduction, we can calculate the expected number of observed events by multiplying the signal efficiency tabulated in Table 6.1. Based on the expected number of observed events, we can generate number of observed events following Poisson statistics. This procedure was repeated to accumulate a histogram of the observed number of events for a fixed μ by sampling the signal efficiency within its systematic error. The 90 % C.L. upper limit for μ is the one that results in 10 % probability to have five events or less. Figures 7.1, 7.2, 7.3, 7.4, and 7.5 show distributions of expected number of events with various mass of WIMPs for the corresponding upper limits of μ. Using Eq. 2.42, this μ was then translated to an inelastic WIMP nucleus cross section with the variation of our limit within our systematic uncertainties shown by the gray band in Figure 7.6. A calculation of σ_I^{as} was done by the formula shown as

$$\sigma_I^{as} = \frac{R_{I,\text{point-like}} M_\chi}{\rho_\chi \langle v \rangle f N_T}\,, \tag{7.1}$$

where σ_I^{as} is the asymptotic cross section for inelastic scattering, $R_{I,\text{point-like}}$ is the total event rate in the signal region for calculating the 90 % C.L. upper limit both "with" and "without" systematic error when 5 events observed, ρ_χ is the local mass density of dark matter ($0.3\,\text{GeV}\,\text{c}^{-2}\,\text{cm}^{-3}$), a natural abundance of ^{129}Xe in natural Xe was assumed 0.264, N_T is $6.02\times10^{26}/129$ as the number of target nuclei taken into account natural abundance of ^{129}Xe, M_χ is the WIMP mass, f is the space phase factor, $\langle v \rangle$ is average WIMP velocity of $220\,\text{km}\,\text{s}^{-1}$. For example of 50 GeV WIMP, we used the the space phase factor of 0.13, the signal efficiency of 29 % and $R_{I,\text{point-like}}$ of $1.71\times10^{-3}\,\text{day}^{-1}\,\text{kg}^{-1}$

using 9.27 events, 132 days, and 41 kg of the natural Xe for 90 % C.L. without systematic error and $1.84\times10^{-3}\,\mathrm{day}^{-1}\,\mathrm{kg}^{-1}$ using 9.98 events, 132 days, and 41 kg of the natural Xe for 90 % C.L. with systematic error. We obtained for a 50 GeV WIMP an upper limit for its inelastic cross section on ^{129}Xe nuclei of 3.2 pb at the 90 % C.L without systematic error.

It should be noted that the constraint obtained by the DAMA group [56, 57] was derived from a statistical evaluation of an excess above a large background, $\sim 2\times10^{-2}\,\mathrm{keV}^{-1}\,\mathrm{day}^{-1}\,\mathrm{kg}^{-1}$. We achieved a lower background $\sim 3\times10^{-4}\,\mathrm{keV}^{-1}\,\mathrm{day}^{-1}\,\mathrm{kg}^{-1}$ using cuts discussed above. This low background allowed us to avoid having to subtract background to obtain a competitive limit. And DAMA group's upper limit did not consider any systematic errors. So our upper limit without systematic (solid line) in Figure 7.6 can be compared directly with the DAMA group. As a result of comparison between our result and the DAMA group, the upper limit of this work had a better constraint above 80 GeV WIMP mass compared with the DAMA group using the enriched Xe. Also, when comparing the inelastic channel and elastic, it can be expected total event rate of inelastic channel is 10 times lower than elastic for ^{129}Xe [73]. However, the inelastic channel would be expected a better sensitivity than that of elastic because of peak search at high energy region ($\sim$ 40 keV) resulting high background rejection.

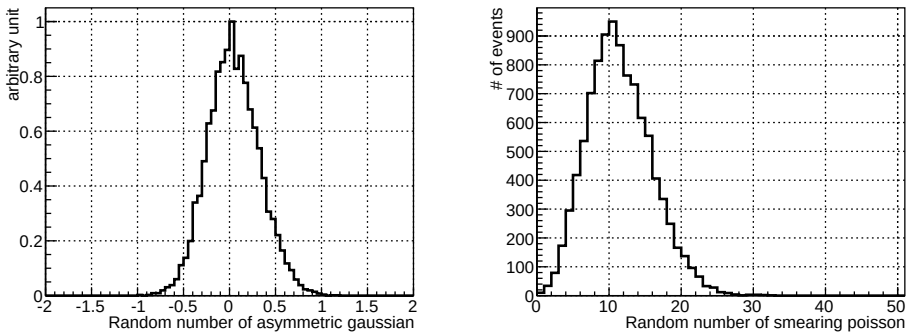

Figure 7.1: The left histogram is the asymmetric gaussian distribution with total systematic error of 20 GeV signal MC. The right histogram is the Poisson distribution smeared by the asymmetric gaussian to obtain the 90 % upper limit with systematic error.

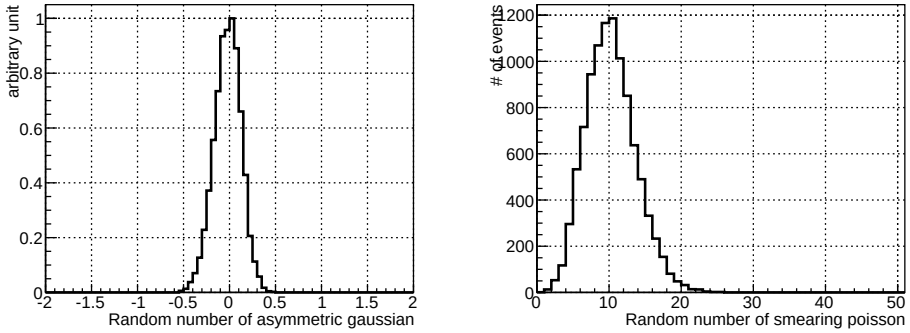

Figure 7.2: The left histogram is the asymmetric gaussian distribution with total systematic error of 50 GeV signal MC. The right histogram is the Poisson distribution smeared by the asymmetric gaussian to obtain the 90 % upper limit with systematic error.

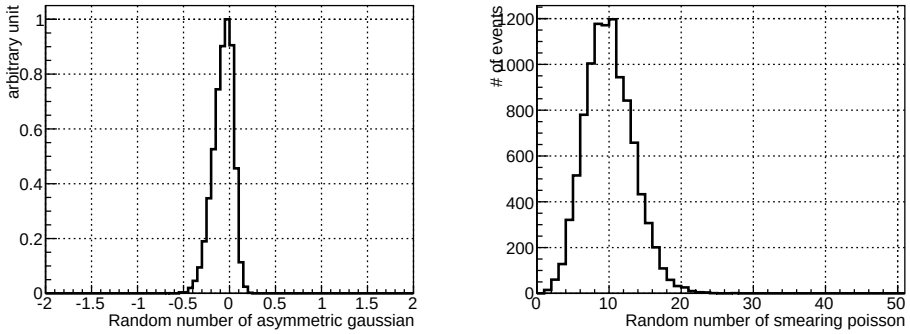

Figure 7.3: The left histogram is the asymmetric gaussian distribution with total systematic error of 100 GeV signal MC. The right histogram is the Poisson distribution smeared by the asymmetric gaussian to obtain the 90 % upper limit with systematic error.

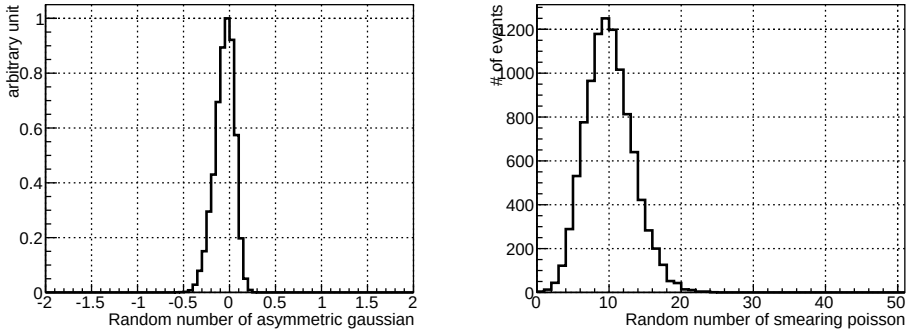

Figure 7.4: The left histogram is the asymmetric gaussian distribution with total systematic error of 300 GeV signal MC. The right histogram is the Poisson distribution smeared by the asymmetric gaussian to obtain the 90 % upper limit with systematic error.

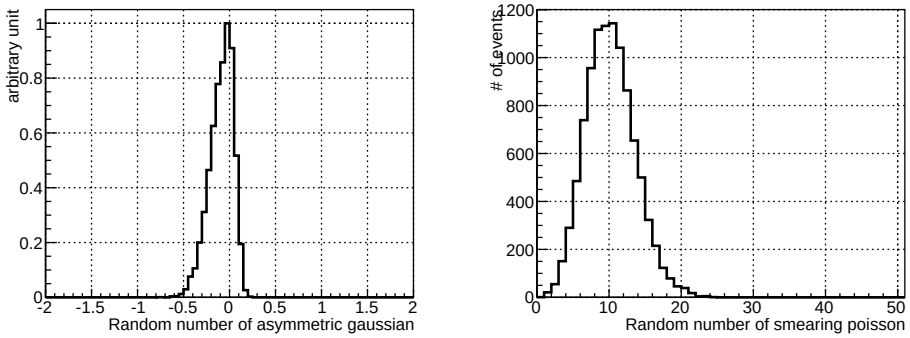

Figure 7.5: The left histogram is the asymmetric gaussian distribution with total systematic error of 5000 GeV signal MC. The right histogram is the Poisson distribution smeared by the asymmetric gaussian to obtain the 90 % upper limit with systematic error.

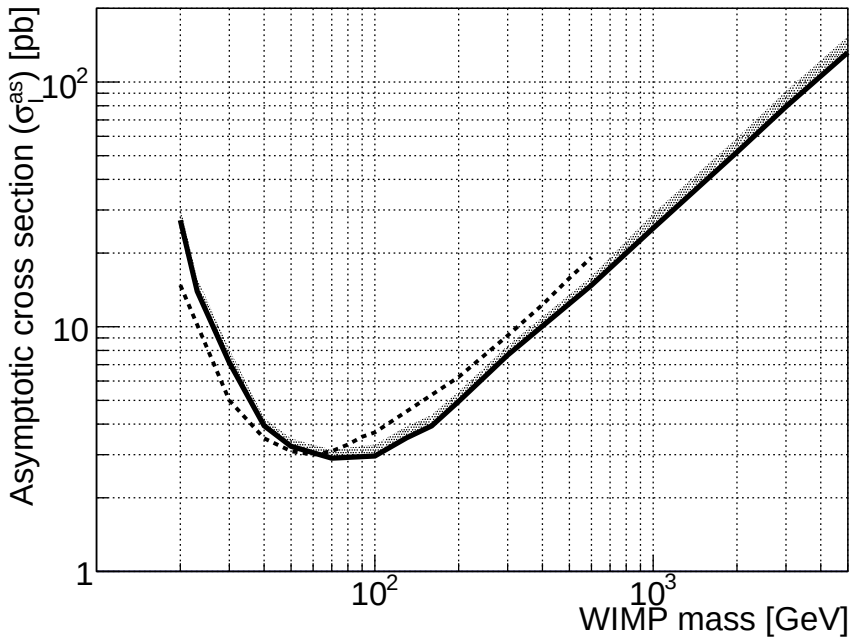

Figure 7.6: The black solid line is the 90 % C.L. upper limit on the asymptotic cross section σ_I^{as} for inelastic scattering on ^{129}Xe (black solid line). The gray band covers its variation with the systematic uncertainty. The dotted line is the limit obtained by the DAMA group[56, 57] derived from a statistical evaluation of an excess above its background.

Chapter 8

Conclusion

A search for inelastic scattering of WIMPs on ^{129}Xe was performed using data from the single phase liquid xenon detector XMASS. The observed data used for this search was taken between December 24, 2010 and May 10, 2012, and amounts to a total live time of 165.9 days. The inelastic signal simulation was produced with XMASS detector simulation. The signal simulation was a sum of 39.58 keV gamma ray by de-excitation of ^{129}Xe and a few keV by nuclear recoil. Data reductions of four methods are the pre-selection, the radius cut, the timing cut, and the band cut were applied. Cut optimization with the radius, the timing, and the band was done by using the ratio of remaining signal events in the signal range from 30 to 80 keV from the simulation over the sum of background events in two side bands ranging from 10 to 30 and from 80 to 100 keV. For the radius cut this procedure results in an extremely low fiducial volume, leading us to relax the cut to 15 cm. Optimized cut parameters obtained 15 cm for the radius cut, 12.91 ns for the timing cut, and a ratio of 0.248 for the band cut. By data reduction using optimized cut parameters, remaining events in the signal region; 36 - 48 keV of observed data were 5 events. A probability more than obtained 5 events was 5.3 % assuming the Poisson when main radon concentration was 2.0±0.6 events in the signal region in the detector which was deduced from the ^{222}Rn concentration in LXe as the main source of background. As other background contributions were smaller but less certain, we did not subtract the background when calculating the limits. The central volume within 15 cm of the XMASS detector containing 41 kg of LXe was used in this analysis. We observed no significant excess in 165.9 days' data and derived an upper limit of inelastic cross section on ^{129}Xe nuclei of 3.2 pb for a 50 GeV WIMP at the 90 % confidence level. As the result of comparison between our result and the DAMA group, the upper limit of the our result had better constraint above 80 GeV WIMP mass compared with the DAMA group. Also, XMASS obtained very low

background ($\sim 3{\times}10^{-4}\,\mathrm{keV}^{-1}\,\mathrm{day}^{-1}\,\mathrm{kg}^{-1}$) by good efficiency reduction. This level is 2 order lower than DAMA group.

Appendix A

Signal spectrum based on other form factor A from Ref. [73]

A expected spectrum of inelastic channel have published. Therefore we can obtain the WIMP - neutron SD cross section with inelastic scattering search. In the appendix A, we show the upper limit using this recent spectrum.

A.1 Signal simulation

Signal simulation was produced using recent structure factor from Ref. [73]. Figure A.1 was based on the inelastic structure factors for $S_n(u)$ 1b+2b currents.

A.2 Reduction and optimization

We use the same method reduction and optimized cut parameters as Chapter. 5. The pre-selection, the radius, the timing and the band cut were used. A signal MC of 50 GeV WIMP mass shows in Figure A.5 after each cuts. Signal MCs of other mass show in Figures A.6 and A.7 after each cuts. Figures A.2, A.3 and A.4 show cut parameter distributions in the signal region. Signal efficiencies show in Table A.1.

A.3 Systematic error evaluation

The systematic uncertainty on our signal efficiency was estimated from data - MC comparisons for ^{241}Am calibration data (60 keV) at various positions

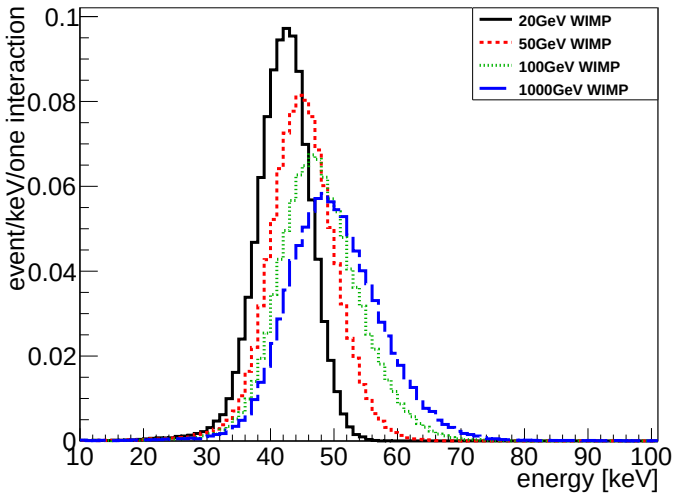

Figure A.1: Simulated energy spectra for the WIMP mass with 20 (solid line), 50 (dashed line), 100 (dotted line), and 1000 GeV (long dashed line). The energy is defined by dividing the number of photoelectrons observed by 13.9 p.e./keV.

within the fiducial volume. The relevant comparisons are shown in Figures 6.21, 6.22, 6.23, and 6.24. From these comparisons we derived systematic differences in the energy scale, the energy resolution, the radius reconstruction, the timing cut and the band cut parameter. There was uncertainty in the effective light yield $\mathcal{L}_{\text{eff}}$ and in the decay constants of nuclear recoils. The cumulative effect of these individual contributions was obtained by adding these errors in quadrature. As an example for our systematic error evaluation we explain it for the signal efficiency for 50 GeV WIMPs; see Table A.2 for other masses.

A.3.1 Total systematic error

The total systematic error on the signal efficiency for a 50 GeV WIMP was evaluated to $^{+8.2}_{-15}$ %, summing up the systematic errors as evaluated above in quadrature . This evaluation was repeated for WIMP masses of 20, 100 and 300 GeV and 1, 3 and 5 TeV and assumed to be applicable for masses close to the evaluated ones.

WIMP mass (GeV)	20	50	100	300	1000	3000	5000
signal efficiency (%)	24^{+7}_{-6}	30^{+2}_{-5}	29^{+2}_{-4}	26^{+2}_{-5}	25^{+2}_{-5}	25^{+2}_{-5}	25^{+2}_{-5}

Table A.1: Signal efficiencies with their systematic errors for deriving the limit shown in Figure B.7.

WIMP mass (GeV)	20	50	100	300	1000	3000	5000
Energy scale	$^{+27}_{-21}$	$^{+5.6}_{-9.9}$	$^{+0}_{-7.8}$	$^{+4.8}_{-13}$	$^{+5.5}_{-14}$	$^{+5.9}_{-14}$	$^{+6.1}_{-17}$
Energy resolution	$^{+0}_{-7.1}$	$^{+0}_{-5.7}$	$^{+0}_{-7.9}$	$^{+0}_{-8.9}$	$^{+0}_{-9.7}$	$^{+0}_{-9.5}$	$^{+0}_{-9.5}$
Radius cut	$^{+0}_{-3.7}$	$^{+0}_{-4.1}$	$^{+0}_{-4.4}$	$^{+0}_{-4.3}$	$^{+0}_{-5.3}$	$^{+0}_{-4.5}$	$^{+0}_{-3.9}$
Timing cut	$^{+4.2}_{-5.1}$	$^{+4.2}_{-5.1}$	$^{+4.2}_{-5.1}$	$^{+4.2}_{-5.1}$	$^{+4.2}_{-5.1}$	$^{+4.2}_{-5.1}$	$^{+4.2}_{-5.1}$
Band cut	± 4.2	± 4.2	± 4.2	± 4.2	± 4.2	± 4.2	± 4.2
$\mathcal{L}_{\text{eff}}$	$^{+0}_{-2.0}$	$^{+0}_{-1.5}$	$^{+1.8}_{-0}$	$^{+5.7}_{-0}$	$^{+1.0}_{-0}$	$^{+2.2}_{-2.9}$	$^{+5.1}_{-0}$
τ_{nr}	$^{+0}_{-0.8}$	$^{+0}_{-4.7}$	$^{+0}_{-5.4}$	$^{+0}_{-4.7}$	$^{+0.2}_{-4.1}$	$^{+0}_{-7.1}$	$^{+0}_{-4.9}$
total systematic error	$^{+28}_{-24}$	$^{+8.2}_{-15}$	$^{+6.2}_{-15}$	$^{+9.5}_{-18}$	$^{+8.2}_{-19}$	$^{+8.7}_{-20}$	$^{+9.9}_{-21}$

Table A.2: Systematic errors on the signal efficiency for different WIMP masses. All the numbers tabulated are in % relative to the nominal efficiencies. They were evaluated by comparing ^{241}Am data and simulated events (see text).

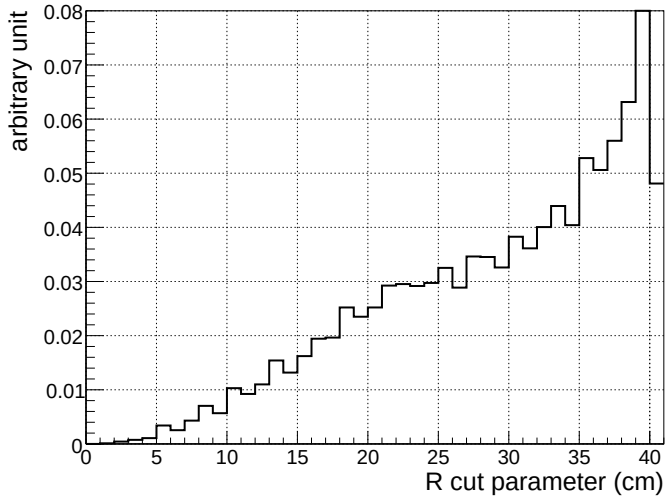

Figure A.2: The radius cut parameter distribution of 50 GeV signal MC after pre-selection in the signal region from 36 to 48 keV.

A.4 WIMP - neutron SD cross section

We calculated the 90 % C.L. upper limit on WIMP - neutron SD cross section remaining five events in the signal region from Ref. [73]. As the result, we obtained $1.1\times10^{-37}\,\mathrm{cm}^2$ on its cross section. This exclusion plot was shown in Figure B.7 with a result of Appendix B.

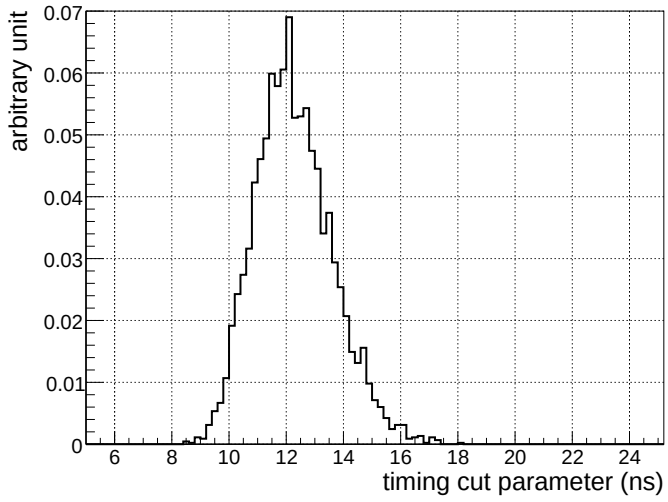

Figure A.3: The timing cut parameter distribution of 50 GeV signal MC after the radius cut in the signal region from 36 to 48 keV.

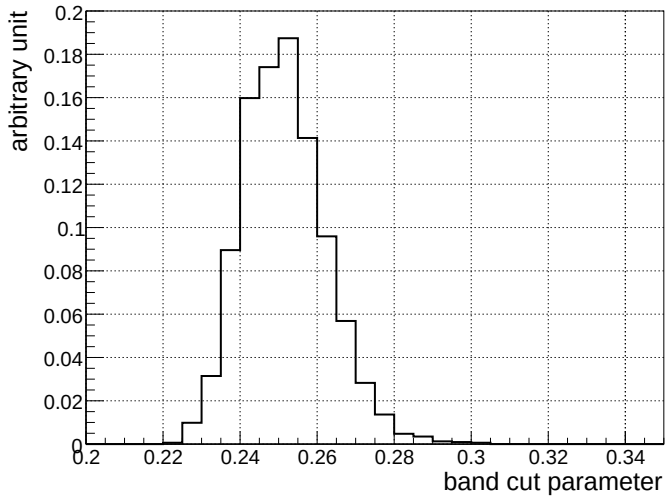

Figure A.4: The band cut parameter distribution of 50 GeV signal MC after the timing cut in the signal region from 36 to 48 keV.

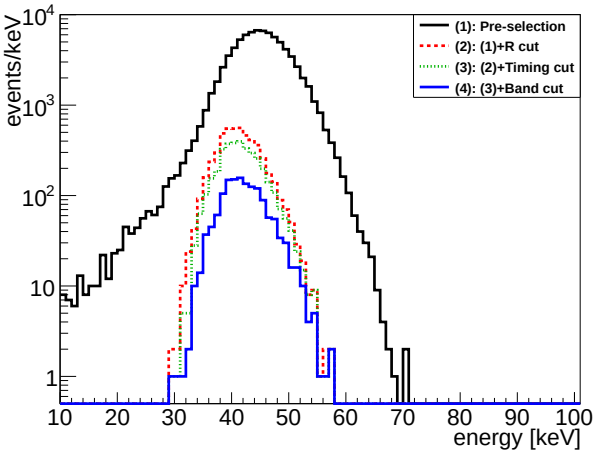

Figure A.5: The 50 GeV WIMPs energy spectra of the simulated events after each step of the cuts. From top to bottom, simulated energy spectrum after the pre-selection (solid line), radius cut (dashed line), timing cut (dotted line), and band cut (solid line).

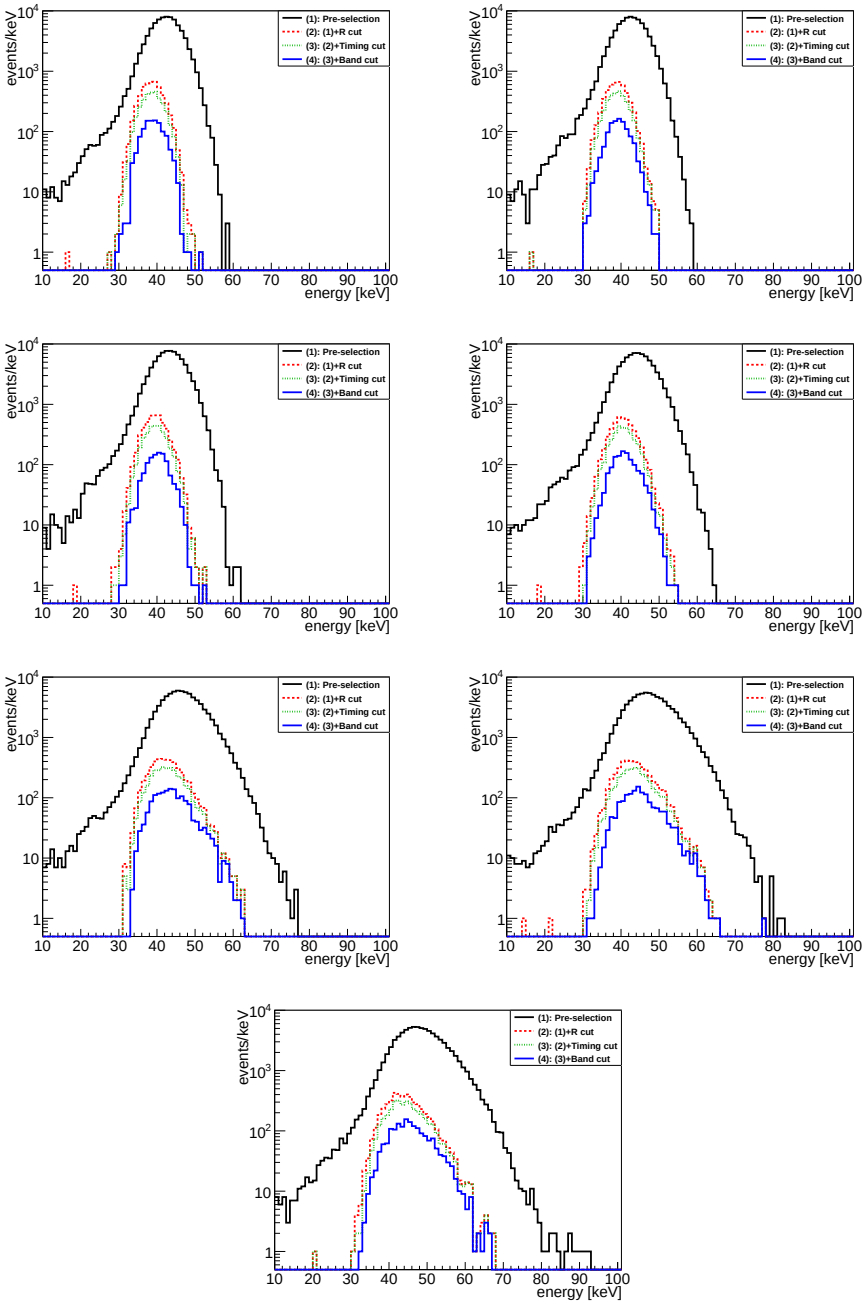

Figure A.6: The WIMPs energy spectrum of 20, 23, 30, 40, 70, 100, and 130 GeV for the simulated events after each step of the cuts. From top to bottom, simulated energy spectrum after the pre-selection (solid line), radius cut (dashed line), timing cut (dotted line), and band cut (solid line).

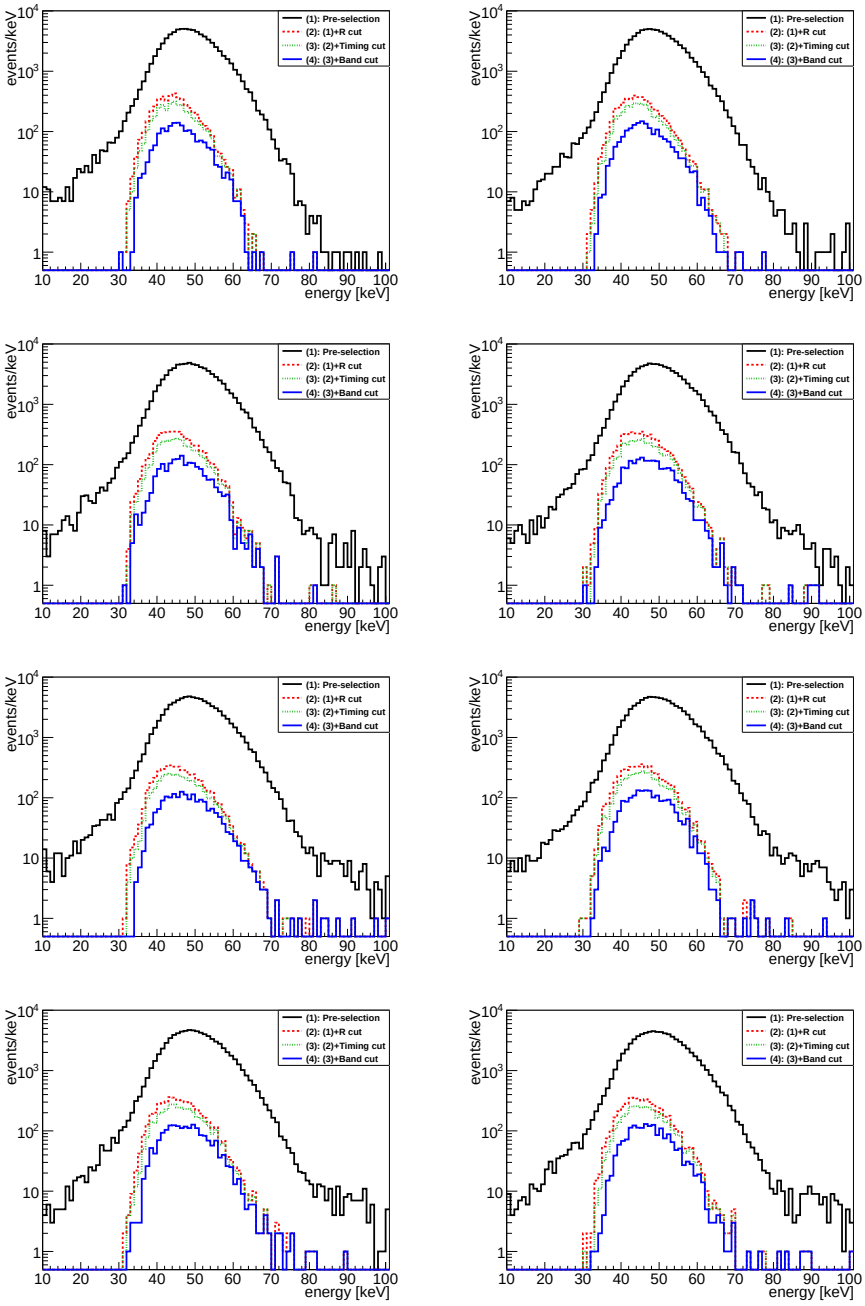

Figure A.7: The WIMPs energy spectrum of 160, 200, 300, 600, 1000, 2000, 3000, and 5000 GeV for the simulated events after each step of the cuts. From top to bottom, simulated energy spectrum after the pre-selection (solid line), radius cut (dashed line), timing cut (dotted line), and band cut (solid line).

Appendix B

Signal spectrum based on other form factor B from Ref. [74]

A expected spectrum of inelastic channel have published. Therefore we can obtain the WIMP - neutron SD cross section with inelastic scattering search. In the appendix B, we show the upper limit using this recent spectrum.

B.1 Signal simulation

Signal simulation was produced using recent structure factor from Ref. [74]. Figure B.1 was made from the differential scattering rate for inelastic scattering of Ref. [74]

B.2 Reduction and optimization

We use the same method reduction and optimized cut parameters as Chapter. 5. The pre-selection, the radius, the timing and the band cut were used. A signal MC of 50 GeV WIMP mass shows in Figure B.5 after each cuts. Signal MCs of other mass show in Figures B.6 after each cuts. Figures B.2, B.3 and B.4 show cut parameter distributions in the signal region. Signal efficiencies show in Table B.1.

WIMP mass (GeV)	50	100	200	500	1000
signal efficiency (%)	33	30	25	22	20

Table B.1: Signal efficiencies for deriving the limit shown in Figure B.7.

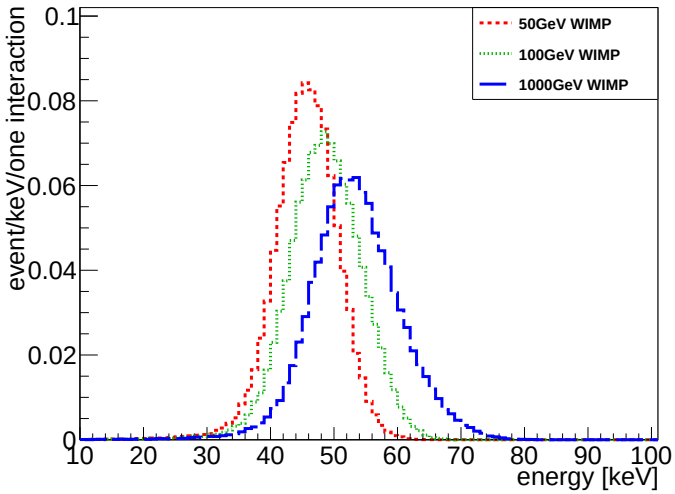

Figure B.1: Simulated energy spectra for the WIMP mass with 50 (dashed line), 100 (dotted line), and 1000 GeV (long dashed line). The energy is defined by dividing the number of photoelectrons observed by 13.9 p.e./keV.

B.3 WIMP - neutron SD cross section

We calculated the 90 % C.L. upper limit on WIMP - neutron SD cross section remaining five events in the signal region from Ref. [74]. As the result, we obtained 4.2×10^{-38} cm^2 on its cross section. This exclusion plot was shown in Figure B.7.

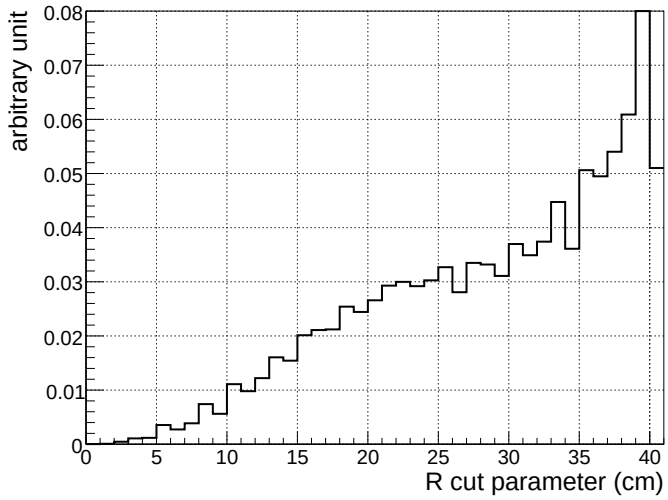

Figure B.2: The radius cut parameter distribution of 50 GeV signal MC after pre-selection in the signal region from 36 to 48 keV.

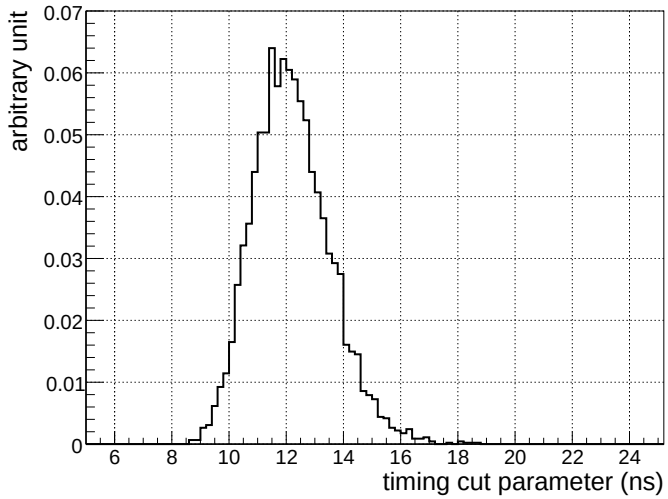

Figure B.3: The timing cut parameter distribution of 50 GeV signal MC after the radius cut in the signal region from 36 to 48 keV.

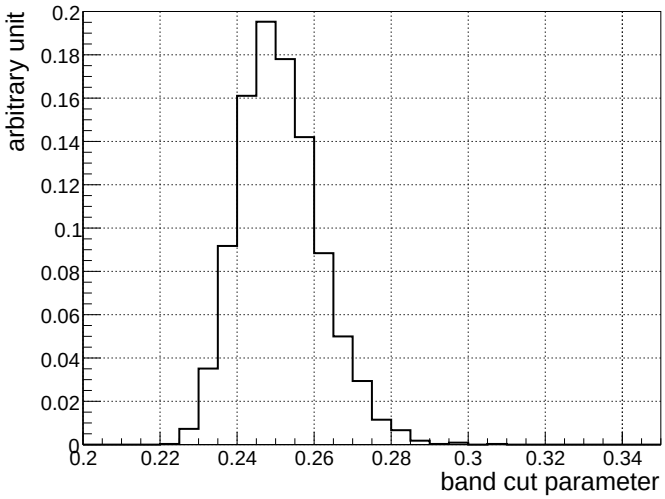

Figure B.4: The band cut parameter distribution of 50 GeV signal MC after the timing cut in the signal region from 36 to 48 keV.

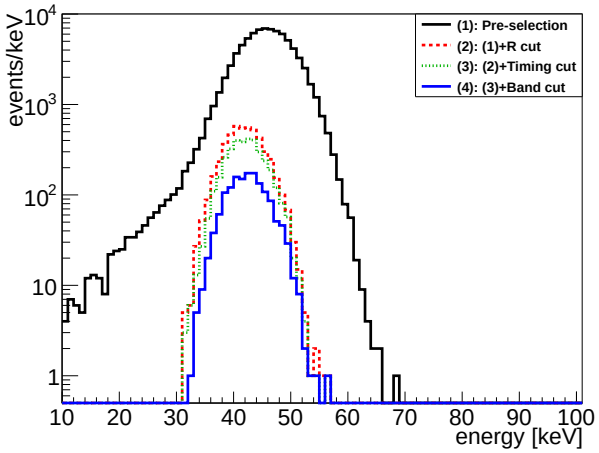

Figure B.5: The 50 GeV WIMPs energy spectra of the simulated events after each step of the cuts. From top to bottom, simulated energy spectrum after the pre-selection (solid line), radius cut (dashed line), timing cut (dotted line), and band cut (solid line).

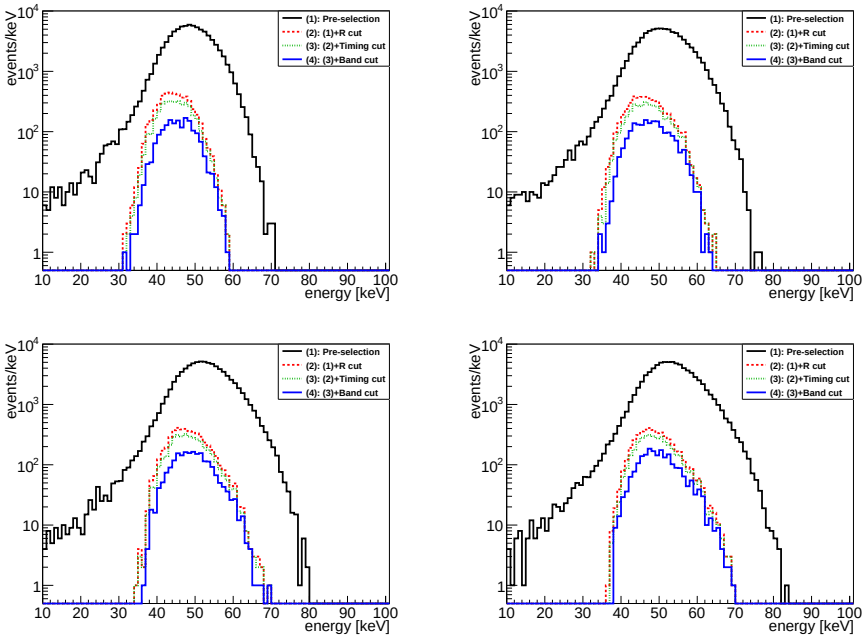

Figure B.6: The WIMPs energy spectrum of 100, 200, 500, and 1000 GeV for the simulated events after each step of the cuts. From top to bottom, simulated energy spectrum after the pre-selection (solid line), radius cut (dashed line), timing cut (dotted line), and band cut (solid line).

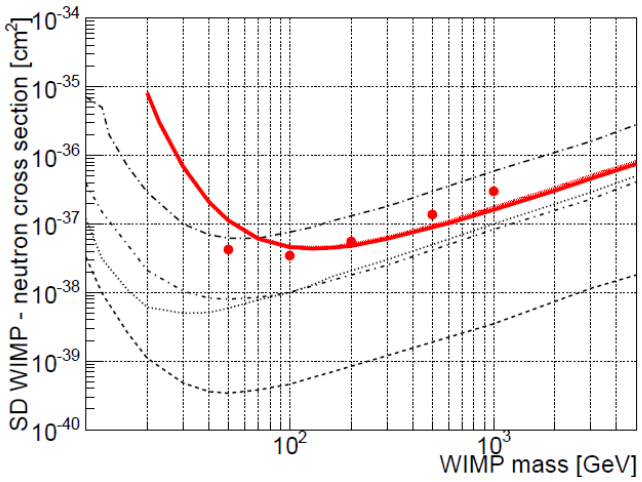

Figure B.7: The red solid line is the 90 % C.L. upper limit on the WIMP - neutron SD cross section and the pink band covers its variation with the systematic uncertainty as the appendix A.The red point is the 90 % C.L. upper limit on the WIMP - neutron SD cross section as the appendix B. The dotted lines are the 90 % C.L. upper limit obtained by elastic scattering of XENON10, CDMS, ZEPLIN-III, and XENON100, Refs. [75, 77, 76, 17].

Reference

[1] F. Zwicky. Helv. Phys. Acta **6**, 110 (1933).

[2] R. P. Olling, MNRAS **311**, 361(2000).

[3] K. G. Begeman, A. H. Broeils and R. H. Sanders, MNRAS **249**, 523 (1991).

[4] J. Caldwell and J. P. Ostrinker Astrophys. J. **251**, 61 (1981).

[5] P. Ade, *et al.*, (Planck Collaboration), arXiv:1303.5076.

[6] M.Tegmark *et al.*, Phys. Rev. D **74**, 123507 (2006).

[7] Astalos *et al.*, Phys. Rev. D **69**, 011101 (2004).

[8] P. Sikivie Phys. Rev. Lett. **51**, 1415 (1983).

[9] S. Andriamonje *et al.*, JCAP **04**, 010 (2007).

[10] Y.Inoue *et al.*, Phys. Lett. B **68**, 93 (2008).

[11] K. Abe *et al.*, (XMASS Collaboration), Phys. Lett. B **724**, 46 (2013).

[12] G. Jungman *et al.*, Phys. Rep. **267**, 195 (1996).

[13] R. Bernabei *et al.*, Eur. Phys. J. C **67**, 39 (2010).

[14] Z. Ahmed *et al.*, Phys. Rev. Lett. **106**, 131302 (2011).

[15] J. Angle, *et al.*, Phys. Rev. Lett. **100**, 021303 (2008).

[16] E. Aprile *et al.*, Phys. Rev. Lett. **109**, 181301 (2012).

[17] E. Aprile *et al.*, Phys. Rev. Lett. **111**, 021301 (2013).

[18] D. S. Akerib *et al.*, arXiv:1310.8214.

[19] T. Tanaka *et al.*, Astrophys. J. **742**, 78 (2011).

[20] M. G. Aartsen *et al.*, Phys. Rev. Lett. **110**, 131302 (2013).

[21] DMTOOLS http://dmtools.brown.edu:8080/session/new

[22] Table of isotope

[23] P. Belli *et al.*, Nuovo Cimento C **19**, 537 1996

[24] J. D. Lewin and P. F. Smith, Astropart. Phys. **6**, 87 (1996).

[25] F. Arneode *et al.*, Nucl. Instrum. Meth A **449**, 147 (2000).

[26] D. Akimov *et al.*, Nucl. Instrum. Meth A **524**, 245 (2000).

[27] N. J. Spooner *et al.*, Phys. Lett. B **321**, 156 (1994).

[28] Y. Messous *et al.*, Astropart. Phys. **3**, 361 (1995).

[29] K. Ueshima, 2010, *Study of pulse shape discrimination and low background techniques for liquid xenon dark matter detectors*, PhD dissertation, University of Tokyo, Japan.

[30] M. T. Ressell and D. J. Dean, Phys. Rev. C **56**, 535 (1997).

[31] Y. Suzuki, arXiv:hep-ph/0008296.

[32] National Institute of Standards and Technology, http://www.nist.gov/srd/nist12.html

[33] Photon Cross Sections Database, http://physics.nist.gov/PhysRefData/Xcom/Text/XCOM.html

[34] A. Baldini *et al.*, IEEE Trans. Dielectr. Electr. Insul. **13**, 547 (2006).

[35] Handbook of Chemistry & Physics, The Chemical Rubber Company.

[36] A. C. Sinnock and B. L. Smith Phys. Rev. **181**, 1297 (1969).

[37] S. Eidelman *et al.*, (Particle Data Group), Phy. Lett. B **592**, 1 (2004).

[38] S. Nakamura KEK workshop "Radiation detector and its application" , 2004

[39] T. Doke *et al.*, Jpn. J. Appl. Phys. **41**, 1538 (2002).

[40] T. Doke and K. Masuda Nucl. Instr. and Meth. A **420**, 62 (1999).

[41] MEG proposal to PSI, Proposal to INFN,
(URL: http://meg.web.psi.ch/docs/index.html).

[42] Photon Cross Sections Database,
(URL: http://physics.nist.gov/PhysRefData/Xcom/Text/XCOM.html).

[43] S. Fukuda *et al.*, (Super-Kamiokande Collaboration), Nucl. Instrum. Meth. A**501**, 418 (2003).

[44] Y. Takeuchi *et al.*, (Super-Kamiokande Collaboration), Phys. Lett. B **452**, 418 (2003).

[45] W, Otani, master thesis 1994, University of Tokyo, Japan.

[46] K. Miuchi, master thesis 1999, University of Tokyo, Japan.

[47] H. Nishiie, master thesis 2011, University of Tokyo, Japan.

[48] R. Bernabei *et al.*, Eur. Phys. J. C **56**, 333 (2008).

[49] C. E. Aalseth *et al.*, Phys. Rev. Lett. **106**, 131301 (2011).

[50] G. Angloher *et al.*, Eur. Phys. J. C **72**, 1971 (2012).

[51] J. Angle *et al.*, Phys. Rev. Lett. **107**, 051301 (2011).

[52] Z. Ahmed *et al.*, Science **327**, 1619 (2010).

[53] E. Armengaud *et al.*, Phys. Rev. D **86**, 051701(R) (2012).

[54] H. Ejiri, K. Fushimi, and H. Ohsumi, Phys. Lett. B **317**, 14 (1993).

[55] K. Fushimi *et al.*, Nucl. Phys. B (Proc. Suppl.) **35**, 400 (1994).

[56] P. Belli *et al.*, Phys. Lett. B **387**, 222 (1996).

[57] R. Bernabei *et al.*, New J. Phys. **2**, 15 (2000).

[58] Y. Suzuki, arXiv:hep-ph/0008296.

[59] K. Abe *et al.*, (XMASS Collaboration), Nucl. Instr. Meth. A **716**, 78 (2013).

[60] S. Fukuda *et al.*, (Super-Kamiokande Collaboration), Nucl. Instrum. Meth. A**501**, 418 (2003).

[61] S. Agostinelli *et al.*, Nucl. Instr. Meth. A **506**, 250 (2003).

[62] K. Amako *et al.*, IEEE Trans. Nucl. Sci. **53**, 270 (2006).

[63] E. Aprile *et al.*, Phys. Rev. Lett. **107**, 131302 (2011).

[64] K. Abe *et al.*, (XMASS Collaboration), Phys. Lett. B **719**, 78 (2013).

[65] J. Beringer *et al.*, (Particle Data Group), Phys. Rev. D **86**, 010001 (2012).

[66] K. Freese *et al.*, Phys. Rev. D **37**, 3388 (1988).

[67] J. Ellis *et al.*, Phys. Lett. B **212**, 375 (1988).

[68] J. Engel, Phys. Lett. B **264**, 114 (1991).

[69] P. Toivanen *et al.*, Phys. Lett. B **666**, 1 (2008).

[70] P. Toivanen *et al.*, Phys. Rev. C **79**, 044302 (2009).

[71] P. Klos *et al.*, Phys. Rev. D **88**, 083516 (2013).

[72] M. Szydagis *et al.*, JINST 6 (2011) P10002; NEST (Noble Element Simulation Technique), http://nest.physics.ucdavis.edu/site/.

[73] L. Baudis *et al.*, Phys. Rev. D **88** 115014 (2013).

[74] J. D. Vergados, H. Ejiri, and K. G. Savvidy, Nucl. Phys. B **877**, 36 (2013).

[75] J. Angle *et al.*, Phys. Rev. Lett. **101**, 091301 (2008).

[76] Z. Ahmed *et al.*, Phys. Rev. Lett. **102**, 011301 (2009).

[77] D. Akimov *et al.*, Phys. Lett. B. **709**, 14 (2012).